PROCESS OPTIMIZATION OF METAL 3D PRINTING THROUGH THERMOGRAPHIC ANALYSIS OF THE MELT POOL

by

Matheus Andre SOARES

THESIS WITH ARTICLES PRESENTED TO ÉCOLE DE TECHNOLOGIE SUPÉRIEURE IN PARTIAL FULFILLMENT OF THE REQUIREMENTS FOR THE DEGREE OF MASTER OF APPLIED SCIENCE IN MECHANICAL ENGINEERING
M.A.Sc.

MONTREAL, AUGUST 21, 2026

ÉCOLE DE TECHNOLOGIE SUPÉRIEURE
UNIVERSITÉ DU QUÉBEC

BOARD OF EXAMINERS

THIS THESIS HAS BEEN EVALUATED

BY THE FOLLOWING BOARD OF EXAMINERS

Dr. Alena Kreitcberg, Thesis Supervisor
Department of mechanical engineering at École de technologie supérieure

Dr. Vladimir Brailovski, Thesis Co-supervisor
Department of mechanical engineering at École de technologie supérieure

Dr. Sébastien Lalonde, President of the Board of Examiners
Department of mechanical engineering at École de technologie supérieure

Dr. Pierre Bélanger, Member of the jury
Department of mechanical engineering at École de technologie supérieure

THIS THESIS WAS PRESENTED AND DEFENDED

IN THE PRESENCE OF A BOARD OF EXAMINERS AND PUBLIC

AUGUST 13, 2026

AT ÉCOLE DE TECHNOLOGIE SUPÉRIEURE

ACKNOWLEDGEMENTS

First and foremost, I would like to thank God for the life and health that have allowed me to reach this point.

To Dr. Brailovski and Dr. Kreitcberg, I express my deepest admiration and gratitude for all the help and support provided throughout my studies. I will always be grateful for the opportunity to pursue my Master's degree at this institution. The knowledge and guidance shared will be carried into my entire professional life, along with the conversations and advice about life itself.

I also thank my wife for standing by my side throughout this entire journey. For accepting the challenge of moving to a new country and reinventing herself professionally, and for enduring with so much love the days when I could not be fully present. I am equally grateful for all her efforts since we arrived here: for learning a new language and for contributing financially to our home.

To my family, I am grateful for all the support offered despite the distance and the novelty of moving abroad. You were present through every challenge, even if remotely. I am also deeply thankful for the effort of coming to visit us, even during the harsh weather conditions.

I would like to extend special thanks to two laboratory colleagues. First, to Donatien Campion, for guiding me since my very first day, sharing all of his knowledge about the equipment and supporting me throughout the entire sample production process required for my study, as well as helping with code development and manuscript revision. To Aurore Leclerc, my gratitude for her valuable contribution to the preparation of my article, for adding information in a clear and insightful manner, assisting with image production and data analysis, and also for her careful textual revision.

To the other members of the laboratory — Quentin, William, Josselin, Matthew, Chloé, Nolan, Mykhailo, Salah, Elisabeth, Emma, Pauline — and to everyone else who passed through LAMSI, thank you for making the workplace a pleasant and welcoming environment, even amid all the pressures inherent to a post-graduation program or internship.

Finally, I would like to thank my friend, professor, and undergraduate supervisor, Dr. Ziberov, and Dr. de Oliveira, who made my Master's degree possible by supporting me in writing articles and providing letters of recommendation. I also thank my friends in Brazil for their companionship and moments of laughter, even from afar. And to the friends I made here in Montreal, who have become my family: you will always be remembered with great affection, for the support and the prayers you dedicated to me and my wife.

Optimisation du procédé d'impression 3d métallique par analyse thermographique du bain de fusion

Matheus Andre SOARES

RÉSUMÉ

La fusion laser sur lit de poudre (LPBF) est l'une des technologies de fabrication additive métallique les plus utilisées dans l'industrie, mais la qualité des pièces fabriquées demeure fortement dépendante des paramètres du procédé et de leur effet sur le bain de fusion. Étant donné que la géométrie et la distribution de température du bain de fusion déterminent directement la formation de défauts, les contraintes résiduelles et la microstructure, leur caractérisation fiable in situ est essentielle tant pour le développement du procédé que pour l'assurance qualité.

Parmi les techniques de surveillance disponibles, les caméras thermiques offrent l'accès le plus direct à la surface du bain de fusion ; toutefois, les systèmes monochromatiques nécessitent une connaissance préalable de l'émissivité du matériau, une propriété qui ne peut être déterminée de manière fiable par un facteur unique dans les conditions transitoires et multiphasiques du procédé LPBF. Même les caméras bichromatiques, qui éliminent en principe la dépendance à l'émissivité par le rapport des luminances spectrales à deux longueurs d'onde, reposent en pratique sur des calibrations réalisées à l'aide de lampes à filament de tungstène dont les caractéristiques spectrales diffèrent significativement de celles d'un bain de fusion métallique formé par laser, produisant des lectures de température physiquement incohérentes lorsqu'elles sont appliquées aux conditions LPBF. Ces limitations ont jusqu'à présent confiné la plupart des systèmes d'imagerie thermique à une observation qualitative du procédé plutôt qu'à une caractérisation quantitative du bain de fusion.

Cette thèse développe et valide une méthodologie de surveillance quantitative in situ du bain de fusion à l'aide d'une caméra thermique infrarouge bichromatique calibrée par métallographie ex situ de cordons unitaires. L'approche bichromatique élimine le besoin de

caractérisation de l'émissivité en utilisant le rapport des luminances spectrales mesurées à deux longueurs d'onde (725 et 900 nm), tandis que la métallographie fournit des mesures indépendantes de largeur du bain de fusion servant à la fois de référence de calibration et de validation croisée. La calibration en cours de procédé, basée sur les températures de liquidus connues de cinq matériaux (316L, IN625, CoCr, W et Mo), a révélé des écarts de température allant jusqu'à 450 °C par rapport à la calibration par filament de tungstène, confirmant que la calibration commerciale ne permettait pas de convertir de manière fiable la luminance émise en température. La méthodologie complète, combinant imagerie thermique calibrée et validation métallographique, est dans un premier temps appliquée à trois alliages (316L, IN625 et CoCr) sur une large gamme de puissances laser et de vitesses de balayage sur un système d'impression EOS M280, puis validée sur le Ti-6Al-4V.

La caméra calibrée permet l'extraction de la largeur, de la longueur et de la température de surface du bain de fusion de manière indépendante de l'émissivité, avec une validation croisée entre les mesures de largeur par caméra et par métallographie présentant des écarts de seulement 6 à 9 % pour l'ensemble des matériaux. Combiné aux données de profondeur de bain de fusion métallographiques, ce dispositif fournit un jeu de données tridimensionnel complet du bain de fusion, utilisé pour évaluer la fiabilité d'un modèle analytique de conduction thermique. Le modèle s'est avéré fiable pour la prédiction des dimensions de surface dans le régime de fusion par conduction (R^2_{adj} globale > 0,70 pour la longueur, > 0,52 pour la largeur), mais sous-estime systématiquement la profondeur du bain de fusion dans le régime en trou de serrure en raison de la non-prise en compte de la pression de recul et de la dynamique de la vapeur, avec une déviation linéaire constante (pente ≈ 0,30) observée pour les trois matériaux.

Mots-clés : Fabrication additive, LPBF, Surveillance in situ, Caméra thermique, Pyrométrie bichromatique, Calibration en cours de procédé, Simulation analytique

Process optimization of metal 3d printing through thermographic analysis of the melt pool

Matheus Andre SOARES

ABSTRACT

Laser powder bed fusion (LPBF) is one of the most industrially used additive manufacturing technologies for metallic components, but the quality of printed parts is highly sensitive to the process parameters and their effect on the melt pool. Since the melt pool geometry and temperature distribution are related to the formation of process-induced defects, residual stresses, and microstructure, their reliable in-situ characterization is essential for both process development and quality assurance.

Among the available monitoring techniques, thermal cameras offer the most direct access to the melt pool surface, however, single-wavelength systems require prior knowledge of the material's emissivity, a property that cannot be reliably determined by a single factor under the transient, multi-phase conditions of the LPBF process. Even dual-wavelength cameras, which in principle eliminate emissivity dependence through the ratio of spectral radiances at two close wavelengths, rely in practice on calibrations performed using tungsten filament lamps. However, spectral characteristics of such lamps differ significantly from those of a laser-formed metallic melt pool, producing physically inconsistent temperature readings when applied to LPBF conditions. These limitations have so far confined most thermal imaging to qualitative process observation rather than quantitative melt pool characterization.

This thesis develops and validates a methodology for quantitative in-situ melt pool monitoring using a dual-wavelength infrared thermal camera calibrated through ex-situ single-track metallography. The dual-wavelength approach eliminates the need for emissivity characterization by utilizing the ratio of spectral radiances measured at two wavelengths (725 and 900 nm), while metallography provides independent melt pool width measurements that serve as both calibration and cross-validation reference. This calibration approach, based on the known liquidus temperatures of five materials (316L, IN625, CoCr, W, and Mo), revealed

temperature deviations of up to 450 °C compared to the tungsten filament calibration, confirming that the latter cannot reliably convert radiance emitted into temperature. The complete methodology, combining calibrated thermal imaging with metallographic validation, is initially applied to three alloys (316L, IN625, and CoCr) across a wide range of laser powers and scanning speeds on an EOS M280 system, and further validated on Ti-6Al-4V.

The calibrated camera enables emissivity-independent extraction of melt pool width, length, and surface temperature, with cross-validation between camera and metallographic width measurements showing discrepancies of only 6–9% across all materials. Combined with the metallographic melt pool depth data, this provides a complete three-dimensional melt pool dataset used to assess the reliability of an analytical thermal conduction model. The model proved to be reliable for predicting surface dimensions within the conduction melting regime (global $R^2_{adj} > 0.70$ for length, > 0.52 for width) but systematically underestimates melt pool depth in the keyhole regime due to the neglect of recoil pressure and vapor dynamics, with a consistent linear deviation (slope ≈ 0.30) observed across all three materials.

Keywords: Additive manufacturing, LPBF, In-situ monitoring, Thermal camera, Dual-wavelength pyrometry, In-process calibration, analytical simulation

TABLE OF CONTENTS

Page

LIST OF TABLES

LIST OF FIGURES

Page

LIST OF ABBREVIATIONS AND ACRONYMS

AE	Acoustic emission
AM	Additive manufacturing
ASTM	American Society for Testing and Materials
BJT	Binder jetting
CAD	Computer-aided design
CBD	Conditioned bulk densities
CMOS	Complementary metal-oxide-semiconductor
CoCr	Cobalt-chromium alloy
CT	Computed Tomography
DED	Directed energy deposition
EC	Eddy current
ÉTS	École de Technologie Supérieure
FEM	Finite element method
FOV	Field of view
FT4	Freeman Technology FT4 powder rheometer
HAZ	Heat-affected zone
IN625	Inconel 625 nickel-based superalloy
ISO	International Organization for Standardization
LED	Linear energy density
LOF	Lack-of-fusion
LPBF	Laser Powder Bed Fusion

MEX	Material extrusion
MJT	Material jetting
MPIF	Metal Powder Industries Federation
NIR	Near-infrared
NSERC	Natural Sciences and Engineering Research Council of Canada
OCT	Optical coherence tomography
OT	Optical Tomography
PBF	Powder bed fusion
RMSE	Root mean square error
ROI	Region of interest
SHL	Sheet lamination
SLA	Stereolithography
SLM	Selective laser melting
SLS	Selective laser sintering
SS316L	AISI 316L austenitic stainless steel
Ti-6Al-4V	Titanium-aluminum-vanadium alloy
VPP	Vat photopolymerization
μCT	Micro-computed tomography

LIST OF SYMBOLS AND UNITS OF MEASUREMENT

A	Absorptivity
a_1	Regression slope
a_2	Regression intercept (µm or µm²)
$B_\lambda(T)$	Spectral radiance of a blackbody ($W \cdot m^{-2} \cdot sr^{-1} \cdot m^{-1}$)
c	Speed of light in vacuum ($m \cdot s^{-1}$)
c_p	Specific heat capacity at constant pressure ($J \cdot kg^{-1} \cdot K^{-1}$)
d	Melt pool depth (µm)
dt	Time increment (s)
h	Planck constant (J·s)
h	Hatch distance (µm)
I	Pixel intensity from the thermal camera sensor (counts)
k	Thermal conductivity ($W \cdot m^{-1} \cdot K^{-1}$)
K_b	Boltzmann constant ($J \cdot K^{-1}$)
L	Melt pool length (µm)
L_λ	Spectral radiance measured at wavelength λ ($W \cdot m^{-2} \cdot sr^{-1} \cdot m^{-1}$)
LED	Linear energy density ($J \cdot mm^{-1}$)
P	Laser power (W)
Pe	Peclet number
R	Intensity ratio between two wavelengths
R^2_{adj}	Adjusted coefficient of determination
$RMSE$	Root mean square error (µm or µm²)

Rs	Electrical resistivity of the material (Ω·m)
r_f	Laser beam radius (m)
T	Temperature (K or °C)
T_0	Baseplate temperature (K)
T_{haz}	Heat-affected zone temperature (K or °C)
T_{melt}	Melting (liquidus) temperature (K or °C)
T_{vap}	Vaporization temperature (K or °C)
t	Layer thickness (µm)
v	Laser scanning speed ($mm \cdot s^{-1}$)
W	Melt pool width (µm)
x, y, z	Spatial coordinates (m)
α	Thermal diffusivity ($m^2 \cdot s^{-1}$)
ε	Spectral emissivity
ζ, η, ξ	Normalized spatial coordinates
λ	Wavelength of radiation (nm or m)
λ_1, λ_2	Camera wavelengths (725 nm and 900 nm respectively)
ρ	Material density ($kg \cdot m^{-3}$)
τ	Normalized time parameter

INTRODUCTION

Metal additive manufacturing (AM), also known as 3D printing, is a manufacturing process that consists of a layer-by-layer printing until the final part geometry is achieved. One of the most prominent technologies used in metal AM is the laser powder bed fusion (LPBF) capable of producing a near net shape part, even with complex geometries and performance requirements. Over the last decades, this technology has enabled the manufacturing of production-grade parts and has been widely used in aerospace, biomedical, energy and tooling applications. The advantages of the LPBF include fine microstructural properties, fabricating complex internal geometries and the possibility of producing parts with mechanical properties comparable or even superior to traditional manufacturing processes.

In LPBF, a laser beam scans across a thin layer of metallic powder following the geometry defined by a CAD model, melting and fusing the material before a new powder layer is deposited and the process repeats layer-by-layer until the final part is formed. In order to avoid oxidation and defects induced by the atmosphere, this process is realized in an inert atmosphere using typically argon for all materials, or nitrogen for non-reactive alloys such as steels and nickel- and cobalt-based alloys. The physical phenomenon is complex and includes different sets of important interactions including the laser-powder interactions responsible for the melt pool formation, the rapid solidification of the melted metal, the residual stresses and particular microstructures formed throughout the thermal cycles of the process.

The melt pool, defined by the zone of molten metal created by the laser, provides relevant data regarding defects and mechanical properties that can be expected at the end. It can be monitored through its geometry (width, length, and depth) and from the thermal fields generated by the temperature distribution inside the melt pool. These characteristics define the presence of defects, cooling rate and microstructure. It is then essential to monitor and predict the melt pool characteristics for process optimization and guarantee the quality of the final LPBF part.

The main defects observed in the LPBF process are the lack-of-fusion defects and keyhole pores. The first occurs when there is insufficient energy input, causing the powder to not fully melt, generating powder pockets and balling, which leads to porosity in the final part. The latter are caused by a high energy input generating a deep unstable cavity caused by the vaporization of the powder, which, when solidified, entraps gas and forms voids, thus reducing the final part density. These defects also end up reducing the mechanical properties of the printed parts, including reducing their tensile strength, fracture toughness and fatigue resistance.

However, due to the inherent process characteristics such as fast printing, rapid cooling, small melt pools and complex physical interactions, it becomes hard to monitor the process in real time and predict the final part characteristics.

For these reasons, a dual-wavelength camera was used in this work to monitor the printing of different alloys, including 316L stainless steel, IN625 superalloy, CoCr cobalt-chrome alloy, and the refractory metals tungsten and molybdenum, with an additional validation experiment on Ti-6Al-4V. This was done to capture thermal fields with different input parameters and also validate the use of a simplified analytical melt pool model to assess the influence of the parameters on the melt pool geometry and temperature.

CHAPTER 1

LITERATURE REVIEW

1.1 Laser Powder Bed Fusion (LPBF)

Additive manufacturing is the technology to manufacture complex parts adding material layer-by-layer and depositing metal, polymer or ceramic materials. This process is also known as 3D printing and can produce the part in a near net-shape geometry, allowing complex design parts that are not able to be produced by traditional manufacturing processes. According to the ISO/ASTM 52900 standard, there are 7 different techniques, namely: Vat Photopolymerization (VPP), Material Extrusion (MEX), Material Jetting (MJT), Binder Jetting (BJT), Powder Bed Fusion (PBF), Directed Energy Deposition (DED) and Sheet Lamination (SHL) (Kumar et al., 2021; Pessoa et al., 2021).

Laser Powder Bed Fusion (LPBF), a PBF process, is one of the most widely used metal additive manufacturing technologies. Due to its ability to produce near-net-shape parts with complex geometries, internal channels, and lattice structures, combined with reduced material waste and simplified post-processing, it has made it attractive across a variety of industries such as aerospace, automotive, biomedical, and energy sectors (Wang et al., 2023; Grasso & Colosimo, 2017). The process works by selectively melting thin layers of metallic powder using a laser beam, building the part layer by layer according to a CAD model until the final design is obtained (Wang et al., 2023). To avoid oxidation and possible contamination of the material, the process happens inside an inert atmosphere chamber. Argon is used for all materials, while nitrogen is usually used for non-reactive metals and alloys, mainly steels and nickel- and cobalt-based alloys. Some parameters that rule the process are defined by laser power (P), scanning speed (v), hatch distance (h) and layer thickness (t) as seen in Figure 1.1.

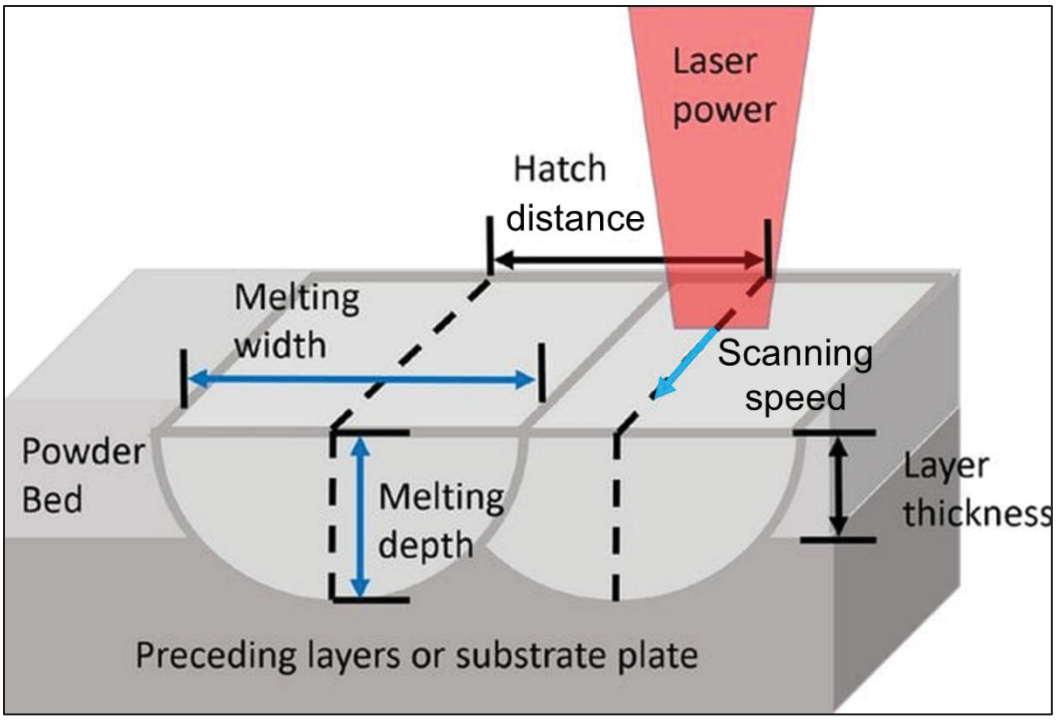

Figure 1.1: LPBF parameters diagram
Adapted from Aydogan and Chou (2024)

Despite being a versatile process, having consistent part quality (density and mechanical properties) is still a challenge in the LPBF. The physical interactions that govern the process are complex and occur at high temperatures, small spatial scales, fast laser scanning and rapid cooling rates (Yan et al., 2018; Mitrasinović et al., 2025). Deviations from the optimum laser power, scanning speed, hatch distance and layer thickness values can cause different defects (Shrestha & Chou, 2022; Khairallah et al., 2016).

When the laser power, scanning speed, hatch distance and layer thickness are optimized for the process window, the energy input to the powder bed is sufficient to fully melt the material without significant vaporization. This condition is known as the conduction regime (or mode), in which heat is transferred to the surrounding material primarily by thermal conduction, the melt pool maintains a stable semicircular shape, and the resulting tracks are less prone to balling and porosity (Patel and Vlasea, 2020). Outside this window, two main defects can be highlighted in LPBF, namely: Lack-of-fusion and Keyhole porosity (Gordon et al., 2020).

These effects correspond to the extreme conditions of low energy input, for Lack-of-fusion (LOF), and high energy input in the case of Keyhole porosity. The LOF porosity is defined by powder not melted between two scans, with insufficient overlap between scan paths leaving unfused powder particles entrapped in the final part. The keyhole pores are caused by the instabilities of a melt pool. These instabilities are created by intense recoil pressure and lead to the formation of gas-filled pores in the solidified material (Guo et al., 2023; Gordon et al., 2020).

The melt pool geometry (width (W), length (L) and depth (D)) and temperature distribution are the primary links between the process parameters and the quality of the resulting part (Figure 1.2: Melt pool dimensions
Adapted from Cheng and Chou (2016)). These three dimensions are the results of the energy balance in the process. Width and depth together define the cross-sectional area of each track, controlling the degree of fusion between tracks and layers and directly determining whether the process operates in the LOF, conduction, or keyhole regime. Length, which extends behind the laser in the scan direction, is related to the thermal tail of the melt pool and provides information about the cooling rate and solidification behavior (Wang et al., 2023; Kou, 2002).

An important constraint in the experimental characterization of melt pool geometry is that no single measurement technique can access all three dimensions simultaneously. Thermal cameras can capture the melt pool surface during printing, providing measurements of width and length, but cannot probe the depth since thermal emission is confined to the surface. Metallographic cross-sectioning of solidified single tracks, on the other hand, provides melt pool width and depth measurements but requires sample destruction and provides no information about length or the in-process thermal field.

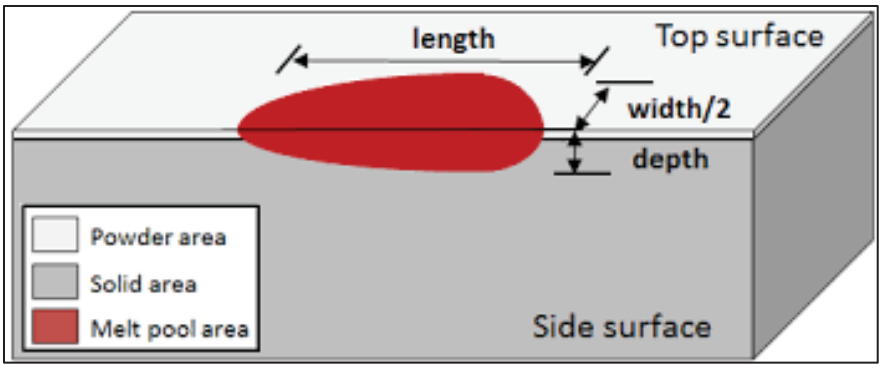

Figure 1.2: Melt pool dimensions
Adapted from Cheng and Chou (2016)

1.2 In-Situ Process Monitoring Techniques

Given the importance of controlling the melt pool and the transient, high-speed nature of the LPBF process, a variety of in-situ monitoring techniques have been developed to capture process information in real time without interrupting or interfering with the build (McCann et al., 2021; Myers et al., 2025). These can be categorized into optical, thermal, and acoustic methods, each offering different information and manifesting different limitations.

1.2.1 High-Speed Cameras

High-speed cameras operating in the visible spectrum can capture melt pool behavior, spatter ejection, and plume formation during LPBF at frame rates up to tens of kHz (McCann et al., 2021; Myers et al., 2025). They have been used to observe keyhole dynamics, melt pool oscillations, plume behavior (shown in Figure 1.3), and denudation zone formation. Myers et al. (2025) used high-speed optical imaging to study plume behavior and its interaction with the laser beam across a range of process conditions, demonstrating that plume attenuation can reduce effective energy delivery to the powder bed by up to 30% at high scanning speeds. However, the use of high-speed cameras for quantitative temperature measurements is limited because they capture light in a broad spectral range and require emissivity corrections that are difficult to apply reliably in the LPBF environment (McCann et al., 2021).

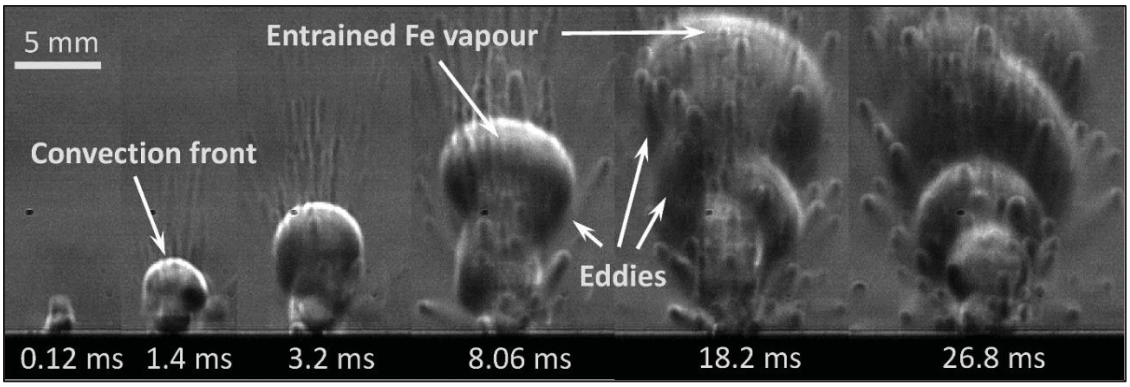

Figure 1.3: Plume formation during laser-powder interaction captured by high-speed camera Adapted from Bidare et al. (2018)

1.2.2 Photodiodes

Photodiodes are one of the simplest and most temporally responsive radiation-based sensing technologies for in-situ LPBF monitoring. Rather than converting detected radiation into an absolute temperature estimate, a photodiode measures the integrated light intensity emitted by the melt pool region over a defined spectral band, in the visible or near-infrared range, and outputs a voltage signal proportional to the total photon flux incident on the detector. When light from the melt pool strikes the photosensitive element, a photocurrent is generated and subsequently converted into a photovoltage by a load resistor; for a given wavelength, this photovoltage is directly proportional to the incident light power (Khairallah et al., 2016). The signal reflects the combined thermal emission from the melt pool, the vapor plume, and any surrounding hot material within the sensor field of view (FOV). The physical link to process state is indirect, meaning that a brighter signal corresponds to a higher-energy emission event, correlating with a higher local temperature, a larger melt pool area, or a more energetic ejection event, but the relationship is not quantitative in the way it is for a pyrometer or thermal camera.

The photodiodes can be placed in two different configurations: a) on-axis (Figure 1.4), where they are attached to the laser beam path via a beam splitter and observe only the small region around the melt pool, and b) off-axis, where the sensor is mounted in the build chamber and integrates emission from the full platform. By combining the scanner position data with the

photodiode signal, the time series is mapped onto the build plane, generating a layer-by-layer intensity map at resolutions up to 50 µm/pixel as seen in Figure 1.4. This resolution is sufficient to analyze individual hatch lines and localize anomalies to their point of origin within each layer (Fuchs & Eischer, 2018, Tao et al, 2024).

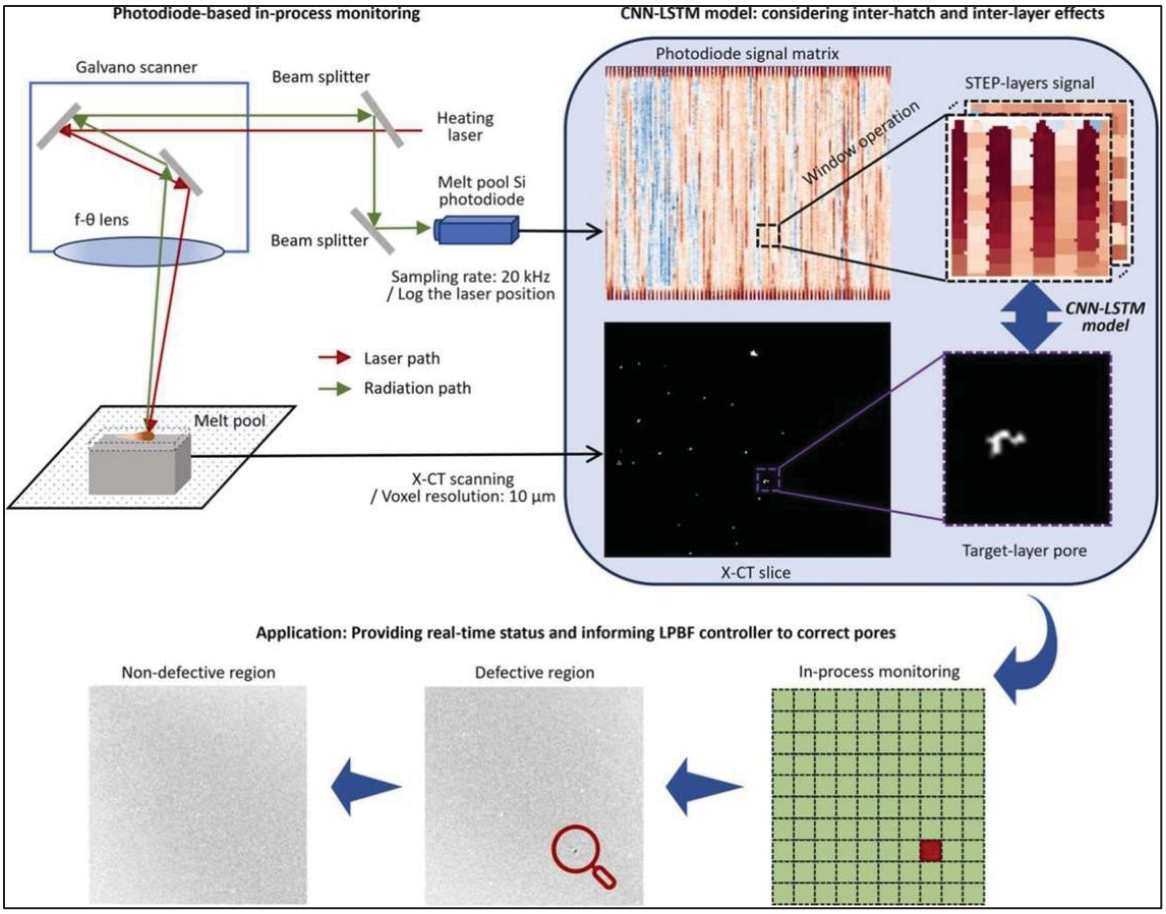

Figure 1.4: Diagram representing the steps to detect anomalies formation using photodiodes Taken from Tao et al. (2024)

The principal advantage of photodiodes over camera-based systems is temporal resolution. Commercial on-axis systems can operate at 60 kHz or higher, making photodiodes sensitive to sub-millisecond process events, such as keyhole instabilities, spatter ejection pulses, and laser power fluctuations that are temporally averaged out in any imaging-based approach (Fuchs & Eischer, 2018). Clijsters et al. (2014) implemented a high-speed melt pool monitoring system

combining an on-axis photodiode and camera in LPBF, demonstrating that the photodiode signal can detect material discontinuities and melt track inconsistencies in-process, establishing the foundation for photodiode-based closed-loop control. Coeck et al. (2019) demonstrated the porosity prediction capability of a two-photodiode setup during LPBF of Ti-6Al-4V, correlating signal anomalies with pore locations. The latter were confirmed by computed micro-tomography measurements (micro-CT) and achieved a prediction accuracy of 90% for pores with volume greater than 0.001 mm^3. However, the presence of 61 false positives among 93 predicted pores highlighted the ambiguity of integrated signals.

Taherkhani et al. (2021) developed a defect-detection system using photodiode signals collected from the melt pool, applying feature extraction and machine learning classification to discriminate between nominal and anomalous process states across multiple alloys and parameter combinations, showing that data interpretation improves the defect classification performance of raw photodiode signals. More recently, Zhang et al. (2023) used an off-axis photodiode system to monitor single-track melting states in LPBF, classifying tracks into the three melting regime categories (conduction, keyhole, and LOF) using a neural network trained on the photodiode time series, achieving reliable regime identification across nine parameter combinations, demonstrating that even a simple off-axis configuration carries sufficient process information for regime classification when aligned with appropriate signal processing.

The main limitation of photodiodes is spatial ambiguity, because the signal integrates all the emissions within the sensor FOV simultaneously. Moreover, they add contributions from the melt pool, spatter, plume, and background thermal emission, making defect classification and dimensional measurement unreliable, when photodiodes are used in isolation. This limitation is most effectively addressed by combining photodiodes with a camera-based system, where the diodes provide high-temporal-resolution anomaly detection and precise scan-path localization, while the camera supplies the geometric and spatial context needed to distinguish between defect types: an architecture that represents the current industrial standard for photodiode-based LPBF monitoring (Fuchs & Eischer, 2018; McCann et al., 2021).

1.2.3 Pyrometers And Thermal Cameras

All non-contact thermal measurement methods based on the detection of thermal radiation rely on the Planck's law of blackbody emission (Vollmer, M., & Möllmann, K. 2017), which describes the spectral radiance emitted by a perfect blackbody at temperature T, at a specific wavelength λ as:

$$B_\lambda(T) = \frac{2hc^2}{\lambda^5} \cdot \frac{1}{e^{\frac{hc}{\lambda k_B T}} - 1} \tag{1.1}$$

where h is the Planck's constant (J·s); T, the temperature (K); c, the speed of light (m/s); and K_b, the Boltzmann's constant (J/K); and $B_\lambda(T)$, the blackbody spectral radiance ($W \cdot m^{-2} \cdot sr^{-1} \cdot m^{-1}$).

In the short-wavelength limit, where $hc/\lambda k_B T >> 1$, the exponential term dominates and Planck's law simplifies to Wien's approximation (Vollmer & Möllmann, 2017):

$$B_\lambda(T) = \frac{2hc^2}{\lambda^5} \cdot e^{-\frac{hc}{\lambda k_B T}} \tag{1.2}$$

and forms the basis for temperature estimation from intensity measurements in the near-infrared range commonly used by LPBF monitoring cameras.

For real materials, also called gray bodies, the emitted spectral radiance is reduced relative to that of a perfect blackbody by a wavelength-dependent emissivity factor ε, which depends on the material, its temperature, its surface roughness, and the observation wavelength. Incorporating ε into Wien's approximation gives:

$$B_\lambda(T) = \varepsilon \cdot \frac{2hc^2}{\lambda^5} \cdot e^{-\frac{hc}{\lambda k_B T}} \tag{1.3}$$

Single-wavelength pyrometers estimate the temperature from the radiance measured at a single spectral band. The major limitation is that this conversion requires knowledge of the emissivity, which in the LPBF environment varies continuously within and around the melt pool, making accurate single-wavelength temperature measurements without a priori emissivity characterization very challenging (Mitchell et al., 2019; Williams et al., 2019). Dual-wavelength (ratio) pyrometers partially mitigate this issue by measuring the radiance at two nearby wavelengths λ_1 and λ_2 and computing their ratio. Under Wien's approximation and the assumption that emissivity is equal at the two closely spaced wavelengths, the emissivity in the ratio cancels, allowing temperature to be estimated without prior knowledge of the material's emissivity (Araujo, 2021):

$$\frac{L_{\lambda 1}(T)}{L_{\lambda 2}(T)} = \frac{\varepsilon B_{\lambda_1}(T)}{\varepsilon B_{\lambda_2}(T)} \tag{1.4}$$

where $L_\lambda$corresponds to the radiance measured by the sensor at a wavelength λ.

Thermal cameras extend the pyrometric concept to provide a 2D thermal map over a region. Dual-wavelength thermal cameras apply ratio pyrometry region-wise or pixel-by-pixel across the full FOV, producing temperature maps of the melt pool at frame rates up to several tens of kHz (Figure 1.5). While the pixel-by-pixel ratio is the most physically accurate method to obtain temperature, it also produces a noisy image if the pixel resolution is not sufficiently small or if the pixel position is not correctly aligned between sensors (Vollmer and Mollmann, 2017). On the other hand, using a region-wise ratio calculates an emissivity factor only in a small portion of the image and is considered constant for the rest of the pixels (Mitchell et al., 2019), producing a clearer image but that might not represent reality if the emissivity varies significantly across the image.

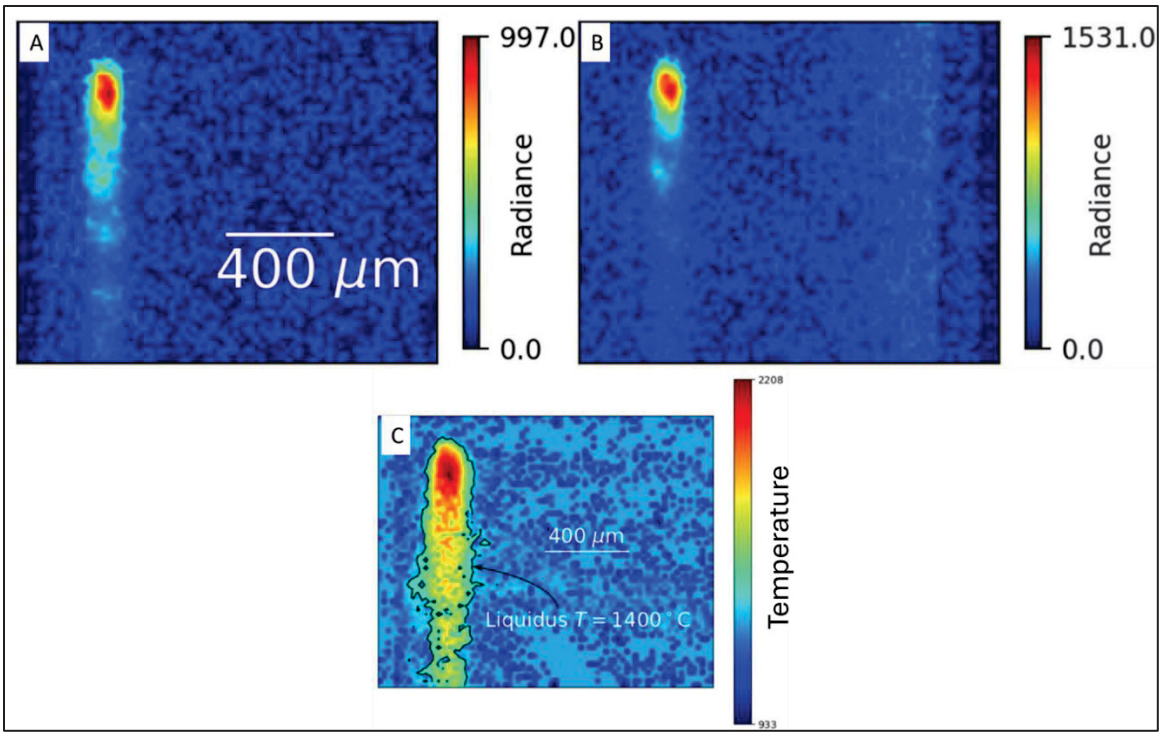

Figure 1.5: Example of radiance image captured at (a) 900 nm and (b) 725 nm, and (c) temperature image based on region-wise conversion

Adapted from Mitchell et al.(2019)

Several key studies have demonstrated the capabilities and limitations of dual-wavelength thermal cameras for LPBF monitoring. Hooper (2018) detailed thermal imaging of the LPBF melt pool using a two-wavelength system, measuring peak temperatures near the vaporization point (~3000 °C for 316L) and cooling rates on the order of 10^6 K/s, confirming the extreme thermal conditions within the melt pool. Wang et al. (2022) used multi-sensor approaches including a thermal camera to correlate in-situ melt pool measurements with process parameters for multiple alloys. This study demonstrated the potential of thermal data for quality monitoring together with an emissivity calibration method considering the contour of the melt pool at the melting point of the material. Myers et al. (2023) extended two-color thermal imaging to a standard color camera platform, demonstrating that high-resolution melt pool temperature mapping can be achieved with consumer-grade hardware by appropriate spectral filtering.

Furthermore, Mitchell et al. (2019) correlated pyrometric thermal signals with porosity in additively manufactured metals, showing that melt pool temperature data can serve as a proxy for the assessment of defect formation risk. It also presented a detailed path for thermal image treatment, including the melt pool isolation from spatter and studying the correlation between spatters and defects. Finally, Williams et al. (2019) showed that in-situ layer temperature measurements correlate with final part porosity, microstructure, and mechanical properties, demonstrating the potential of thermal monitoring for in-process quality control. One of the limitations of thermal camera approaches for LPBF is that they cannot measure melt pool depth, since thermal emission is captured from the surface of the melt pool only (McCann et al., 2021). Another limitation of these instruments is that they are not able to correctly measure background temperature, due to a significant discrepancy of temperatures inside the melt pool and its contour.

1.2.4 Other Advanced In-Situ Monitoring Techniques

Beyond optical and thermal cameras, more specialized in-situ monitoring techniques have been developed for LPBF research. High-speed synchrotron X-ray imaging provides information on melt pool depth inaccessible for surface optical methods, enabling direct observation of keyhole dynamics, melt pool flow, pore formation, and solidification in real time (Zhao et al., 2020; Huang et al., 2022). Zhao et al. (2020) used this technique to identify keyhole tip instability as the primary mechanism of pore formation, seen in Figure 1.6, while Huang et al. (2022) identified keyhole fluctuation as the cause of porosity. However, these experiments are limited to large synchrotron facilities and cannot be performed on production machines.

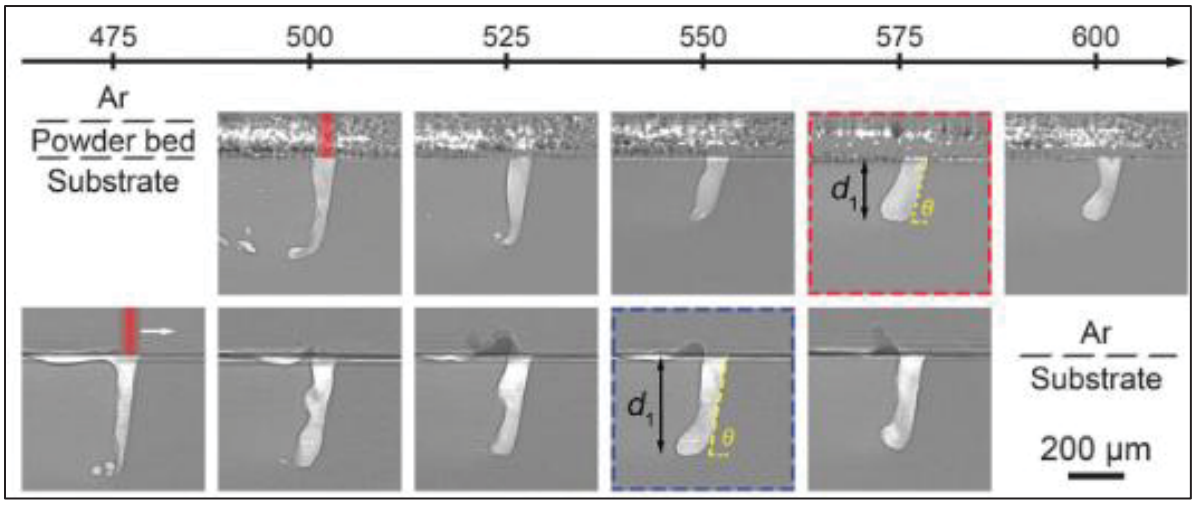

Figure 1.6: Melt pool depth captured by high-speed x-ray imaging with a range of scanning speed

Taken from Zhao et al. (2020)

Acoustic emission (AE) monitoring represents a more accessible alternative, capturing ultrasonic waves generated during laser–powder bed interaction. Pandiyan et al. (2024) demonstrated a machine learning approach combining acoustic emission signals with process maps for the LPBF process classification, showing that acoustic signals can distinguish between different melting regimes (LOF, conduction mode and keyhole) at a cost and complexity level compatible with industrial integration. However, interpretation and obtaining acoustic signal without noise is challenging since the readings include the superposition of laser–powder interaction, machine vibration, powder recoating noise, and environmental background.

Eddy current (EC) monitoring is an electromagnetic non-destructive technique adapted for in-situ LPBF monitoring, in which an alternating magnetic field induces circulating currents in the conductive part whose path and intensity depend on the local electrical conductivity, which is a property sensitive to porosity, cracks, and temperature. Spurek et al. (2022) integrated an EC sensor on the recoater of a LPBF machine and demonstrated that differences in relative density as small as 0.1% could be detected in AlSi10Mg by correlating the EC signal with micro-CT measurements. The EC sensors can simultaneously measure effective solidified

layer thickness and a total part height. Peng et al. (2025) extended the approach to subsurface temperature monitoring by exploiting the temperature dependence of electrical conductivity in austenitic steels, validating through coupled thermal–electromagnetic simulations that the EC signal can track temperature variations in the 420–700 K range, information inaccessible to surface optical method. However, the technique is limited by the electromagnetic skin effect, which constrains the penetration depth to a few hundred micrometers at typical operating frequencies, and by the need for calibration to convert impedance variations into quantitative estimates.

Beyond thermal imaging, laser-based ultrasound (LBU) is a complementary non-contact, all-optical technique for characterizing LPBF parts, offering surface and sub-surface defect detection without the acquisition times and part-size trade-offs of X-ray CT. Harke et al. (2022) demonstrated a surface acoustic wave (SAW) setup on Ti-6Al-4V single-tracks, successfully resolving spatter deposits, track discontinuity, and sub-surface voids within approximately 200 μm of the surface; the detection depth was limited by the frequency-dependent power flux density of the Rayleigh wave, with voids deeper than 400 μm falling below the experimental noise floor. Xu et al. (2024) extended the approach across four LPBF alloys (Ti-6Al-4V, AlSi10Mg, 316L, and IN718) by coupling a finite element simulation with a through-transmission experimental platform, reporting that the longitudinal wave amplitude decreases nearly linearly with the internal defect diameter and that artificial holes as small as 200 μm could be characterized in all four materials, with the signal amplitude scaling with each alloy's thermal expansion and thermal conductivity coefficients. Together, these studies establish LBU as a promising diagnostic for LPBF that complements the surface view provided by dual-wavelength thermal imaging, although its practical depth sensitivity remains constrained to near the surface region and its interpretation depends strongly on the alloy's thermophysical properties.

Each monitoring technique reviewed accesses different aspects of the LPBF process and carries different limitations. High-speed cameras and optical tomography observe the powder bed surface and melt pool geometry but cannot provide subsurface information or absolute

temperature. Pyrometers and photodiodes offer high temporal resolution but lack spatial resolution. Dual-wavelength cameras provide 2D temperature maps but are limited by calibration accuracy and cannot measure melt pool penetration depth. Synchrotron X-ray imaging provides unmatched subsurface detail but is inaccessible outside specialized facilities. Acoustic emission is sensitive to bulk defect events but requires machine learning to interpret the signal. Eddy current monitoring can complement these approaches providing subsurface electrical and thermal information but is limited by penetration depth and material-specific calibration. The trend in the field is to combine multiple sensors to access complementary process information (McCann et al., 2021; Aydogan & Chou, 2024).

Table 1.1: Comparison of in-situ monitoring techniques for LPBF

Technique	Surface observation	Depth observation	Temperature acquisition
High-speed camera	✓	×	×
Photodiodes	✓	×	×
Pyrometer/Thermal camera	✓	×	✓
Synchrotron X-Ray	✓	✓	×
Acoustic emission	×	✓	×
Eddy current		✓	×*
Laser ultrasound	✓	✓	×

* Only possible in materials with high thermal conductivity dependence.

1.3 Ex-Situ Characterization: Single-Track Metallography

Complementary to in-situ thermal monitoring, post-process metallographic analysis of solidified single laser tracks provides the most direct and relatively accurate measurements of melt pool cross-sectional geometry. To this end, in a single-track experiment, an individual laser scan is performed on top of the last printed layer under controlled process parameters, without depositing a powder layer above. The resulting track is then sectioned perpendicular

to the scan direction, mounted, polished and etched to reveal the melt pool cross-section. From this cross-section, the width and depth of the fused zone can be measured directly using a microscope, with measurement uncertainties typically in the range of ± 5-20 µm depending on the etch contrast and image resolution (Shrestha & Chou, 2018; Goossens & Van Hooreweder, 2021).

The single-track approach offers several key advantages for process characterization: it provides a clear and direct measurement of the melt pool geometry; it can distinguish between conduction mode, keyhole, and lack-of-fusion based on cross-sectional morphology of the tracks and it can be performed across a wide range of laser powers and scanning speeds in a single experiment, enabling a fast process window mapping, as shown in Figure 1.7 taken from Ren et al. (2024). Additionally, the top view of a single track provides the width of the fused region at the surface, which can be directly compared with thermal camera measurements taken from the same perspective during printing (Shrestha & Chou, 2018).

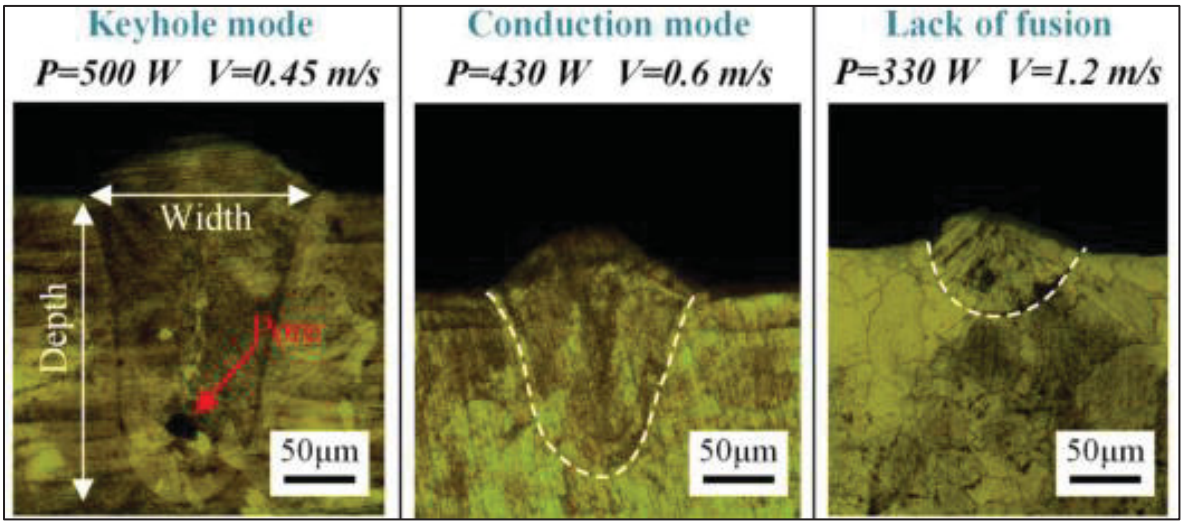

Figure 1.7: Cross section image of CuCrZr representing the 3 different modes in LPBF: Keyhole, conduction mode and lack of fusion

Taken from Ren et al. (2024)

The primary limitations of single-track metallography are its destructive and time-consuming nature, and the fact that it provides no information about the in-process melt pool length or

thermal behavior. Furthermore, single tracks in the lack-of-fusion regime may not produce a detectable cross-section if the balling effect causes the material to not adhere uniformly to the substrate. The complementarity between thermal camera observations (temperature, width and length, in-situ) and metallographic measurements (width and depth, ex-situ) is therefore clear: combining both techniques in the same experimental procedure provides access to all three melt pool dimensions simultaneously, while the shared width measurement creates a cross-validation opportunity that confirms the reliability of both approaches (Goossens & Van Hooreweder, 2021; Park et al., 2025).

1.4 Thermal Camera Calibration

The reliability of temperature measurements from a dual-wavelength thermal camera depends significantly on the quality of its calibration, meaning the mathematical relationship between the measured intensity ratio and the absolute temperature of the observed surface. Without accurate calibration, the temperature maps produced by the camera may be physically unrealistic, and the melt pool contour cannot be extracted reliably since the melting temperature isotherm might not be identified in the image. Calibration is therefore not merely a technical detail but a fundamental prerequisite for the quantitative use of thermal camera data in LPBF monitoring.

1.4.1 Tungsten Filament Calibration and its Limitations

The calibration approach most used in commercial dual-wavelength systems employs a tungsten filament lamp as a reference source. A tungsten filament is heated to a series of known temperatures through controlled electrical current, and the camera's pixel intensity response at each wavelength is defined as a function of the known temperature. This calibration approach is practical and easily reproducible. However, it carries a fundamental limitation when applied to LPBF: the conditions during calibration differ substantially from those during actual melt pool imaging (De Izarra & Gitton, 2010; Partouche-Sebban et al., 2005).

The spectral emissivity of tungsten differs from the effective emissivity of the metallic melt pool in LPBF, which is a mixture of liquid metal, vapor, and condensate with a complex and variable spectral response. Tungsten filament lamps are enclosed in a glass bulb, while the in-process measurement path passes through the sensor optics, and potentially through spatter and condensate generated during the printing that can possibly contaminate the optical path. Furthermore, the spatial distribution of emitted light from a heated filament is non-uniform (Figure 1.8), introducing errors that depend on which region of the filament is chosen as reference (De Izarra & Gitton, 2010). De Izarra and Gitton (2010) characterized this spatial non-uniformity of a standard tungsten lamp used in pyrometer calibration, finding temperature gradients of up to 200 °C along the filament length.

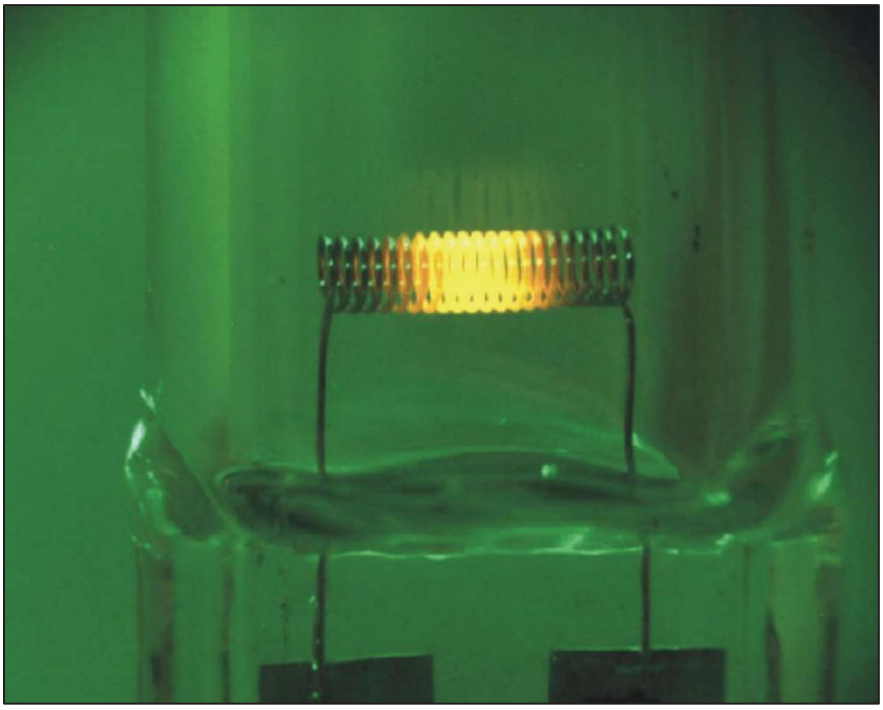

Figure 1.8: Radiance emitted from a tungsten filament with low current
Taken from Fu et al. (2006)

The practical consequence of these discrepancies in the context of LPBF is that the cameras systematically overestimate melt pool temperatures by several hundred degrees Celsius. This makes it impossible to use the melting temperature of the material as a contour threshold for

melt pool boundary extraction, which in turn prevents any quantitative dimensional measurement from the thermal image with the conventional calibration (Hooper, 2018).

1.4.2 In-Process Calibration Using Melting Points

To address the limitations of tungsten filament calibration, an alternative approach uses the melting point of the material being processed as a physical temperature reference that is tied to real in-situ measurement conditions. This approach is based on the following principle: for a given material and set of process parameters, an in-situ thermal image of the melt pool contains a contour at some intensity level that corresponds to the liquidus temperature of the material, i.e., to the boundary between the melt pool and the surrounding material (solid or powdered). By identifying this contour in the thermal image and correlating it with the known liquidus temperature, the intensity ratio–temperature pair can be established without any assumptions about emissivity or optical conditions. Repeating this process across multiple materials with different melting temperatures could allow building a calibration curve correlating intensity with temperature in a wide temperature range, entirely under real LPBF operating conditions.

The key experimental challenge of this method is determining which intensity contour corresponds to the melt pool boundary, since the camera cannot directly indicate the location of the solidus isotherm. The approach that solves this issue makes a cross-referencing the thermal image with ex-situ metallographic measurements of the single-track width: the intensity threshold at which the measured image width equals the metallographically measured track width is taken as the liquidus contour, and the corresponding intensity ratio provides the calibration point at the liquidus temperature of the material.

This concept was studied by Doubenskaia et al. (2015) for single-wavelength sensors during LPBF of a C103 niobium-based refractory alloy (Nb-10Hf-1Ti), where the melting point isotherm was used to measure the effective emissivity of the melt pool surface. Park et al. (2025) extended this approach to the same alloy processed by LPBF, correlating single-

wavelength thermal camera contours with metallographically measured single-track widths to calibrate the sensor and validate numerical simulations of the solidification velocity and thermal gradient (Figure 1.9).

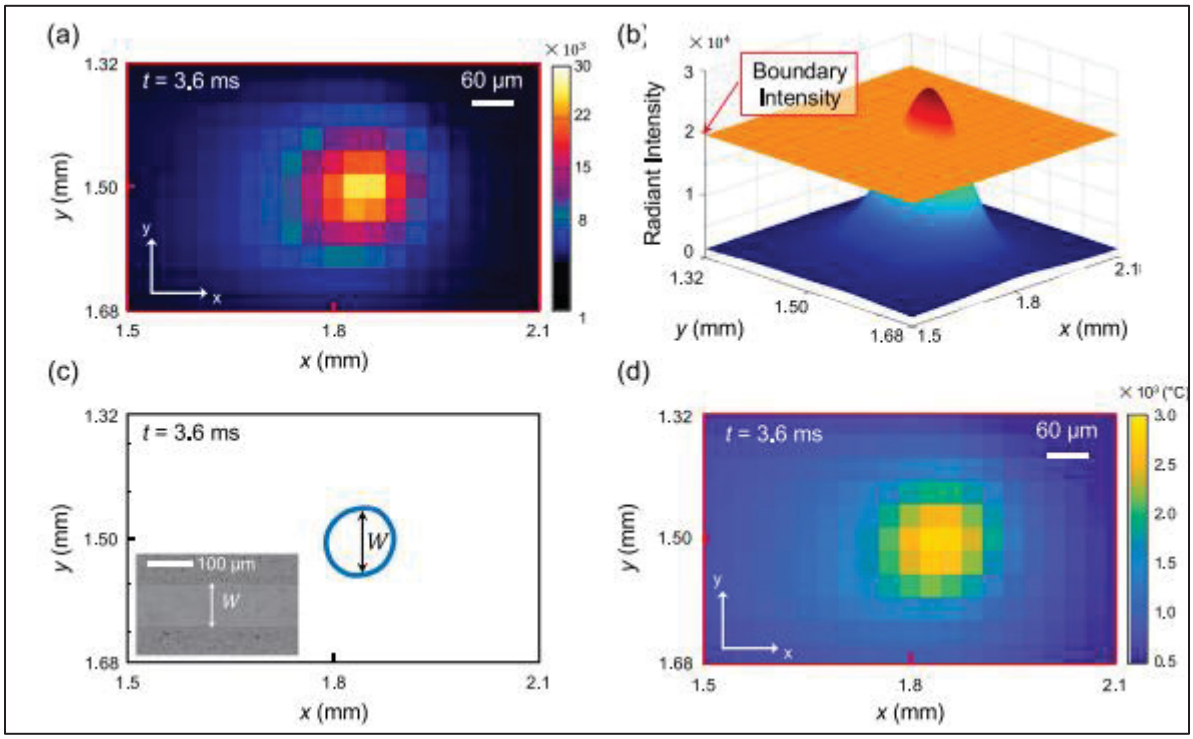

Figure 1.9: A) example of radiance image during LPBF, b) intensity threshold applied based on the width measured in (c), and (d) final temperature result

Taken from Park et al. (2025)

Some practical limitations of this calibration process should be acknowledged. The metallographic measurements required as input have inherent measurement uncertainties (typically ±5–20 μm) that propagate into the calibration. The camera must be operated under conditions that avoid pixel saturation at both wavelengths for all materials, requiring careful selection of exposure time and neutral density filters for each material and parameter combination, significantly increasing the experimental time required. Furthermore, the calibration is specific to the camera configuration and optical path on a given machine and needs to be repeated if the optical setup changes. Additionally, the resolution of the camera will define how precise the calibration is.

1.5 Melt Pool Simulations

Computational modeling of the LPBF melt pool provides a physical predictive link between process parameters with melt pool geometry and thermal field, complementing the experimental characterization techniques described previously. Models are available in a wide range of complexities, from fast analytical solutions to high-fidelity simulations, and the choice of model depends on the computational resources available and the level of physical fidelity required.

1.5.1 Analytical Models Based on Moving Heat Sources

The analytical melt pool model used in this study is based on the solution of the steady-state heat conduction equation for a moving heat source in a semi-infinite solid, a problem that was solved in the context of welding by Rosenthal in 1946 (Hugel & Dausinger, 1998). In the LPBF context, the laser beam is modeled as a moving Gaussian heat source and is thoroughly discussed in Chapter 3.

The primary advantage of analytical models is their computational speed: a complete melt pool temperature field can be computed in seconds on a standard computer, enabling rapid analysis across a wide range of process parameters and materials. This makes them ideally suited for process window mapping and material-specific optimization before costly experimental simulations are performed. Letenneur et al. (2019) demonstrated this approach for density optimization of multiple LPBF alloys using the analytical model in combination with design-of-experiment methods, while Leclercq et al. (2024) applied it to the tungsten LPBF parameter optimization.

Because the material in LPBF is a metal powder bed rather than a dense solid, the thermophysical properties must be corrected to account for the porous nature of the bed. The powder bed absorptivity is estimated from the bulk material absorptivity using the Hagen-Rubens relation and corrected for the effective emissivity of a porous powder surface. The

effective thermal conductivity of the powder bed is reduced relative to the dense solid value according to the porosity percentage (Sih & Barlow, 2004. Hugel & Dausinger, 1998).

1.6 Summary and Research Objectives

The literature review in the preceding sections establishes the foundation for the present work. LPBF is a process governed by a complex set of interacting phenomena at the melt pool scale, where laser power, scanning speed, and material thermophysical properties altogether determine the melt pool geometry, the thermal field, and, ultimately, the presence or absence of defects. Controlling and predicting these outcomes requires tools that operate at complementary levels: simulation models that can rapidly map the process window before costly experiments are conducted, and in-situ monitoring systems that can observe the melt pool during printing and provide experimental data for model validation.

On the simulation side, fast analytical melt pool models based on the moving heat source solution are used to guide process parameter selection for a wide range of metallic alloys. These models offer advantages in computational speed and multi-material flexibility, but their reliability has only been assessed using a single experimental technique at a time. The combination of in-situ dual wavelength thermal camera observations and ex-situ metallographic measurements in the same experimental campaign, accessing all melt pool dimensions and temperatures with a cross-validation on the melt pool width measurements, has not been reported.

On the monitoring side, dual-wavelength thermal cameras are capable tools for spatially resolved, quantitative in-situ melt pool temperature measurements in LPBF. However, their precise use is limited by a calibration problem: commercial tungsten filament calibrations are performed in an environment that does not represent LPBF building process and produce systematic temperature overestimations of several hundred degrees Celsius, making it impossible to identify the melt pool boundary from the thermal image. The concept of using the material's liquidus temperature as an in-process calibration reference, anchored by

metallographic single-track width measurements, has been demonstrated for single-wavelength sensors but has not been extended to dual-wavelength cameras or applied across a range of materials with widely different melting points.

These two limitations are connected, where a reliable thermal camera calibration is a prerequisite for using its result as a validation for the analytical model, and the model provides the simulation context needed to interpret the camera results. The present work addresses both limitations through a methodology that integrates analytical simulations, dual-wavelength thermal camera monitoring, and single-track metallography as three mutually supporting tools.

This work is based on a dual hypothesis that the liquidus temperature of the material provides a physically consistent and practical calibration reference for a dual-wavelength thermal camera, and that the analytical conduction model accurately captures the process-dependent trends of melt pool width, length, and area in the conduction melting regime. To validate these hypotheses, the following specific objectives are defined:

– Develop and validate a novel in-process calibration method for a dual-wavelength thermal camera (Stratonics Thermaviz) using the liquidus temperatures of five materials (316L, IN625, CoCr, W, Mo) as physical calibration references, according to ex-situ metallographic measurements of their respective single-track widths. The method must produce temperature maps that are physically consistent across a melting temperature range of approximately 1300-3422 °C and must reduce the peak temperature overestimations associated with the conventional tungsten filament calibration to more realistic values.

– Assess the reliability of the simplified Gaussian heat source analytical model by comparing its predictions of melt pool width, length, depth, surface area and temperature against simultaneous in-situ thermal camera observations and ex-situ metallographic measurements for three alloys (316L, IN625, CoCr). This assessment must be done across a wide range of process parameters covering the LOF, conduction, and keyhole melting regimes. The analysis must identify which dimensions and regimes the model predicts reliably, quantify systematic

discrepancies where it does not, and cross-validate the two experimental techniques through their shared melt pool width measurements.

The work carried out in this thesis is organized into two parts, each presented as an article. The first article (Chapter 2) addresses the calibration objective, proposing and validating the in-process calibration approach across five materials with the thermal camera and metallography combined. The second article (Chapter 3) uses this validated methodology to assess the analytical model reliability across the full range of melting regimes for three materials, namely 316L, IN625, and CoCr metallic alloys. To validate the calibration method, Ti-6Al-4V is used, a material not utilized in the proposed calibration process, and the method and results are described in Chapter 4. The general conclusion synthesizes the findings of both articles considering the objectives stated above and identifies limitations and possibilities for future work.

CHAPTER 2

IN-SITU LPBF MONITORING USING A DUAL-WAVELENGTH THERMAL CAMERA CALIBRATED VIA EX-SITU SINGLE-TRACK MEASUREMENTS

Matheus Soares [a], Donatien Campion [a], Alena Kreitcberg [a], Vladimir Brailovski [a]

[a] Département de Génie mécanique, École de Technologie Supérieure,
1100 Notre-Dame Ouest, Montréal, Québec, Canada H3C 1K3

Article presented at WorldPM2026, Montreal, QC, Canada, June 25–29, 2026

2.1 Preface

To obtain reliable quantitative measurements from the dual-wavelength thermal camera and use them to validate the analytical melt pool simulation, it is necessary to establish a physically consistent relationship between the thermal radiation observed by the sensor and the actual temperature of the melt pool surface. The commercial tungsten filament calibration was found to produce temperature readings inconsistent with the physical properties of the materials being processed, preventing the use of the camera as reliable equipment. This first article therefore addresses the calibration problem as a prerequisite, developing an in-process calibration method using the melting point of the processed material as a physical temperature reference, with the melt pool boundary identified through ex-situ metallographic width measurements of single tracks. The method yielded a calibration curve that brings peak temperature estimates close to the vaporization point of each material and enables the use of the liquidus temperature as a threshold for direct melt pool surface measurement from the thermal image, capability required for the validation study presented in Chapter 3.

2.2 Abstract

Real-time monitoring of the laser powder bed fusion (LPBF) process using in-situ dual-wavelength infrared thermal camera observations can contribute to the improvement of process reproducibility and quality control. Dual-wavelength thermography estimates the melt pool

temperature distribution without prior knowledge of the material emissivity by applying Wien's approximation of Planck's law to the pixel-wise intensity ratio obtained at two close wavelengths. However, when applied to LPBF thermal fields, conventional tungsten filament-based calibration methods used to convert the intensity ratio to temperature values often lead to unrealistic temperature distributions.

In this work, a novel thermal camera calibration approach using post-process single-track measurements is proposed. The method correlates melt-pool contour intensities obtained during powder bed fusion of multiple materials (316L, CoCr, IN625, W, Mo) with their melting temperatures, thus covering a wide range of melting points and process conditions. The proposed calibration method leads to an approximately 20% improvement in the melt pool dimensional accuracy as compared to the tungsten filament-based calibration, thus providing a practical and physically consistent calibration strategy for the dual-wavelength thermal monitoring of LPBF processes.

2.3 Introduction

In-situ monitoring of the laser powder bed fusion (LPBF) process remains a significant challenge due to its intrinsic particularities, including high scanning speeds and process temperatures, rapid cooling rates, complex laser-powder interaction phenomena, and micrometer-scale melt pool dimensions (Aydogan & Chou, 2024; Grasso & Colosimo, 2017; Yan et al., 2018). Nevertheless, real-time monitoring can provide valuable information regarding the process stability, defect formation, and final part quality (Pandiyan et al., 2024). Temperature measurements, in particular, can be used to validate process simulations, predict defect formation, and optimize building strategies (Mahmoudi et al., 2018, Mitchell et al., 2020, Williams et al., 2019).

Several non-contact temperature measurement techniques are available for LPBF applications. Pyrometers can measure the temperature at a given point or along a line and can be classified according to the number of wavelengths used as single-wavelength, dual-wavelength (ratio

pyrometry), and multi-wavelength systems. While the single-wavelength pyrometry is highly dependent on emissivity values, which vary with temperature, phase state and surface conditions, dual-wavelength (ratio) pyrometry mitigates this issue by calculating the ratio of light intensities from two distinct sensors. Thermal cameras extend this concept by providing spatially resolved temperature measurements over a region, while relying on the same radiative emission principles (Yan et al., 2018). More advanced techniques, such as X-ray imaging, are less common in industrial applications, and are generally confined to research laboratory setups (Scheel et al., 2023).

A key challenge in non-contact thermography is the calibration routine required to convert measured light intensities into temperatures. Since the blackbody simulator-based calibration approach provides high accuracy, but is extremely expensive and time-consuming (McCann et al., 2021), commercial systems frequently use tungsten filaments to generate calibration curves. Although this approach is practical, it may introduce errors due to an uneven filament heating, optical distortions, and which is even more challenging, differences between laboratory and in-process measurement conditions. These inaccuracies often result in unrealistic temperature readings (De Izarra & Gitton, 2010; Partouche-Sebban et al., 2005; Russell et al., 1960). Another common approach assumes constant emissivity values across the entire image, which reduces noise but introduces systematic errors because the emissivity of metal powder, molten and heated metals differ significantly (Mitchell et al., 2020).

To address the above limitations, this study proposes a novel calibration method for dual-wavelength thermal cameras that involves the use of post-process single-track width measurements obtained for multiple materials with melting points ranging from ~1300 to 3420 °C and submitted to variable LPBF process conditions. Allowing the calibration being performed even under non-ideal laboratory conditions (e.g., with a tungsten filament or a flat solid sample), but directly during a real LPBF process using the powder bed. This represents the actual process conditions, including the emissivity of the powder and melt pool. Combining in-situ intensity measurements with ex-situ metallographic observations allows establishing a

physically consistent calibration curve, more suitable for thermal monitoring of the LPBF process than can be done using its conventional tungsten filament-based calibration approach.

2.4 Experimental Setup

Single-track building experiments were performed using an EOS M280 LPBF system equipped with a 400 W ytterbium fiber laser (beam diameter 100 μm) under an argon atmosphere, without baseplate preheating. To ensure a wide range of thermal conditions and process characteristics, five materials were included in the study: 316L stainless steel, IN625 nickel alloy, CoCr alloy, pure tungsten (W) and pure molybdenum (Mo). Other materials, e.g. aluminum, were not used due to its high infrared reflectivity requiring the use of different neutral density filters. During these experiments, thermal imaging was performed using a dual-wavelength infrared CMOS camera (Stratonics Thermaviz) operating at 725 (λ_1) and 900 (λ_2) nm wavelengths. Each sensor provides a 1024 × 1024 pixel field of view (FOV) corresponding to a spatial resolution of 13.6 μm/pixel. The camera was aligned coaxially with the building platform. Frame rates between 95 and 150 fps and exposure times between 0.01 and 0.05 ms were used. Neutral density filters with an optical density of 0.5 were also applied to prevent the saturation of the sensors.

Ten LPBF process parameter sets were used for building 316L, CoCr and IN625 powders, with the laser power (P) ranging from 80 to 370 W, and the scanning speed (v), from 200 to 1600 mm/s. For pure Mo and W powders, because of their extremely high melting points, only one parameter set was used for each material (Table 2.1). The melting and vaporization temperatures of all five materials are also presented in Table 2.1.

Table 2.1: Process conditions and characteristic temperatures of the materials used

Process conditions					
Materials	IN625	316L	CoCr	Mo	W
Laser power (W)	80-370	154-370	120-350	200	300
Scanning speed (mm/s)	500-1250	600-1600	400-1400	100	100
Linear energy density (J/mm)	0.06-0.74	0.10-0.61	0.09-0.88	2	3
Characteristic temperatures, ^{o}C					
Melting	1350	1400	1330	2623	3422
Vaporization	2913	3000	2930	N/A	N/A

2.5 Dual-Wavelength Camera Working Principle

The ratio pyrometry method is based on Wien's approximation of Planck's law, where the ratio between emitted intensities at two close wavelengths is used to estimate the temperature. For real materials, the emissivity varies significantly with the temperature, phase state, surface conditions, and wavelength. By using two nearby wavelengths and assuming a similar emissivity at both wavelengths, the emissivity term is canceled, allowing temperature estimations without prior emissivity knowledge (2.1) (Penny & John Hart, 2025).

$$\frac{L_{\lambda 1}(T)}{L_{\lambda 2}(T)} = \frac{\varepsilon B_{\lambda_1}(T)}{\varepsilon B_{\lambda_2}(T)} \tag{2.1}$$

where $L_{\lambda}(T)$ is the measured spectral radiance at wavelength λ (m); ε, the spectral emissivity (assumed equal for two close wavelengths λ_1 and λ_2); and $B_{\lambda}(T)$, the blackbody spectral radiance given by Planck's law (2.2):

$$B_\lambda(T) = \frac{2hc^2}{\lambda^5} \cdot \mathrm{e}^{-\frac{hc}{\lambda k_B T}} \tag{2.2}$$

where h is the Planck`s constant (J·s); T, the temperature (K); c, the speed of light (m/s); and K_b, the Boltzmann's constant (J/K).

In principle, the emissivity ratio should be calculated pixel-by-pixel to obtain full temperature maps. However, even small spatial misalignments between the two wavelength channels may introduce significant noise, especially when the camera resolution is limited. As a result, direct pixel-by-pixel ratio computation can lead to locally nonphysical temperature values. For this reason, some authors calculate this ratio for an enclosed area, thus reducing the pixel by pixel-related uncertainties (Scheel et al., 2023; Williams et al., 2019); this last approach will be applied in the present study.

2.6 Calibration Method

Calibration requires establishing a relationship between the measured intensity ratios and the known temperature values. In this study, the liquidus temperature of each of five materials was used as a reference temperature by correlating the width of an individual weld bead (single track) obtained by ex-situ metallographic measurements with the corresponding thermal camera intensity contour. This method has been successfully applied to single wavelengths sensors, allowing the measurements of emissivity values during LPBF of the C103 niobium-based refractory alloy (Nb-10Hf-1Ti) and the validation of numerical simulations (Doubenskaia et al., 2015; Park et al., 2025).

The process starts with capturing the spectral radiance images of a melt pool during the laser pass using two wavelength sensors, λ_1 and λ_2. The acquisition process is followed by image corrections, including the alignment of two wavelength channels, using a rigid transformation approach. Next, dark-frame subtraction is performed by averaging frames acquired before

powder melting and subtracting the resulting pixel-wise background from the recorded intensity images (Feng et al., 2026). After these steps, the intensity profiles can be extracted along (Figure 2.1-A) and across (Figure 2.1-C) the melt pool (Figure 2.1-B).

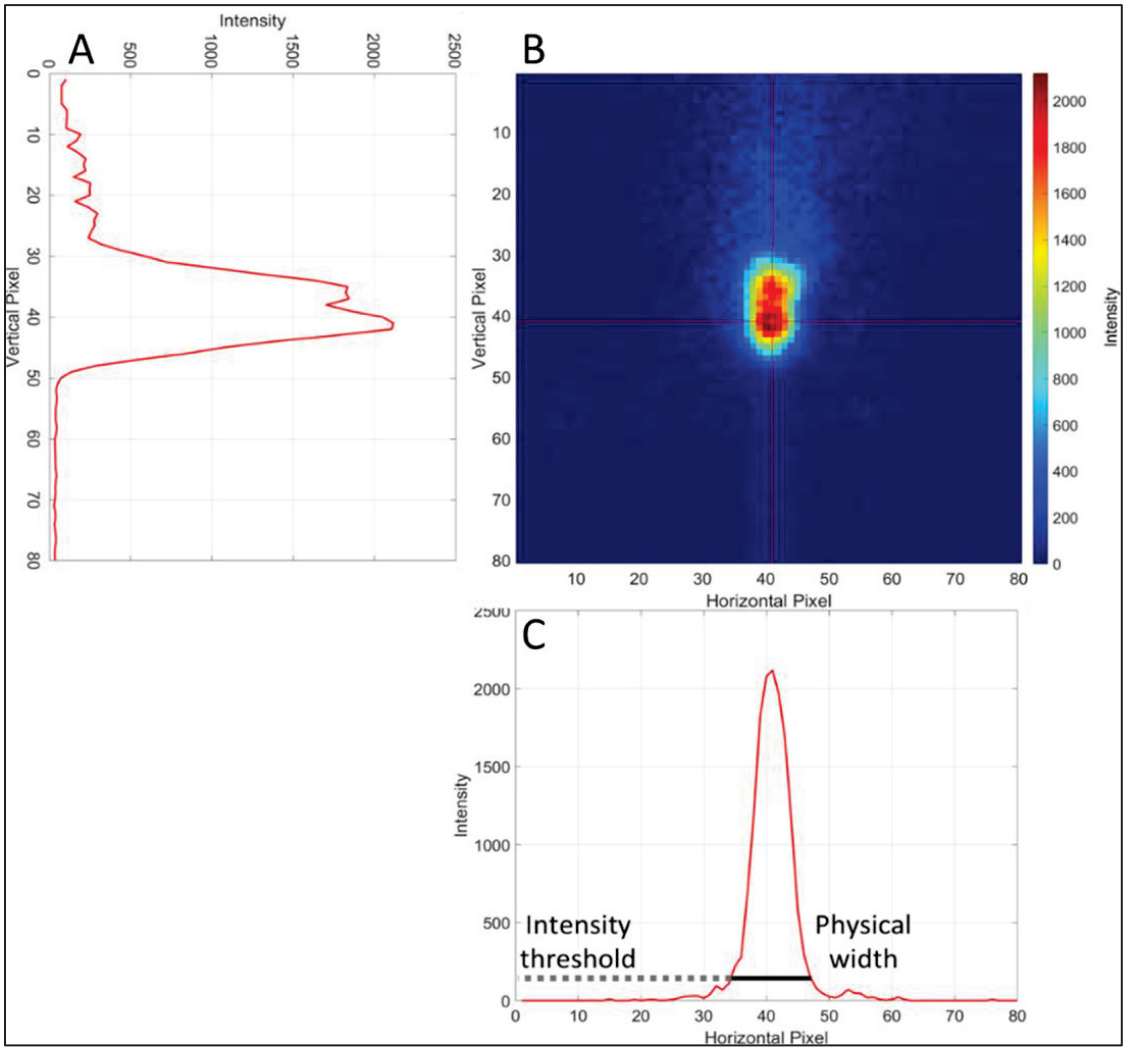

Figure 2.1: Single-track experiment with IN625 (P= 285 W and v = 960 mm/s): (A) vertical intensity profile, (B) melt pool thermal image (λ_1), (C) horizontal intensity profile with the intensity threshold corresponding to a metallography-measured single-track width

It is then considered that for each material and each process condition, the intensity peak width measured across the melt pool image (Figure 2.1-C) must correspond to a single-track width measured by the metallography technique. The intensity thresholds obtained for each of the

wavelengths, λ_1 and λ_2, can therefore be used in Equation (2.1) to calculate the corresponding intensity ratios. Since each single-track width is associated with the melt-pool width, and therefore, the liquidus temperature of a specific material, each measurement provides a specific intensity ratio-temperature pair. By repeating this process for multiple material and building conditions, a calibration curve relating the intensity ratios to the absolute temperatures can be obtained.

2.7 Results

2.7.1 Calibration Curves (Novel And Conventional Approaches)

By analyzing the threshold intensity values obtained for each of the two wavelengths (Figure 2.2a) and the wavelength ratios (Figure 2.2b), it could be seen that for IN625, CoCr and 316L, the intensity threshold for λ_2 is higher than for λ_1, while for Mo and W, it is the other way around. These differences can be explained by the spectral radiance behavior of different materials at different temperatures and wavelengths (Hooper, 2018). Since refractory materials such as Mo and W have significantly higher melting temperatures than their lower melting temperature counterparts, the peaks of their spectral emissions shift toward shorter wavelengths, inverting the measured intensities at wavelengths λ_1 and λ_2.

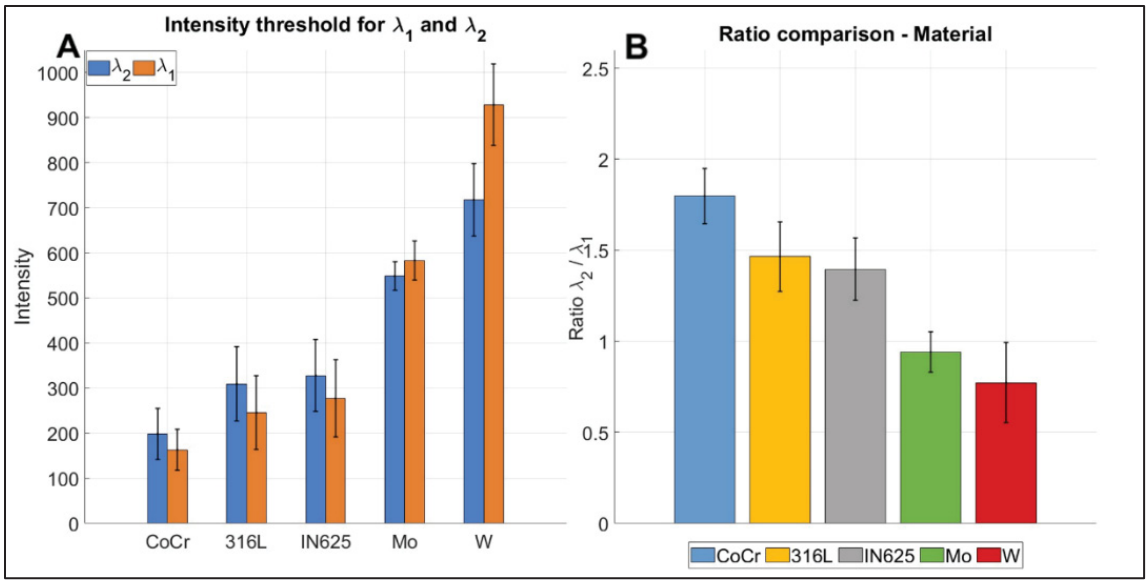

Figure 2.2: (A) Intensity thresholds obtained for each material using two wavelengths, (B) Ratio of spectral radiance, λ_2 / λ_1, for each material

Differences in the intensity ratios of the alloys having close melting temperatures, i.e., CoCr, 316L and IN625, are not significant, and they tend to be minimized in the final calibration curve plotted in Figure 2.3. This calibration curve relates logarithms of the intensity ratios to the inverse temperatures, thus enabling direct temperature estimations.

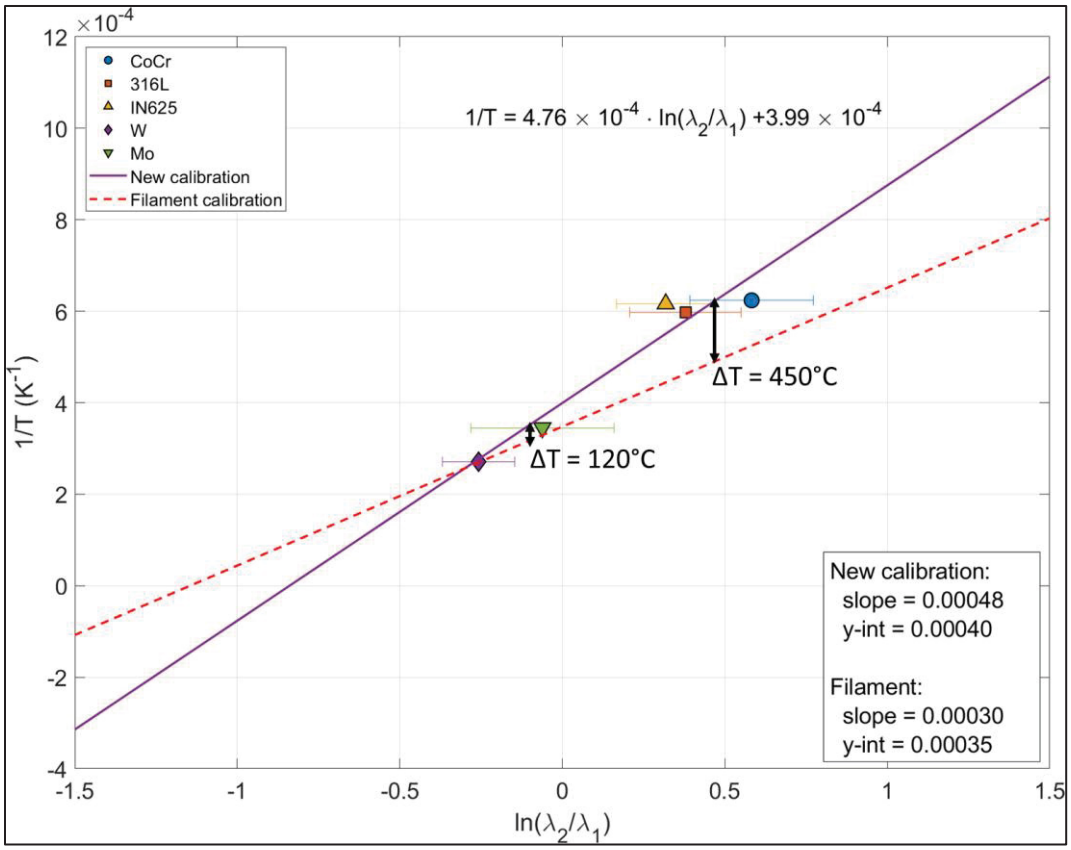

Figure 2.3: Comparison of the single-track measurement-based and tungsten filament-based calibration curves

When this calibration curve is compared with the tungsten filament-based calibration curve (Figure 2.3), a clear difference is observed in the slopes of two curves, with the former being much steeper ($4.76 \times 10^{-4}\ K^{-1}$) than the latter ($3.04 \times 10^{-4} K^{-1}$). This variation directly affects the calculated melt pool contour temperatures. For high melting point materials such as W and Mo, temperature differences between the two calibration methods are relatively small and amount to ~120 °C (5% difference). However, for the lower melting point materials, such as 316L, CoCr, and IN625, temperature differences between the two calibrations approach ~450 °C (20% difference). This means that the results provided by both calibrations are material-dependent: they are close for high melting point materials, such as tungsten and Mo, but significantly different for their lower melting point counterparts.

2.7.2 Temperature Comparison

Temperature profiles obtained via the use of both calibration curves across and along the melt pool are plotted in Figure 2.4 to allow their comparison. These images correspond to the case when the laser was on; images for which the material was heated, but the melt pool was not yet observed, were filtered out. It can be seen that the tungsten filament-based calibration systematically overestimates the melt-pool peak temperatures. At a 90% intensity level, the average maximum temperature reaches approximately 3430 °C for 316L and 3386 °C for IN625, which exceeds the vaporization temperature of each material by ~15%. After the novel calibration approach is applied, the average maximum temperatures decrease to 3144 °C for 316L and 3132 °C for IN625, which are close to the corresponding vaporization temperatures and physically consistent with the recoil pressure and Marangoni effects (J. Liu & Wen, 2022). Such a maximum temperature analysis could not be performed for W and Mo, since the extremely high melting temperatures caused pixel saturation in central parts of the thermal images.

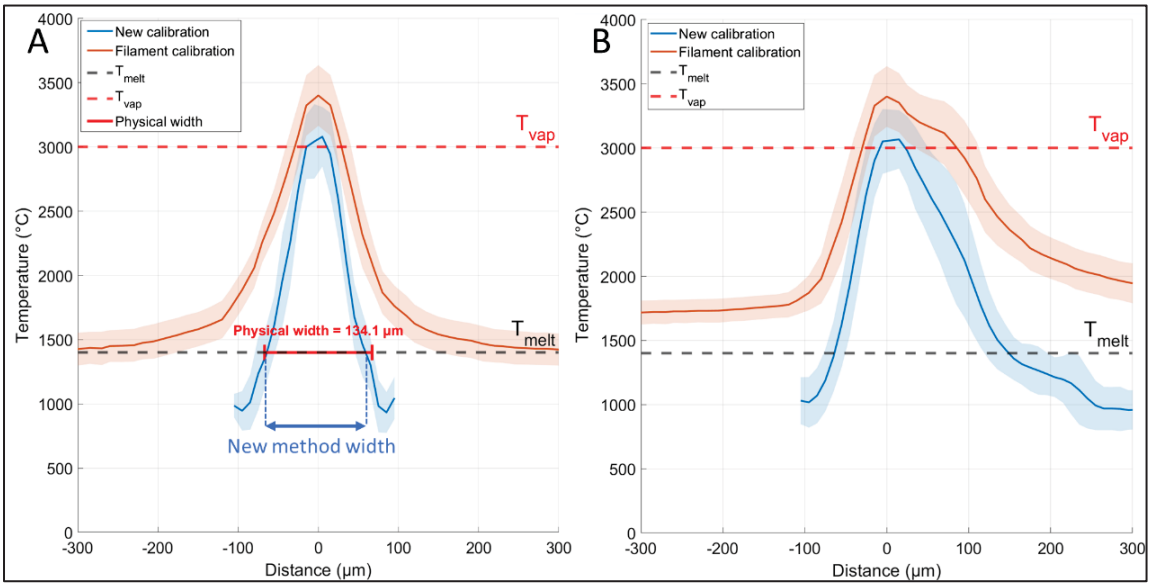

Figure 2.4: Temperature profiles across the melt-pool comparing two calibration methods: A) width and B) length for 316L with $P = 215$ W and $v = 913$ mm/s

Additionally, with the tungsten filament-based calibration, regions outside the melt pool often exhibit temperatures exceeding the melting point, which is physically unrealistic and makes the melt-pool geometry extraction impossible. Similar overestimations have been reported in the literature, where unrealistically high temperatures were occasionally attributed to spatter or plume interference along the optical path (Hooper, 2018). In contrast, the proposed calibration consistently produces background temperatures below the melting temperature for all the investigated materials, allowing melting points to be used as thresholds for the melt-pool dimensional measurements. Finally, in the present work, the use of spatially averaged temperature values reduced the likelihood of localized artifacts affecting the measurements. Measurements in the lower-temperature regions remained limited by the camera calibration range (above ~1000 °C) and by the acquisition frame rate, which prevented the measurement of cooling rates exceeding ~40 °C/µs.

2.7.3 Correlation Between In-Situ And Ex-Situ Melt Pool Measurements And Numerical Simulations

The melt-pool widths extracted from thermal images acquired during processing of 316L, CoCr, and IN625 were compared with their corresponding single-track widths obtained from a simplified numerical simulation model (Leclercq & Brailovski, 2024) (Figure 2.5A). Across all materials, the in-situ measurements show good agreement with the simulated results, yielding a root mean square error (RMSE) of ~15 µm, which is smaller than 1.5 pixels, in combination with a regression slope (a_1) of 0.80. However, due to the instability and complexity of the physics in the process, the scatter is significantly high, with values up to 100 µm.

Furthermore, in-situ two-wavelength thermal imaging can be used for melt pool length assessment (Figure 2.5B). This parameter provides indirect information about solidification and cooling behavior and enables direct comparisons with simulation-predicted geometries and temperature distributions. Using the simplified melt pool numerical simulation model described in (Leclercq & Brailovski, 2024), it was verified that the thermal camera-measured melt pool lengths exhibit a strong correlation with their simulated equivalents. The comparison

resulted in an RMSE smaller than 37 μm (less than 3 pixels) and a_1 of 1.08, indicating good agreement between the experimental measurements and the numerical predictions. These results additionally demonstrate that the proposed calibration method provides consistent and physically meaningful melt pool geometric measurements in LPBF.

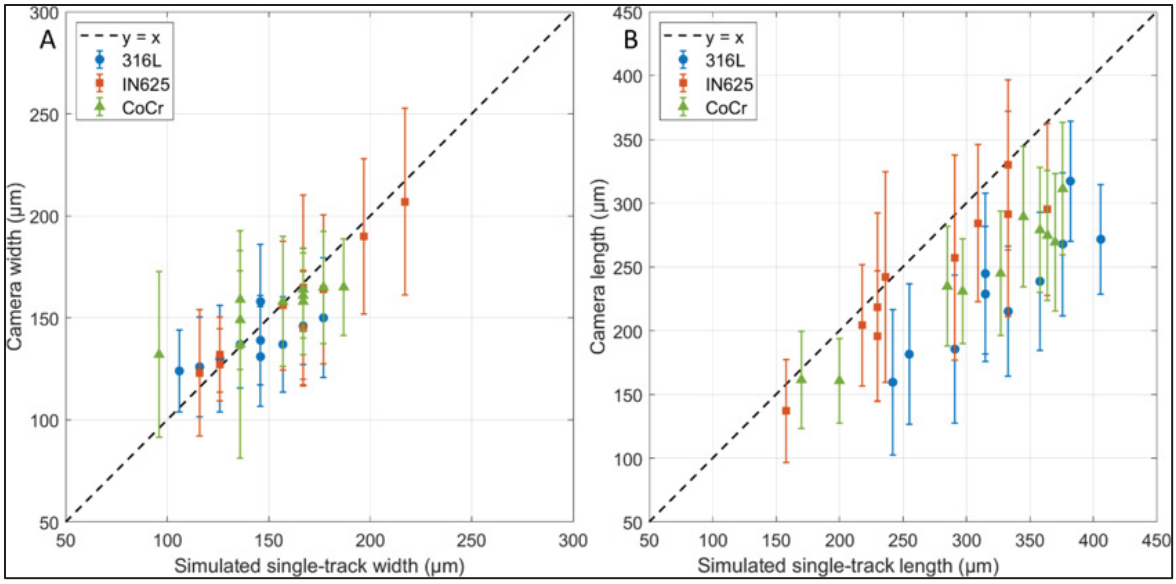

Figure 2.5: Comparison between thermal camera and numerically simulated melt pool: A) widths and B) lengths

2.7.4 Melt Pool Thermal Field Image

Finally, each intensity image can be converted into a temperature field using the calibration procedure described above. This conversion enables the reconstruction of spatially resolved thermal maps, representing the temperature at each pixel of the melt pool region. Such temperature fields are useful for analyzing the vaporization behavior, estimating cooling rates, and evaluating other temperature-dependent phenomena. Figure 2.6 illustrates the results of conversion from the raw intensity images to the corresponding temperature maps, following the steps previously described in this work.

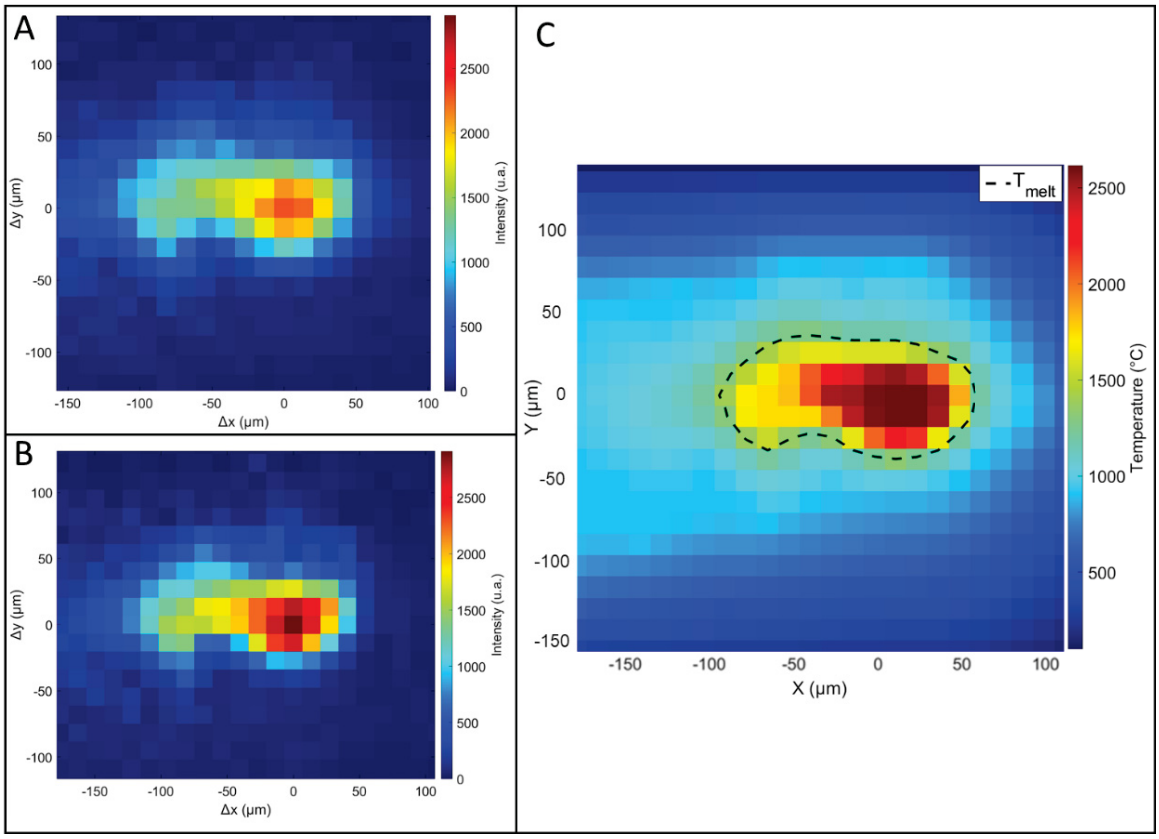

Figure 2.6: Spectral radiance image in (A) λ_1 and (B) λ_2, (C) Final temperature image for 316L at P= 215 W and v= 930 mm/s

2.8 Conclusion

To obtain a new calibration curve, five metallic materials were processed using variable fusion regimes. Next, light intensities obtained during fusion of these materials using a two-wavelength camera were correlated with their corresponding melting temperatures via the post-process measurements of single-track widths. This calibration allowed measuring temperature fields that were physically more realistic than those obtained using the conventional tungsten filament-based calibration approach. The new calibration procedure significantly reduced the peak temperature overestimations and enabled reliable melt-pool dimensional measurements directly from thermal images. The methodology provides a practical and physically sound calibration strategy applicable to multi-material LPBF monitoring environments.

CHAPTER 3

RELIABILITY OF THERMAL CONDUCTION-BASED MELT POOL SIMULATIONS USING IN-PROCESS THERMAL CAMERA AND POST-PROCESS SINGLE-TRACK MEASUREMENTS

Matheus Soares [a], Donatien Campion [a], Aurore Leclercq [a], Alena Kreitcberg [a], Vladimir Brailovski [a]

[a] Département de Génie mécanique, École de Technologie Supérieure, 1100 Notre-Dame Ouest, Montréal, Québec, Canada H3C 1K3

Article published in *Applied Sciences*, May 2026
https://doi.org/10.3390/app16125850

3.1 Preface

With a physically consistent calibration established in chapter 2, the dual-wavelength thermal camera was then used as a quantitative measurement tool, not only for temperature visualization, but also for extracting melt pool surface geometries (width, length and area) directly from the thermal images using the material liquidus temperature as a contour threshold. This second article combines these in-situ camera measurements with ex-situ metallographic cross-sections of the same single tracks to simultaneously access all three melt pool dimensions and assess the reliability of a simplified analytical thermal conduction model used for process parameter optimization. The three alloys studied: 316L, IN625, and CoCr, are part of the materials covered by the calibration developed in Chapter 2, ensuring that the camera measurements used as experimental reference rest on a validated physical basis. The cross-validation between the two experimental techniques through their shared width measurement further confirms that the combined methodology is internally consistent, and that the observed discrepancies between model and experiment reflect genuine physical limitations of the conduction only formulation rather than measurement issues.

3.2 Abstract

Laser Powder Bed Fusion (LPBF) is a complex manufacturing process that depends on precise control of printing parameters and melt pool geometry, which directly influence defect formation and final part quality. This study evaluated the reliability of a simplified thermal conduction-based melt pool model by combining post-process metallographic analysis with in-situ dual-wavelength infrared thermal imaging. Experimental data were obtained through single-track printing on 316L, IN625, and CoCr alloys across a wide range of parameters. The simulated melt pool length showed strong agreement with thermal camera measurements (R^2_{adj} > 0.78), while the width showed moderate but consistent correlation (R^2_{adj} > 0.52). For melt pool depth, the model systematically deviated due to its inability to capture keyhole melting, although a strong linear correlation was still observed (R^2_{adj} > 0.86). Cross-validation between metallographic measurements and thermal imaging revealed only a 6–9% discrepancy, confirming the reliability of both methods and the potential of dual-wavelength cameras for industrial process monitoring. Overall, the model proves to be a reliable tool for predicting melt pool surface geometry specifically within the conduction melting regime, while its predictive capability degrades significantly in the keyhole regime, where simulated peak temperatures reach up to 7000 °C and melt pool depth errors escalate due to the disregard of recoil pressure, liquid and vapor dynamics.

Keywords: Additive manufacturing; Laser Powder Bed Fusion; In-situ monitoring; Dual-wavelength sensor; Analytical modeling; Metallography measurements.

3.3 Introduction

Laser powder bed fusion (LPBF) is one of the most widely used metal additive manufacturing technologies due to its ability to produce near-net-shape parts with complex shape, simplify post treatments and reduce material wastage (J. Wang et al., 2023). It consists of using a laser to selectively melt a powder bed, layer by layer, according to the part geometry. However, controlling the final part quality, density, and microstructure is quite a complex undertaking (J. Wang et al., 2023). Common major defects observed in LPBF parts include (a) keyhole

pores, which occur because of high laser energy inputs and low scanning speeds, which in turn creates conditions for gas entrapment, and (b) lack-of-fusion defects, which occur when overlaps between neighboring laser tracks and printed layers are limited and thus leave zones of unmelted powder particles (Carter et al., 2014; Khairallah et al., 2016; J. Wang et al., 2023). Both these defects are responsible for process-induced porosity and consequently a lower mechanical resistance of printed parts (Shrestha & Chou, 2022; X. Yang et al., 2023). In practice, the melt pool geometry (width, length, and depth) and temperature distribution constitute the links between process parameters and process-induced defects, and small changes in laser power, scanning speed, hatching distance and layer thickness can switch the process between the optimum and suboptimum printing regimes (Shrestha & Chou, 2022; J. Wang et al., 2023; X. Yang et al., 2023). Moreover, these melt pool characteristics determine cooling speeds and thermal gradients accompanying the part forming process and thus affect material solidification dynamics, and therefore, the microstructure and mechanical properties of printed parts. To improve control over the process and the quality of printed parts, a plethora of in situ and ex situ monitoring methods can be used.

As far as the in-situ process monitoring techniques are concerned (Chen et al., 2023; Mitrašinović et al., 2025; R. Wang et al., 2022), contact sensors such as thermocouples cannot be used directly as they would interfere with the process (Mitrašinović et al., 2025). As such, contactless in situ monitoring methods are frequently employed. Some of them are based on the use of high-speed video cameras, which assist in observing the behavior of the melt pool and the fumes released during laser-metal interaction (Chen et al., 2023; R. Wang et al., 2022). Among temperature measurement equipment, one can distinguish pyrometers which can measure the temperature within a small, defined space using point, cross, or line modes (Mitrašinović et al., 2025). Thermal cameras, on the other hand, can measure temperatures over a larger field of view, capturing the entire extent of a melt pool, recording high-speed 2D images (typically up to tens of kHz, depending on windowing and hardware) (Mitrašinović et al., 2025; R. Wang et al., 2022), but they cannot be used for melt pool depth assessment. Conversely, the depth and width of a single laser track, being representative of the depth and width of a melt pool, can be measured using ex situ metallographic techniques (Leclercq &

Brailovski, 2024; Letenneur et al., 2019; Schuöcker, 1998; Shrestha & Chou, 2018). Therefore, an obvious solution for measuring all the dimensions of a melt pool would involve a combination of in situ and ex situ methods (Leclercq & Brailovski, 2024; Shrestha & Chou, 2018; R. Wang et al., 2022).

Complementary to experimental techniques, simulations offer predictive links between process parameters and the melt pool geometry. Analytical or semi-analytical models based on the calculations of a thermal field created by a moving heat source provide quick estimates of the melt-pool width, length, and depth in conduction melting mode (Letenneur et al., 2019; Schuöcker, 1998). To be reliable, these models must be adapted to specific laser scanning and powder bed conditions, including the laser beam intensity, powder bed absorptivity, specific heat capacity and thermal conductivity (Bala et al., 1989; Letenneur et al., 2019; Sumin Sih & Barlow, 2004; Tolias, 2017). For component-level planning and rapid design exploration, reduced finite element (FE) solvers, including commercial tools, offer practical setup time and cost trade-offs and can be used to predict the thermal history and distortions of a part to be printed (Letenneur et al., 2019). When more detailed physics-based insights are needed, high-fidelity LPBF process models that consider the recoil pressure, the Marangoni convection, vapor dynamics, and conduction-to-keyhole transition phenomena can be used, albeit at a much higher computational cost (X. Yang et al., 2023).

Some studies have already analyzed the accuracy of melt pool simulations using thermal camera observations (Ashby et al., 2022; Mahmoudi et al., 2018), while others have compared thermal camera observations with dimensions of solidified laser tracks obtained using conventional metallographic techniques (Goossens & Van Hooreweder, 2021; Park et al., 2025). However, no research has combined the use of ex situ metallographic measurements with in-situ thermal camera observations to validate the results of melt pool simulations. To bridge this gap, the present study uses a combination of two experimental techniques, namely, in situ dual-wavelength infrared thermal camera observations and ex situ single-track metallography, to assess the reliability of a simplified Gaussian heat source model adapted from (Schuöcker, 1998) in terms of its capacity to predict the width, length, and depth of a

melt pool in LPBF. The scope of this work includes some of the most commonly used LPBF metallic materials: 316L, IN625, and CoCr alloys, shaped using variable laser powers and scanning speeds.

To the best of our knowledge, this is the first study to combine these three approaches in a single experimental campaign: analytical simulation, in situ dual-wavelength thermal imaging, and ex situ metallography. The dual-wavelength calibration approach developed here enables the emissivity-independent extraction of melt pool width, length, and temperature field directly from the thermal image, while metallography provides the complementary melt pool depth and width measurements. Altogether, these techniques deliver a complete dataset for the melt pool model assessment that covers all three melt pool dimensions plus the surface temperature field, with built-in multi-material cross-validation on the shared melt pool width measurements.

3.4 Materials and Methods

3.4.1 Melt Pool Simulations (Analytical Model)

A simplified thermal conductivity-based numerical model of the LPBF process (Leclercq et al., 2025; Leclercq & Brailovski, 2024; Schuöcker, 1998) used in this work was developed in the MATLAB software (R2022b, MathWorks, USA) environment. This model is used to assess melt pool dimensions and is based on analytical calculations of a temperature field generated by a moving Gaussian heat source in a semi-infinite solid (3.1):

$$T(x,y,z) = T_0 + \frac{AP}{kr_f\pi^{\frac{3}{2}}}\int_{+\infty}^{0}\frac{1}{1+\tau^2}exp(C)\,d\tau \tag{3.1}$$

With

$$C = -\left(\frac{\tau^2}{1+\tau^2}\right)\left(\left(\xi - \frac{Pe}{2\tau^2}\right)^2 + \eta^2\right) - \tau^2\zeta^2 \tag{3.2}$$

$$\xi = \sqrt{2}\frac{x}{r_f}\ ; \eta = \sqrt{2}\frac{y}{r_f}\ ; \zeta = \sqrt{2}\frac{z}{r_f}\ ; Pe = \frac{r_f v}{2\sqrt{2}\alpha}\ ; \tau = \frac{r_f}{2\sqrt{2\alpha dt}}\ ; \alpha = \frac{k}{\rho c_p} \tag{3.3}$$

where T_0 is the baseplate temperature (K); A, the absorptivity; P, the laser power (W); k, the thermal conductivity (W/ (m·K)); r_f, the laser beam radius (m); Pe, the Peclet number; v, the scanning speed (m/s); α, the thermal diffusivity (m^2/s); ρ, the density (kg/m^3); c_p, the mass heat capacity (J/ (kg·K), and dt, the time (s).

The absorptivity (3.4) is calculated using the Hagen-Rubens model (Hügel & Dausinger, 1998) approximating the material absorptivity using its electrical resistivity value:

$$A = 0.365\left(\frac{R_s}{\lambda}\right)^{0.5} \tag{3.4}$$

Because the raw material is in the form of a powder bed rather than a dense solid, some variables need to be corrected, namely:

The density, using (3.5):

$$\phi = 1 - CBD \tag{3.5}$$

where ϕ is the fractional porosity and CBD is the coefficient of bulk powder density (without units).

The powder bed absorptivity is calculated according to (Sih & Barlow, 2004), where the powder bed is assumed as a porous surface composed of spherical bodies and holes, all having

the same temperature. Considering the bodies as “gray” without transmission of radiation, absorptivity is then equal to emissivity (A = ϵ). Thus, the powder bed absorptivity can be calculated using equations (3.6-3.8):

$$\epsilon_{powder} = S_h \epsilon_h + (1 - S_h)\epsilon_s \tag{3.6}$$

with

$$\epsilon_s = A \tag{3.7}$$

and

$$S_h = \frac{0.908\phi^2}{1.908\phi^2 - 2\phi + 1} \; ; \; \epsilon_h = \frac{\epsilon_s \left(2 + 3.082 \left(\frac{1-\phi}{\phi}\right)^2\right)}{\epsilon_s \left(1 + 3.082 \left(\frac{1-\phi}{\phi}\right)^2\right) + 1} \tag{3.8}$$

where ϵ_{powder} is the powder emissivity (absorptivity); S_h, the surface fraction occupied by pores; ϵ_h, the pores emissivity; ϵ_s, the emissivity of a bulk material, R_s; the electrical resistivity of the material (Ω·m), and λ, the laser wavelength (m).

The thermal conductivity (3.9) is calculated following the work of (Kang et al., 2013):

$$k_{powder} = k_s (1 - \phi)^{\frac{4}{3}} \tag{3.9}$$

where k_{powder} and k_s are the thermal conductivities (W/(m·K)) of a powder bed and a bulk material, respectively.

In this model, the material properties (melting temperature; material density; powder bed density; specific heat capacity; thermal conductivity and electrical resistivity) are considered constant despite the fact that, during LPBF, their values vary from those at room temperature to those near the melting point and beyond. Since it was proven in a previous work (Leclercq et al., 2025) that considering the material properties at 80% of the melting temperature (0.8Tmelt) leads to the smallest discrepancies between calculated and measured melt pool sizes, this approach was adopted.

Using this model in the present work, in each cell of a parallelepiped domain (X = [0; 0.6], Y = [−0.25; +0.25] and Z = [−0.3; 0], all dimensions in mm, with N = 100 divisions for each axis), temperature values can be calculated. These temperatures are then compared to three material-specific threshold values: a) Vaporization temperature (T_{vap}); b) Melting temperature (T_{melt}), and c) Heat-affected zone (HAZ) temperature (T_{HAZ}), where ($T_{HAZ} < T_{melt} < T_{vap}$). This operation allows delimitating the vaporization, melting and HAZ zones shown in Figure 3.1a, and more specifically, to extract the melt pool dimensions (width, depth and length) shown in Figure 3.1b.

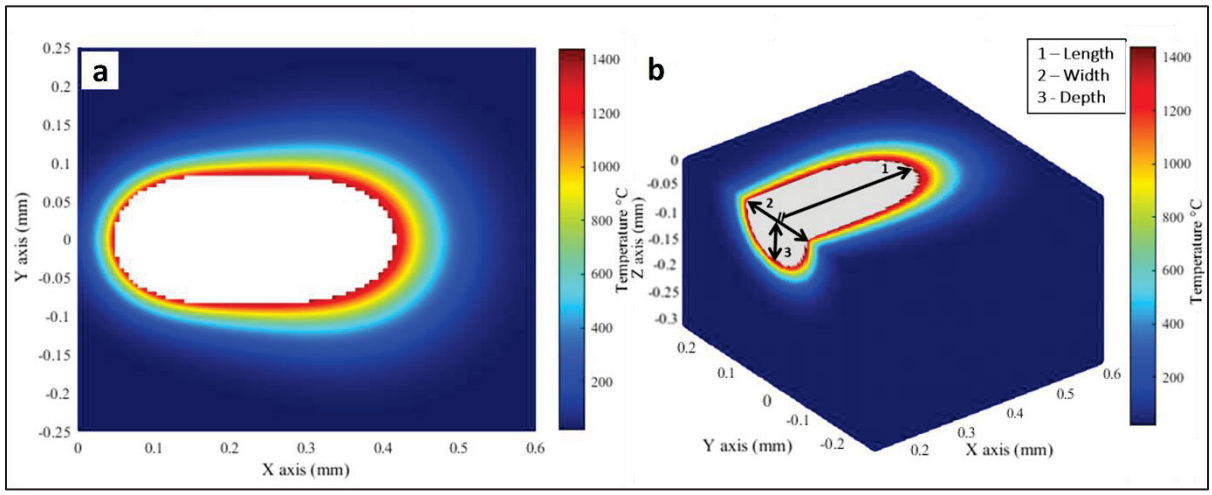

Figure 3.1: Simulated melt pool thermal field (316L at 215 W and 930 mm/s) showing: a) different temperature zones surrounding the melt pool; b) 1-width, 2-length and 3-depth of the melt pool; the temperature in the white zone is above the melting point

To assess the reliability of numerical simulations, the melt pool width, length and depth must be experimentally measured. As was previously mentioned, no single experimental technique can provide all these dimensions at once. On the one hand, the in-process thermal camera allows measuring melt pool widths and lengths, and on the other, post-process single-track metallographic analysis allows measuring melt pool depths and widths. In the framework of this study, both experimental techniques are combined to provide a complete set of experimental data (Table 3.1).

Table 3.1: Melt pool simulation and validation experiments (✓: measured/predicted; −: not applicable)

	Melt pool dimensions		
	Width	Length	Depth
Simulations	✓	✓	✓
Post-process single-track metallography	✓	-	✓
In-process thermal observations	✓	✓	-

3.4.2 Materials

Three powder lots supplied by EOS (EOS GmbH, Munich, Germany) were used for printing: EOS Stainless Steel 316L-4441, EOS Nickel Alloy IN625 and EOS Cobalt Chrome MP1. The chemical composition and the generic particle size distributions (PSD) are given in Table 3.2.

Table 3.2: Chemical compositions (ASTM) and generic particle size distributions of three powder lots

Chemical composition (wt.-%)															PSD (µm)
Material	Fe	Cr	Ni	Mo	Nb + Ta	Co	Mn	Si	Al	Ti	C	N	P	S	
IN625	≤ 5.00	20.0 - 23.0	Balance	8.0 - 10.0	3.15 - 4.15	-	≤ 0.50	≤ 0.50	≤ 0.40	≤ 0.40	≤ 0.10	-	≤ 0.015	≤ 0.015	15 - 65
316L	Balance	17.0 - 19.0	13.0 - 15.0	2.25 - 3.00	-	-	-	-	-	-	≤ 0.03	≤ 0.10	-	-	20 - 65
CoCr	≤ 0.75	26.0 - 30.0	-	5.0 - 7.0	-	Balance	≤ 1.00	≤ 1.00	-	-	≤ 0.25	≤ 0.25	-	-	15 - 45

The material properties used for the simulations are shown in Table 3. The powder bed densities were approximated to the conditioned bulk densities (CBDs) obtained with an FT4 powder rheometer (Freeman Technology, Malvern, UK). Furthermore, for 316L and IN625, the material properties were extracted from JMatPro software (v 14.1, 2023), while for Co-Cr, they were extracted from (Carpenter Technology Corporation, Reading, PA, USA. (2020). CarTech® BioDur® CCM® Alloy—Technical Data Sheet. CRS Holdings Inc.). In all the cases, the property values correspond to ~$0.8T_{melt}$ conditions.

Although 316L, IN625, and CoCr have different thermophysical properties (e.g., thermal conductivity, absorptivity, density, and heat capacity), they exhibit relatively close melting and evaporation temperatures. This means that the phase change thresholds (sol-id–liquid and liquid–vapor) occur within a similar temperature range for all three materials. Since the present model does not explicitly account for phase change effects, selecting materials with comparable melting and evaporation temperatures helps minimize the in-fluence of phase transitions on the simulation results. Consequently, differences observed between materials can primarily be attributed to variations in their thermophysical properties rather than in their phase change behavior.

Table 3.3: Coefficient of conditioned bulk density extracted from FT4 and material properties at $0.8T_m$ extracted from JMatPro software and Carpenter Datasheet; absorptivity is calculated using equations (3.6)-(3.9)

Material	State of Matter	CBD	Melting temperature (°C)	Density (kg/m^3)	Specific Heat Capacity (J/(kg·K)	Thermal Conductivity (W/(m·K))	Electrical Resistivity (nΩ·m)	Absorptivity (%)
IN625	Dense	1	1350	8440	642	27.2	130	40
	Powder	0.56		4773		13.8		53
316L	Dense	1	1400	7485	656	28.5	126	40
	Powder	0.59		4413		14.4		53
CoCr	Dense	1	1330	8407	594	32.4	99	35
	Powder	0.58		4873		15.6		50

3.4.2.1 Printing experiments

Single-track printing experiments were carried out on stainless steel baseplates without preheating, using an EOS M280 LPBF system equipped with a 400 W ytterbium fiber laser (beam radius r_f = 50 μm), in an inert argon atmosphere. For each material, ten printing parameter sets (P0, P1, P2… P9) were considered, with the laser power varying from 80 to 370 W and the scanning speed varying from 200 to 1600 mm/s, as shown in Table 4. Note that the printing parameter sets recommended by the manufacturer (optimized) are tagged as P0. To illustrate the entire printing plan for one of the three materials, 316L, all ten parameter sets are plotted in Figure 3.2a in the linear energy density (*LED*)–scanning speed (v) space coordinates.

$$LED\ (J/mm) = \frac{P}{v} \tag{3.10}$$

Note that such a representation conveniently combines the linear energy density and scanning speed terms. The first term (*LED*) is commonly used in welding to control the bead geometry, while its combination with the second term (v) allows delimitation of the process window

framed by the minimum and maximum powers of a laser source, since P(W)=LED (J/mm)·v(mm/s).

For each material, one 10 × 10 mm base prismatic specimen containing ten vertically connected zones, each 3 mm in height and with a 40 μm layer thickness, was printed, resulting in approximately 75 layers per parameter (see Figure 3.2b); each zone corresponded to one of the ten printing parameter sets presented in Table 3.4.

Table 3.4: Printing parameters for each of the study materials (P0 sets correspond to manufacturer's recommendations); LED is calculated using (3.10)

	IN625			**CoCr**			**316L**		
Parameter	Power (W)	Speed (mm/s)	*LED* (J/mm)	Power (W)	Speed (mm/s)	*LED* (J/mm)	Power (W)	Speed (mm/s)	*LED* (J/mm)
P0	285	960	0.30	290	950	0.30	215	930	0.23
P1	370	500	0.74	290	750	0.39	215	600	0.36
P2	285	500	0.57	350	950	0.37	335	930	0.36
P3	194	500	0.39	121	400	0.30	265	930	0.28
P4	370	960	0.39	228	750	0.30	139	600	0.23
P5	147	500	0.29	334	1100	0.30	300	1300	0.23
P6	370	1250	0.30	290	1100	0.26	370	1600	0.23
P7	80	500	0.16	200	950	0.21	154	930	0.17
P8	150	960	0.16	290	1400	0.21	215	1300	0.17
P9	200	1250	0.16	120	950	0.17	215	1600	0.13

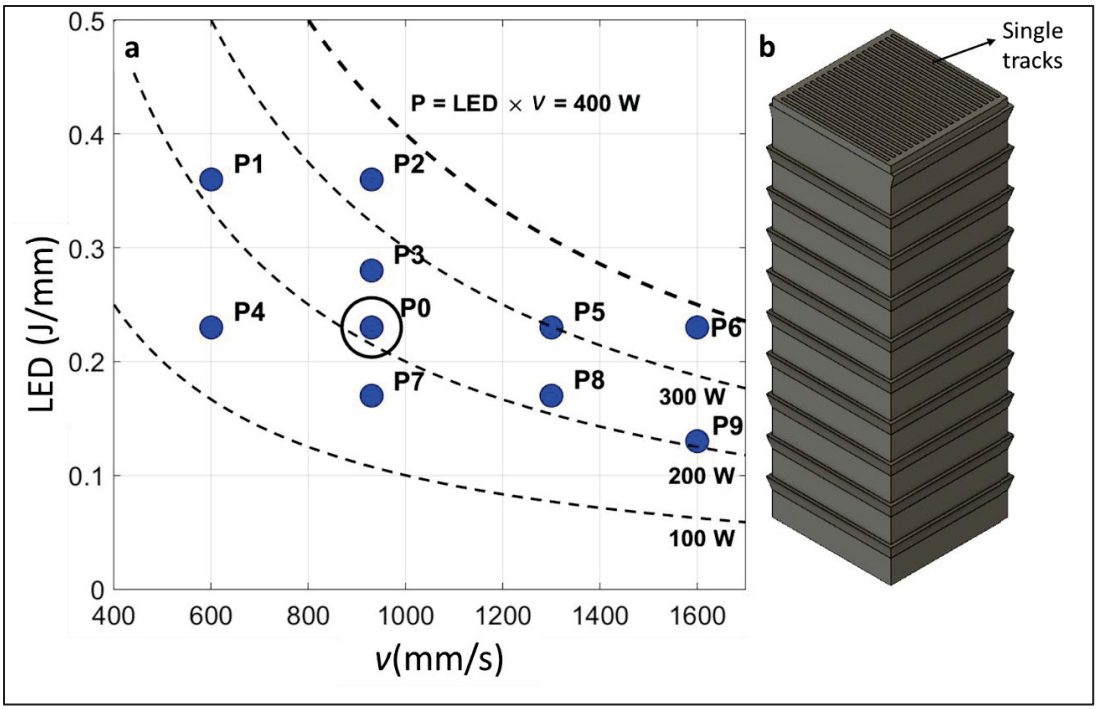

Figure 3.2: a) Plan of experiments in the *LED-v* space coordinates defined for 316L (P0 corresponds to the manufacturer-recommended process conditions; b) printing strategy illustration

3.4.2.2 In-process thermal field measurements

To capture the thermal radiation emitted during the laser-powder interactions as part of the printing process, a dual-wavelength infrared camera (Stratonics Thermaviz, Orange County, CA, USA) was used. The system operates with 725 nm (λ_1) and 900 nm (λ_2) wavelength sensors, each with a 14 × 14 mm^2 (1024 × 1024 pixels) field of view and a 13.6 µm/pixel spatial resolution. The camera was aligned on-axis with the build, as shown in Figure 3.3. To ensure sufficient detection sensitivity for the materials and processing conditions investigated in this work, the acquisition frame rate was set between 95 and 150 frames per second (fps), while the exposure time varied between 0.01 and 0.05 ms. Neutral density filters (NDFs) with an optical density of 0.5 were used to prevent sensor saturation.

The images obtained were processed using custom MATLAB routines. First, the background noise was removed using the dark-frame subtraction method (Gurrala et al., 2023), followed

by a manual rigid registration to minimize the displacement between each pixel across channels. For each frame, an 80 × 80 pixel region of interest (ROI) was extracted around the maximum intensity value to reduce memory usage and improve visualization (Figure 3.4a). Horizontal and vertical intensity profiles were also extracted across and along the lines corresponding to the maximum intensity pixels to characterize thermal gradients across and along the melt pool, respectively (Figure 3.4b).

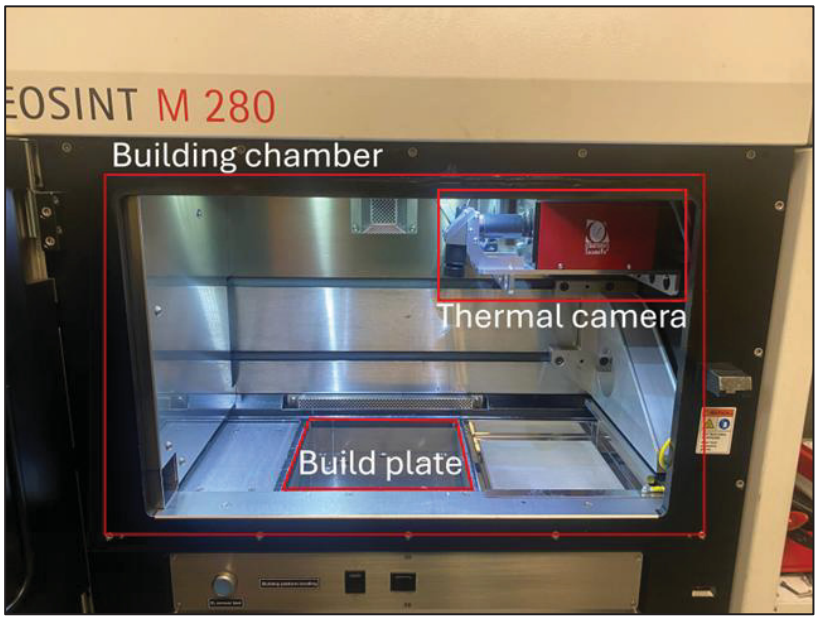

Figure 3.3: Equipment layout inside an EOS M280 building chamber

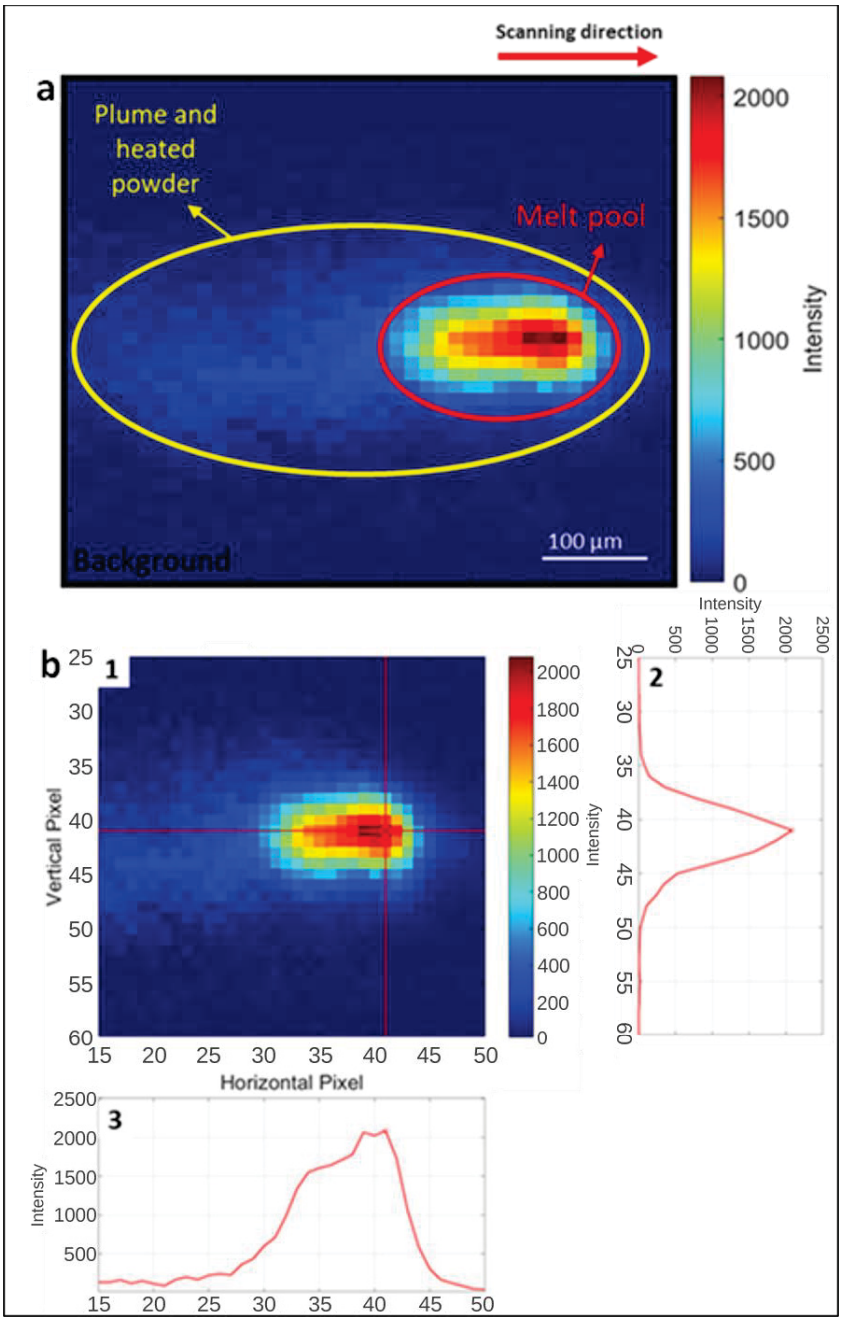

Figure 3.4: a) Segmentation of the intensity image, b) - Melt pool image (1) with corresponding intensity profiles across (2) and along (3) the melt pool; image taken from 316L-P0 using λ_1 =725 nm sensor

3.4.2.3 Conversion of two wavelength intensity values into their temperature equivalents

Plotting the inverse temperature against a logarithm of the intensity ratio yields a straight line, whose slope and intercept are used as calibration constants (Figure 3.5). The temperature T is then given by:

$$\frac{1}{T} = A\, ln\, R + B \tag{3.11}$$

where A and B are the constants corresponding to a linear regression (Mitchell et al., 2020) obtained by single-track calibration experiments on five metallic materials whose melting temperatures cover a 1500-3600 °C temperature range; R is the average intensity ratio obtained from a defined region of the powder bed. This relation allows directly obtaining the temperature value from a known intensity ratio based on the ratio pyrometry theory.

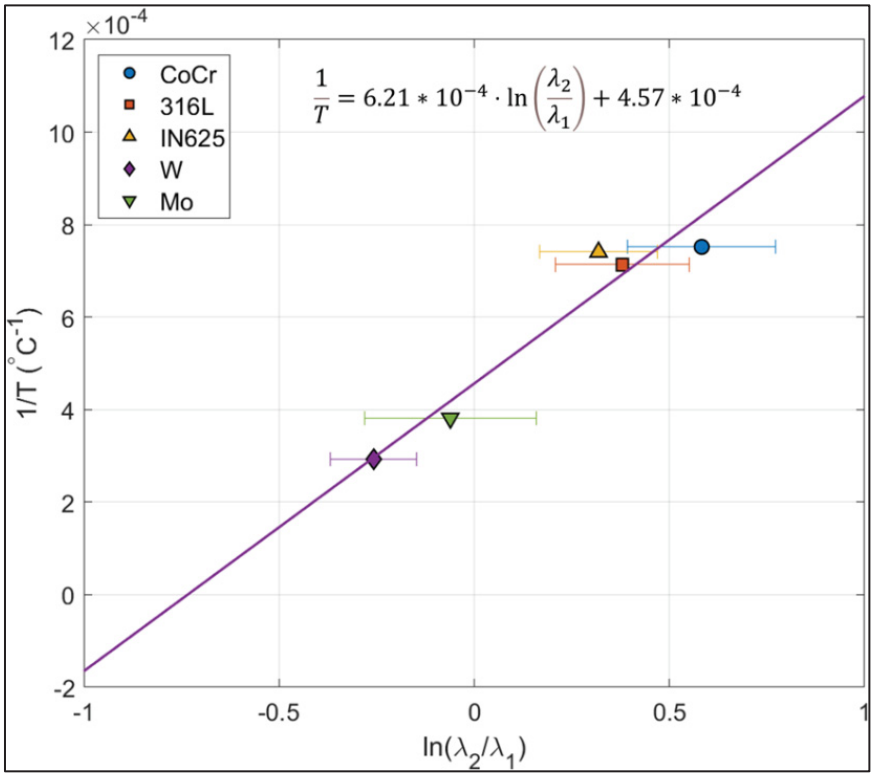

Figure 3.5: Calibration curve based on the melting points of a selected group of metallic materials in the 1500 - 3600 °C temperature range (W, Mo, CoCr, IN625, and 316L)

Note that direct pixel-by-pixel computations of the intensity ratio produce noisy temperature maps, mainly due to small misalignments between the wavelength channels, and lead to non-physical local temperature values. In this study, similar to (L. Wang et al., 2009), temperature isolines and particularly isotherms corresponding to the materials' melting points were used to determine the melt pool contours in each frame acquired. To this end, isolines corresponding to 90, 70, 50, 30, 10 and 5% fractions of the maximum λ_1 intensity images were defined, avoiding overlapping regions and excluding background pixels. Next, for each isoline, the corresponding pixel positions were used to sample the λ_2 image and compute the $R= \lambda_1/\lambda_2$ intensity ratio. The calibration curve was then used to convert the average intensity ratio along each isoline into an effective temperature and to plot the temperature field surrounding the melt pool.

Finally, for each temperature level, the distance from the peak intensity was computed for all the points of an isoline, and the corresponding melt pool widths and lengths were extracted. By plotting the geometric dimensions against the temperature, it was possible to identify regions associated with the vaporization, melting, and heat-affected (HAZ) zones shown in Table 3.5. Figure 3.6 contains an example of the point cloud used for the melt pool measurements applied to LPBF of 316L, where each color corresponds to one of the intensity isoline levels (5 - 90% of the peak λ_1 intensity).

Table 3.5: HAZ, melting and evaporation values for each material used (316L, IN625 and CoCr)

Material	**Characteristic temperatures (°C)**		
	HAZ (0.5 T_{melt})	Melting (T_{melt})	Evaporation (T_{vap})
IN625	675	1350	2913
316L	700	1400	3000
CoCr	665	1330	2930

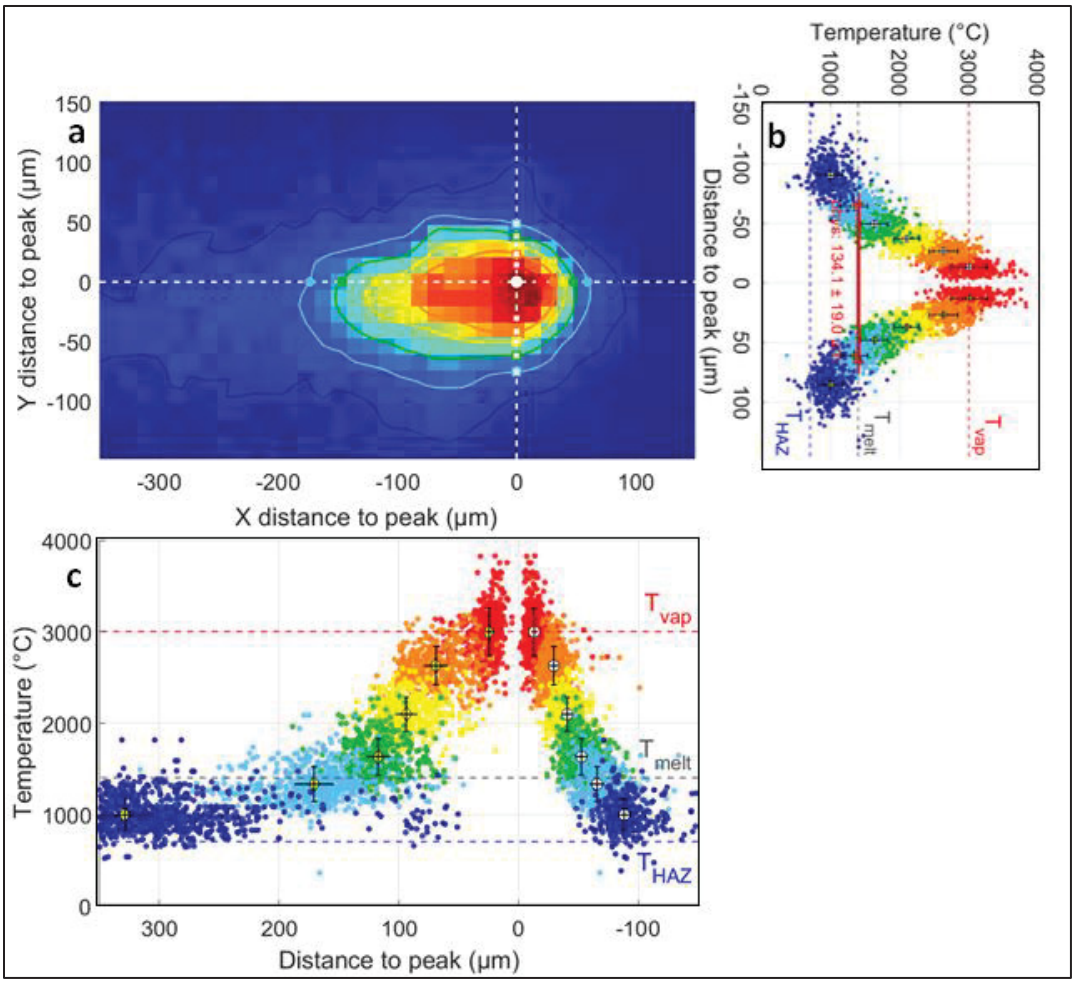

Figure 3.6: Melt pool image (a) with corresponding temperature profile taken across (b) and along (c) the melt pool (316L-P0)

Another way of representing the camera results, which is better suited for comparison with simulations, is to plot 2D regions of interest (ROIs) associated with the vaporization (a), melting (b) and HAZ (c) temperature zones by using distances measured along and across the melt pool zone (width and length) and their corresponding threshold temperatures (Figure 3.7). The shaded areas represent the standard deviation of the measurements across the acquired frames.

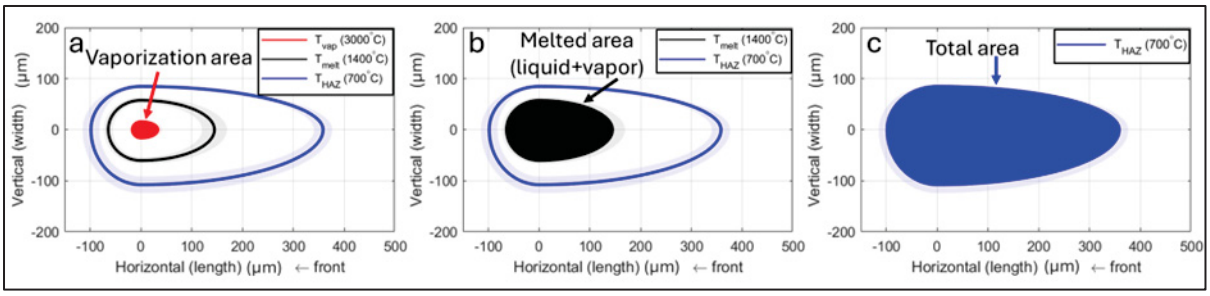

Figure 3.7: Representation of the camera measurements per ROI using the 316 P0 parameter set highlighting the different areas analyzed: a) Vaporization area; b) Melted area that includes the liquid and vaporization areas; c) Total area of a melt pool including HAZ

3.4.2.4 Post-process single-track measurements

After printing, a VHX 7000 Keyence optical microscope (Keyence, Osaka, Japan) having up to a 6000× magnification and a 4K resolution (4000 × 3000 px) was used for imaging and measurement. The single-track measurements (width and depth) were obtained by averaging 8 measurements from the cross-section views (Figure 3.8b). The melt pool characterization was defined using the top view image of the single tracks, enabling to analyze the whole track (Figure 3.8a). This method allows establishing a correlation between in-process thermal observations and post-process metallographic measurements.

Measurements were performed using the image analysis software of the VHX-7000 (v. 3.0.34.332, Keyence, Osaka, Japan) provided with the microscope at 500× and 1000× magnification. The uncertainty reported in Table 3.6 (±5-40 µm) reflects the combined contributions of track-to-track process variability and the complexity associated with the operator-dependent identification of melt pool boundaries.

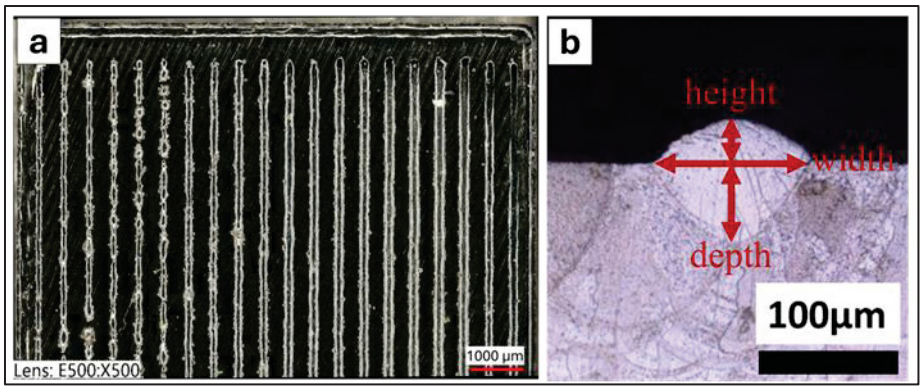

Figure 3.8: (a) Final layer with single tracks and (b) transverse view, highlighting measurements performed

Table 3.6: Single-track widths and depths obtained by metallographic analyses for the three materials studied

	IN625		316L		CoCr	
	Width, µm	**Depth, µm**	**Width, µm**	**Depth, µm**	**Width, µm**	**Depth, µm**
P0	139 ± 22	92 ± 6	134 ± 19	55 ± 9	155 ± 15	114 ± 20
P1	176 ± 17	201 ± 14	154 ± 20	110 ± 6	170 ± 22	146 ± 28
P2	166 ± 21	158 ± 16	140 ± 19	118 ± 7	166 ± 19	147 ± 26
P3	167 ± 31	118 ± 29	142 ± 19	68 ± 7	156 ± 20	64 ± 14
P4	138 ± 14	142 ± 18	129 ± 18	26 ± 6	173 ± 20	97 ± 22
P5	141 ± 15	80 ± 14	136 ± 34	52 ± 5	170 ± 22	131 ± 43
P6	128 ± 24	121 ± 14	129 ± 31	60 ± 4	167 ± 30	107 ± 36
P7	120 ± 33	11 ± 3	118 ± 29	21 ± 14	148 ± 16	57 ± 24
P8	133 ± 28	33 ± 5	124 ± 31	22 ± 8	150 ± 20	70 ± 31
P9	114 ± 27	46 ± 7	119 ± 27	18 ± 9	114 ± 28	34 13

3.5 Results

3.5.1 Single-Tracks Measurements

Single-tracks were classified using two distinct characteristics. The first classification was derived from top view observations, dividing the tracks into continuous or discontinuous (Figure 3.9a). Continuous tracks (Figure 3.9-1a, 2a) were defined as those exhibiting an uninterrupted geometry along their length, whereas discontinuous tracks (Figure 3.9a) presented a lack-of-fusion in certain sections. A second distinction was made using the melt pool depth images (cross-section analyses), which allowed observing three distinct behaviors: regular, lack-of-fusion and keyhole (Figure 3.9b). When the single-track depth was smaller than a one-layer thickness, it was considered to be lack-of-fusion (Figure 3.9-3c); when the single-track depth was 1-2.5 times the layer thickness (Figure 3.9-3a), it was considered regular, and when the single-track depth was >2.5 times the layer thickness (Figure 3.9-3b), it was considered keyhole.

It is noteworthy that all the tracks exhibiting discontinuous geometry along their length also showed a lack-of-fusion in depth. Consequently, keyhole, regular, and lack of fusion single-track categories were retained for the remainder of the study and could be directly correlated with the linear energy density (LED) across all the tested materials (Figure 3.9-4). Specifically, for 316L, a lack-of-fusion behavior was observed when the LED was below 0.20 J/mm, whereas keyhole formation occurred at LED values above 0.31 J/mm, leaving only regular tracks (conduction melting mode) between these two linear energy density levels, regardless of the scan speed considered. Furthermore, the measurements (Table 3.6) highlighted that during a constant scanning speed operation, increasing the LED (P7→P0→P3→P2) consistently resulted in increased single-track widths and depths. Conversely, for a fixed LED, increasing the speed (P4→P0→P5→P6) tended to increase the melt pool depths, but did not affect their widths.

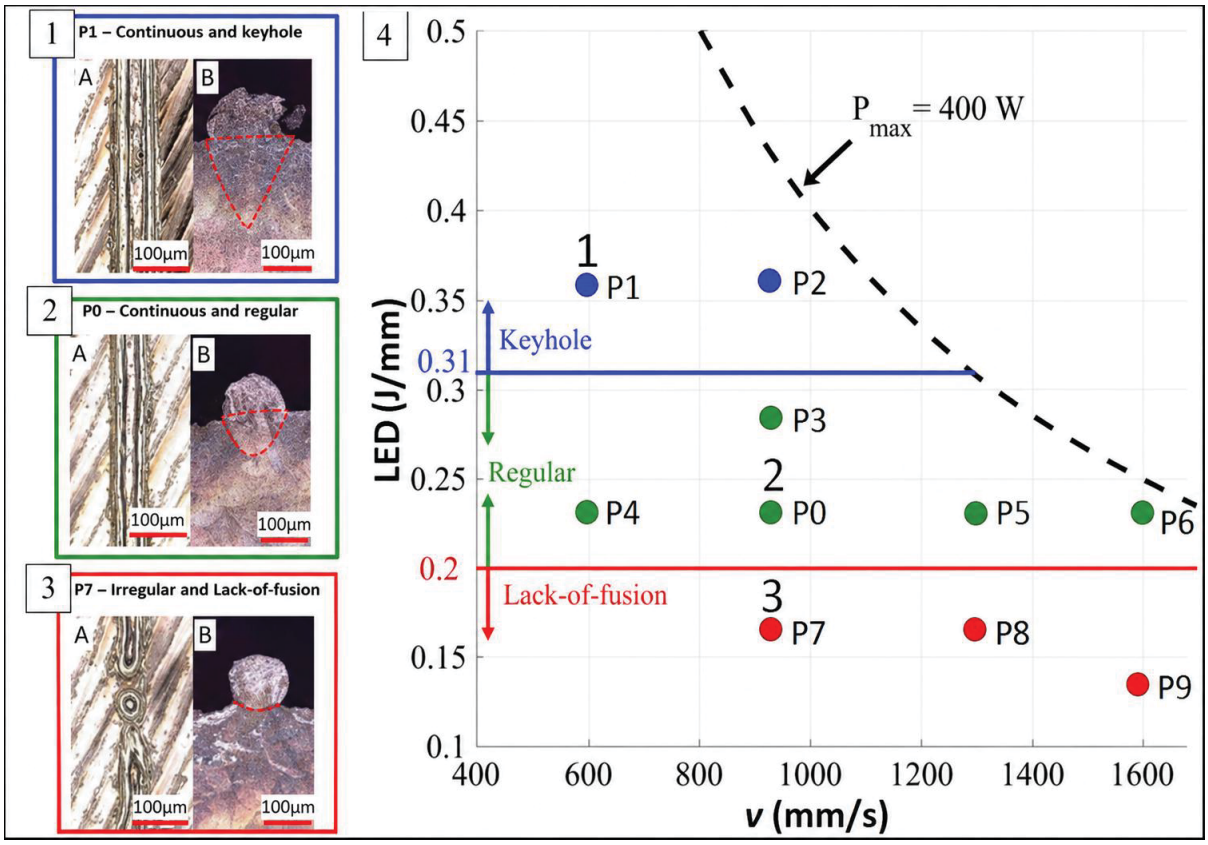

Figure 3.9: Single-track quality classification: (1) continuous and keyhole, (2) continuous and regular (conduction melting) and (3) discontinuous and lack-of-fusion using (A) top layer observations and (B) transverse views, where the red dotted line delimits the melt pool depth boundary; (4) single-track quality of 316L with LED levels associated with different melting regimes

3.5.2 Melt Pool Width And Length (Numerical Simulations Versus Camera Measurements)

3.5.2.1 Temperature Profiles

An initial comparison between simulations and experiments was carried out using melt pool width and length values obtained from the top view temperature fields predicted by numerical simulations and thermal camera observations, using the melting temperature of each material as a threshold. The point clouds corresponding to melt pool widths (Figure 3.10a) and lengths (Figure 3.10b) measured for 316L were compared with their simulated equivalents (black lines

in the graphs). The same procedure was executed for IN625 and CoCr (see corresponding plots in Appendix A Figure AA-1 and AA-2).

As seen from this analysis, the higher the laser power density (P7→P0→P3→P2), the greater the energy input to the powder bed, the higher the maximum temperature reached, and the wider and the longer the melt pools. On the other hand, for a given LED, the higher the scanning speed (P4→P0→P5→P6), the narrower and the longer the melt pools. A clear difference between the experimental and predicted results can be seen in the maximum temperature, more specifically in the keyhole melting mode (high LED values P1-P3). While the thermal camera shows a limit near the material's vaporization point (around 3000 °C), the simulations did not show an upper limit, reaching values of up to ~7000 °C, pointing to the model's limitations in terms of fairly calculating temperature distributions within the evaporation zone and under the keyhole melting mode. However, temperature distributions predicted for the melt pools produced at lower LED and v (P4-P9) can be considered close to their experimentally measured equivalents.

The predicted melt pool dimensions were compared with the thermal camera recordings in Figure 3.11a,b (length and width). Relative errors were first assessed, and linear regression analyses were then performed. A simulation is considered valid when the slope (a_1) is close to 1 and the intercept (a_2) is negligible (equal to 0). The quality of the correlation is reflected by a high adjusted R^2_{adj} (as close as possible to 1) and a low RMSE, indicating good agreement between the model and the experimental data. The simulation results for the length and width, along with the corresponding relative errors, are presented in Tables A1 and A2 in Appendix A for all three materials studied.

When comparing the assessments of melt pools' widths and lengths, the simulated melt pool lengths exhibit better agreement with the experimental data than the simulated melt pool widths. For the length comparison (Figure 3.11b), the global linear regression yields a slope of 1.08 and an adjusted R^2_{adj} of 0.70, indicating a strong positive correlation and consistent scaling between simulated and camera measurements. The corresponding RMSE is 37 μm, reflecting

the larger dimensional range involved in length measurements, corresponding to a difference of 3 pixels. For the width comparison using camera data (Figure 3.11a), the agreement is more moderate, with a slope of 0.94, an adjusted R^2_{adj} of 0.52, and an RMSE of 17.3 μm. Although the linear trend remains evident, the scatter in width measurements is larger than that in length measurements.

To further validate the in situ monitoring approach, simulation measurements are compared with post-process metallography in Figure 3.11c. The resulting regression shows a slope of 1.09 and an adjusted R^2_{adj} of 0.67, with an RMSE of 17.39 μm. The slope slightly above unity suggests a tendency for the simulated measurements to overestimate their metallography-obtained equivalents, with this discrepancy remaining limited. Overall, these results confirm that the simulations provide reliable predictions of the melt pool dimensions, capturing the correct trends while maintaining dimensional errors within an acceptable range.

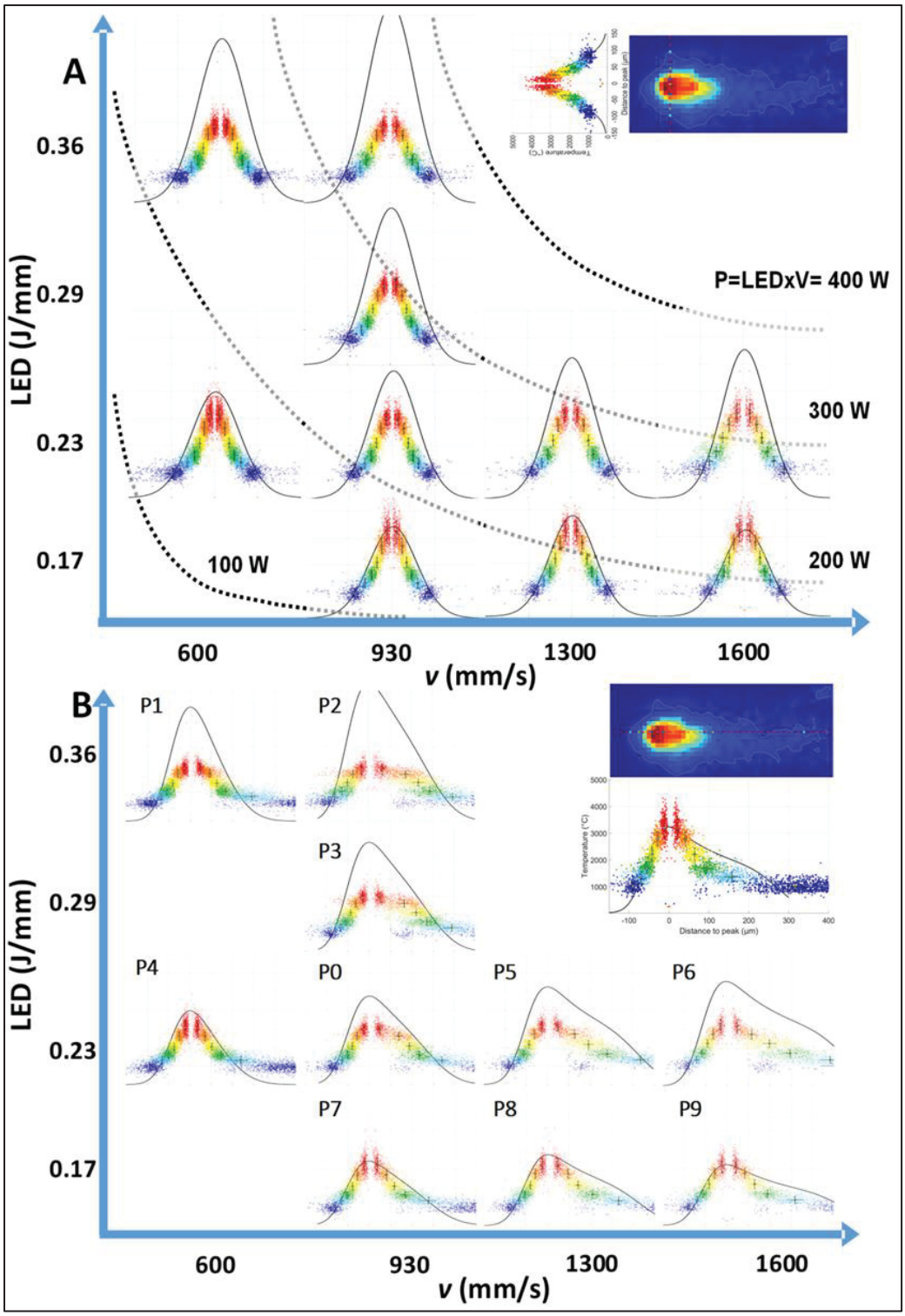

Figure 3.10: 316L melt pool temperature profiles obtained using simulations (black lines) and camera observations (point clouds): A) width, and B) length

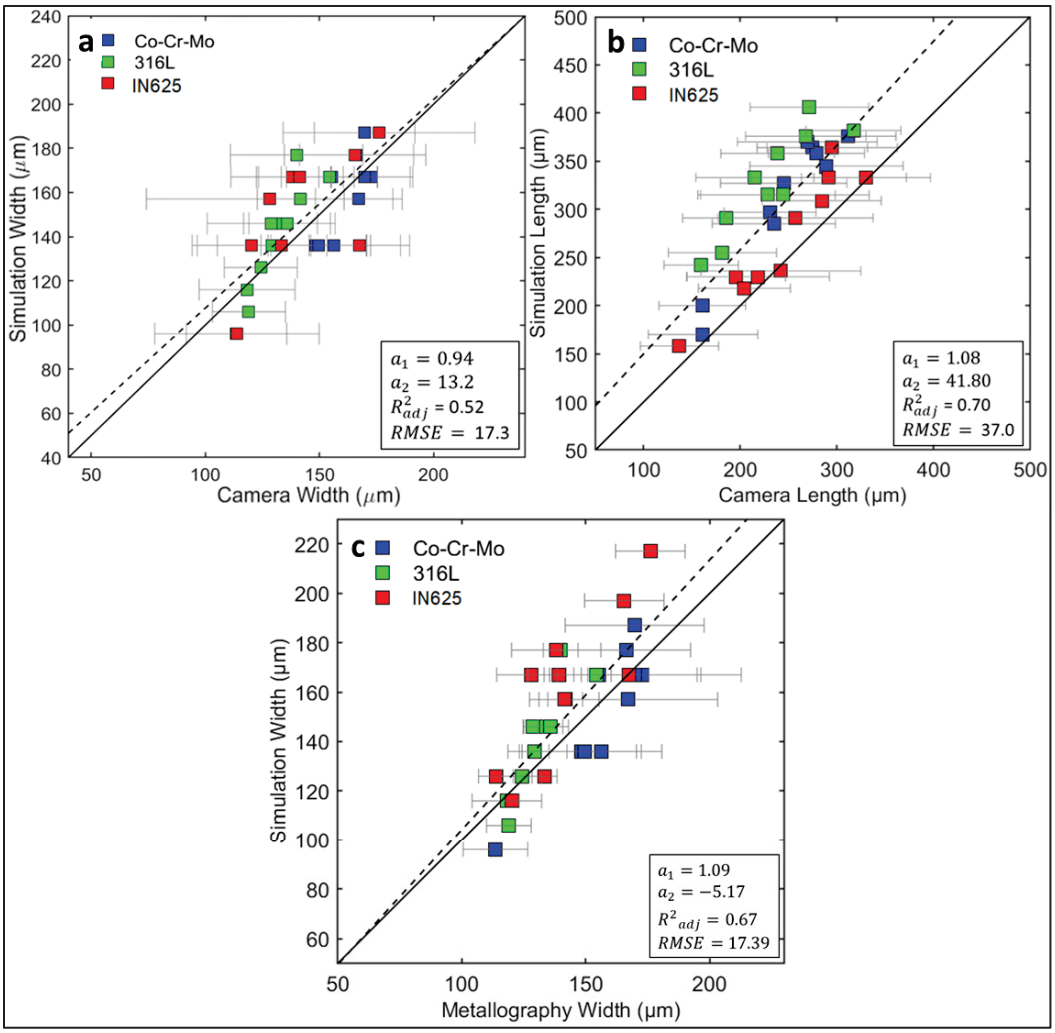

Figure 3.11: Simulated versus camera melt pool measurements: a) width and b) length, for all the materials analyzed; c) width compared between simulation versus metallography results. The solid line represents the perfect agreement (1:1 line), and the dashed line represents the linear regression fit

3.5.2.2 Melt pool area

The 2D thermal camera maps are plotted in the LED - v space in Figure 3.12a for 316L to illustrate how the thermal zones evolve in these coordinates. It can be observed that the melted zone increases with an increase in the LED (P7→P0→P3→P2) and scanning speed (P4→P0→P5→P6). Conversely, no clear trend can be observed in the evolution of the vaporization and HAZ zones with respect to process parameters. The simulated thermal fields

presented in Figure 3.12b show similar trends when compared to their thermal camera equivalents as far as the melting zone is concerned. An increase in both the energy density and scanning speed produces larger melting zones. However, contrary to the thermal camera observations, simulations also reveal HAZ-related trends, with an increased HAZ corresponding to higher energy inputs.

Two main discrepancies between the simulations and the camera observations must be highlighted, the first related to the vaporization zone, and the second, to the HAZ. In both zones, results obtained with the thermal camera cannot be reliably used, for reasons related to the sensor temperature calibration range, which in this study corresponds to 1000 – 3000 °C. Since both the temperature above vaporization and HAZ temperatures fall outside this range, thermal camera measurements in these zones become irrelevant. Nevertheless, the simulated and thermal camera-observed melting zones follow the same trends, and can therefore be compared, even though the camera's melt pools manifest a tear-drop shape, while the simulated melt pools are more ellipse-like. It can be inferred that the ellipse-like shape of the melt pool in simulations is due to a simplified Gaussian beam heat source model.

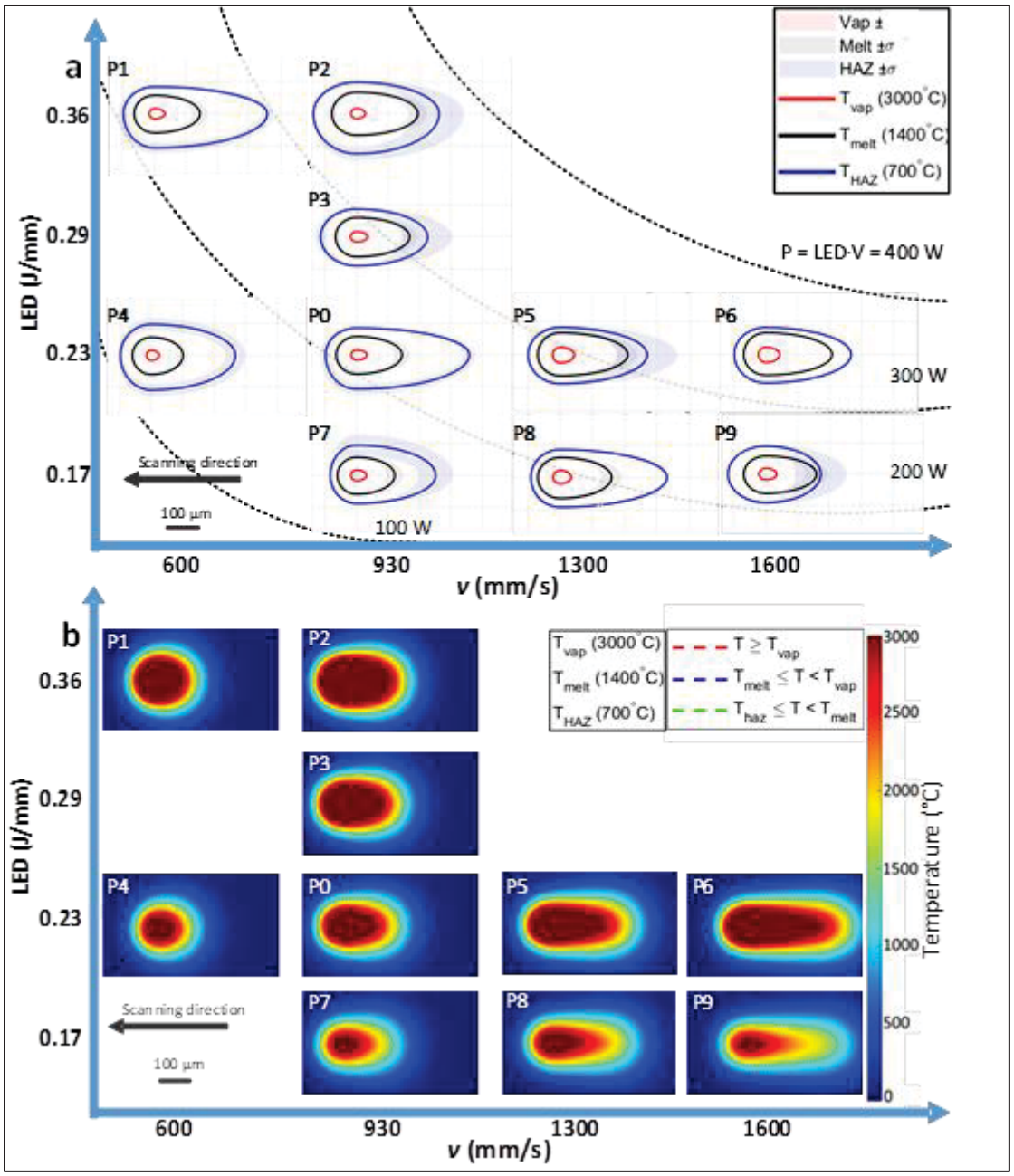

Figure 3.12: a) Averaged 2D thermal maps obtained using thermal camera for 316L; b) simulated thermal maps for 316L, the color scale is limited to 3000 °C

Finally, it can be observed that the higher the laser power, the larger the melt pool areas obtained from simulations (Figure 3.13a) and observations (Figure 3.13b). For 316L, the simulated melted area varies from 0.021 to 0.058 mm^2, while the total area goes up to 0.085 mm^2. The camera results show a similar trend, although with smaller melted areas in the 0.017

to 0.041 mm^2 range. It can therefore be concluded that simulations overestimate the melt pool dimensions as compared to thermal camera observations. These discrepancies hold for all three materials studied and can be explained by two factors: first, the calculated temperature profiles reach unrealistic peaks, greatly exceeding the boiling point of the material (up to 7000 °C), and thus expanding the calculated high-temperature zones. Second, the camera readings are capped by the sensor calibration range, and therefore, by temperatures approaching the material vaporization temperatures, thus reducing the size of the experimentally observed high temperature zones.

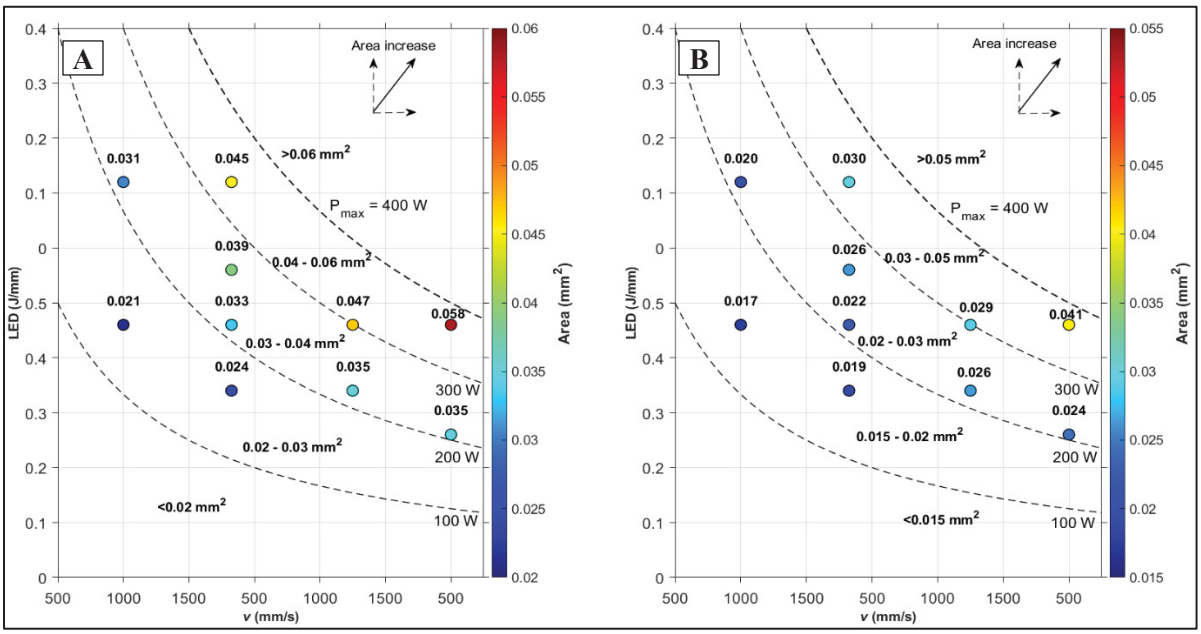

Figure 3.13: Melt pool area for 316L: a) simulations, b) thermal camera observations

When area data for all three materials are grouped together (Figure 3.14), the linear fit yields a_1 = 1.30, with an adjusted R^2_{adj} of ~0.80 and an RMSE of 0.005 mm². This indicates that, overall, the model overestimates the melt pool area by approximately 30% as compared to camera observations, while still preserving a good correlation.

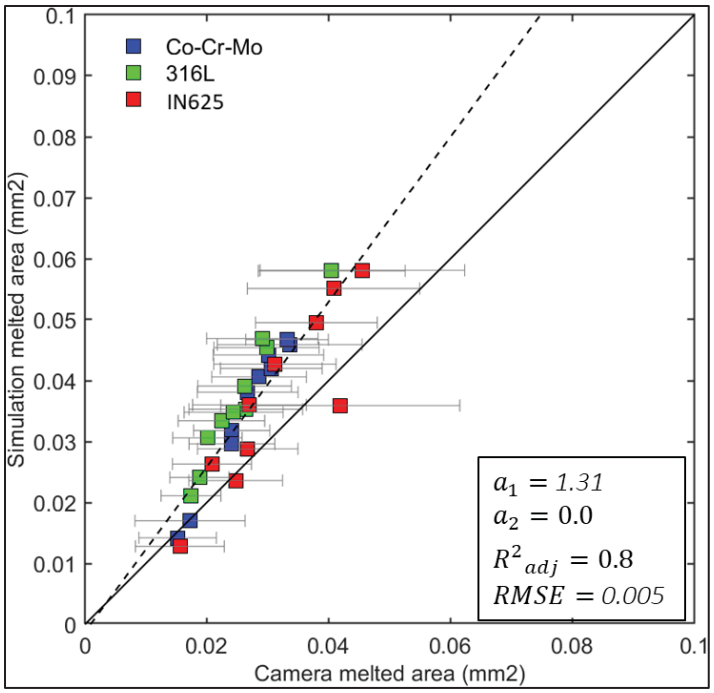

Figure 3.14: Melt pool area: simulations versus camera measurements. The solid line represents the perfect agreement (a_1=1), and the dashed line represents the linear regression fit

3.5.3 Melt Pool Depth (Simulations Versus Metallography)

Comparing the calculated melt pool data with their metallographic equivalents (Figure 3.15) enables to assess the limitations of a heat conduction-based model regarding the melt pool depth calculations. It can be noted that the closest proximity between both sets of data (discrepancy under ±20%) corresponds to the melt pool depth values ranging from 35 to 100 µm (1-2.5 times the layer thickness), i.e., to the occurrence of regular tracks in conduction melting mode. In the keyhole melting region, where the energy input is higher, the greater the melt pool depth, the greater the discrepancy between simulations and experiments, with the discrepancy reaching values as high as 100%. When lack-of-fusion defects occur, the voids (pores) in the solidified substrate act as thermal insulators (heat transfer is much slower than in fully dense solid), a fact not taken into account in the model (this region is named LOF in Figure 3.15). For measured depths between 10 and 35 µm, the model overestimates the

experiments, with a difference of ~30%, while following linear regression with a low dispersion (R^2_{adj} =0.84), which is an excellent fit.

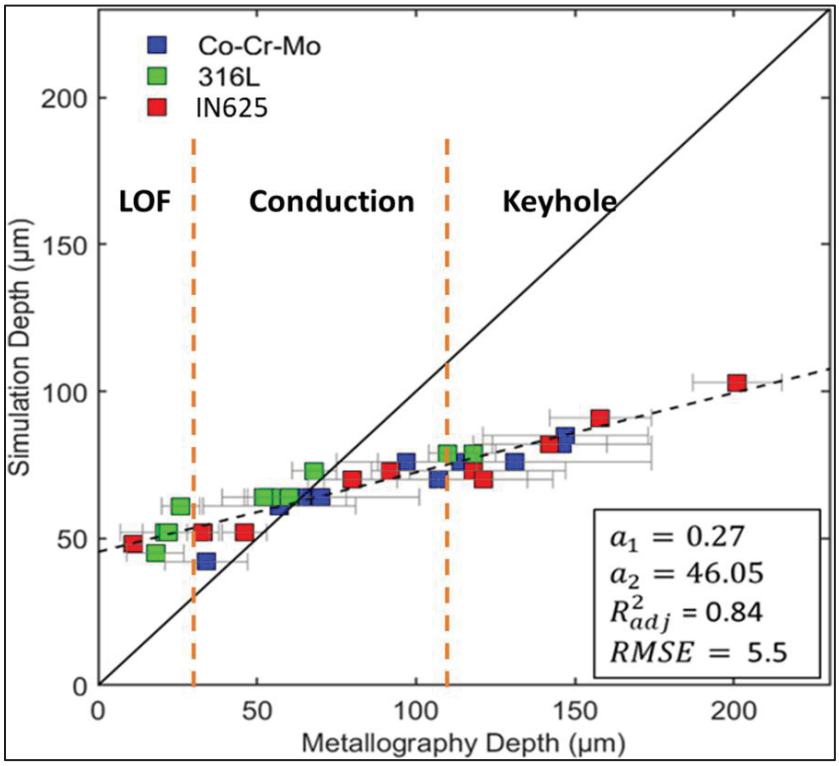

Figure 3.15: Melt pool depth: simulations versus metallography results. The solid line represents the perfect agreement (a_1=1), and the dashed line represents the linear regression fit

3.6 Discussion

The commercial calibration method for a dual-wavelength thermal camera, which consists of resistance-heating a tungsten filament (De Izarra & Gitton, 2010), could not be used in this work. This procedure led to maximum temperature readings exceeding 5000 °C, which is more than 1000 °C above the vaporization point, which is not physically relevant. Furthermore, the background temperature readings were higher than the melting point of the materials analyzed, making it impossible to define the melt pool boundaries. Additionally, the temperatures at the border of melt pools were above 3000 °C, which also did not correspond to the expected temperatures. In contrast, the new calibration method used in the present study brought the

overestimation of the boiling point to only ~100 °C, representing an 80% reduction. This approach also allowed us to directly apply the melting temperature threshold to measure the melt pool dimensions.

Significant differences between the vaporization temperatures and the maximum temperatures obtained with thermal cameras have already been observed in the literature (Hooper, 2018; Myers et al., 2023, 2025), with overestimations varying from ~300 °C to ~500 °C, and being limited by a saturation of sensors. These discrepancies have often been attributed to plume formation or the presence of metal vapor in the optical path between the camera and the melt pool, which interfered with intensity readings. Studies (Hooper, 2018) have also reported difficulties in reaching the melt pool values.

The calibration curve of the present work was obtained by correlating the results of post-process melt pool metallographic analyses with thermal measurements, and the procedure used is explained in more detail in (Soares et al., 2026). Although this type of calibration has not previously been reported for dual-wavelength thermal cameras, a similar approach was adopted for a high-speed infrared camera in (Park et al., 2025). Some equipment producers also suggest applying a constant emissivity across the melt pool, using a single emissivity value calculated at a specific point or region, and generalizing for the whole image. In this study, the pixel-by-pixel ratio was calculated in different regions of the thermal image, thus minimizing the dependence on emissivity. Finally, it should be noted that the calibration developed in this work was performed for a single neutral-density filter configuration. Therefore, the resulting relation between the intensity ratio and the temperature was validated only for this optical setup.

Temperature measurements using dual-wavelength infrared cameras carry significant limitations, the first being the spatial resolution. In the setup used in this work, the pixel size is 13.6 μm in the plane measured, which defines the spatial image resolution. For the melt pool widths in the 100-200 μm range, this means that a one-pixel difference in measurements would correspond to roughly 7-14% melt pool width variations. Consequently, even small

uncertainties in the edge detection or the threshold value can translate into relatively large errors, especially for smaller melt pools (Goossens & Van Hooreweder, 2021). Another limitation of the thermal measurement method developed in this study is the presence of a quite narrow 1000-3000 °C calibration range, also reported in (Mahmoudi et al., 2018). The upper bound prevents an adequate delimitation of the vaporization zone, while the lower bound does not allow adequate definition of the HAZ.

A high-speed CMOS thermal camera has already been used to measure the melt pool width of 316L, with the laser power varied from 100 to 600 W, and the scanning speed, from 400 to 1100 mm/s (Goossens & Van Hooreweder, 2021). In that work, the melt pool contour was determined using a light intensity threshold and a Sobel edge detection filter. The difference between camera and metallographic measurements ranged from −54 to 36% with an average relative error of ~3%. Similar trends were observed in the present work with a ~5% discrepancy for 316L and 7% discrepancy for all three materials. Overall, notwithstanding these limitations, using the thermal camera to validate melt pool measurements and temperature profiles proved to be suitable, especially when it came to comparing values of the melt pool lengths and areas.

The results provided by our simulations can be clustered into two groups, the first being the overall temperature distributions and the peak temperatures, and the other, the proximity of the melt pool width, length, depth and surface area values obtained by simulations to those obtained experimentally.

For the temperature profiles obtained, it was verified that an increase in the LED values also increased the maximum temperature in the melt pool, which was expected, since the energy input also increased. However, it was seen that the maximum simulation temperature was much higher than the vaporization points of the materials, going up to a maximum of 7000 °C, which had also been observed in similar melt pool simulation-related studies (Z. Yang et al., 2024). These discrepancies are related to the models' simplifications, such as neglecting multiple physical phenomena related to the process, including the Marangoni effect, the recoil pressure, the different heat transfer modes and the solid–liquid–vapor phase transformations (De Leon

et al., 2025). These simplifications allowed us to significantly decrease the computational time but at the expense of a reduced model fidelity. For example, when the vaporization effect was considered in (Karayagiz et al., 2019), the maximum temperature calculated in the Ti-6Al-4V alloy's melt pool was reduced by ~50%, going from 6000 to 3050 °C, and the melt pool width measurement error was reduced from ~60 to ~3%, which led to a 30% reduction in discrepancy between the simulated and camera-measured melt pool area values.

The applicability of the present model is therefore reliable in the conduction melting regime, defined here by the linear energy density ranges $0.20 < LED < 0.31$ J/mm for 316L, $0.21 < LED < 0.39$ J/mm for IN625, and $0.21 < LED < 0.37$ J/mm for CoCr. Within this window, melt pool surface dimensions (width, length, and area) and peak temperatures, in some cases, can be predicted with confidence. In either the keyhole regime or the lack-of-fusion regime, the model proved to be a useful tool for trend analysis rather than for exact predictions. Accurate prediction of melt pool depth and peak temperature in these regimes would require the inclusion of recoil pressure, liquid and vapor dynamics, which are beyond the scope of the simplified formulation used here.

The simulations systematically overestimate the melt pool area by ~30%, which can be attributed to two contributions of comparable magnitude. First, the analytical model of this study disregards the liquid and vapor dynamics involved in melt pool formation, including energy losses from the melt pool surface due to evaporation and the downward recoil pressure that redistributes heat into the depth direction. In this context, Karayagiz et al. (2019) demonstrated that the explicit accounting for vaporization in LPBF Ti-6Al-4V reduces the peak temperatures by ~50% and decreases the melt pool width calculation errors from ~60% to ~3%, suggesting that vaporization is responsible for most of the surface-area overestimation. Second, the thermal camera's upper calibration limit at 3400 °C restricts the measurable temperature range. Above this threshold, the temperature mapping becomes unreliable, preventing accurate quantification of the vaporization zone. However, the rest of the temperature field, including the melting isotherm used for melt pool boundary extraction, remains within the calibrated range and is therefore unaffected. A more rigorous treatment of

both effects would require either extending the camera calibration validity above 3400 °C or incorporating a vaporization-limited temperature cap in the simulation framework. Both approaches are recommended for future work.

The morphological validation we performed showed that the strongest correlation between the model and experimental measurements was achieved for the total melted area, with R^2_{adj} values ranging from 0.8 to 0.93. Among the alloys studied, CoCr exhibited the best predictive performance in general for all the melt pool geometrical metrics considered. This behavior is likely associated with the fact that, under the investigated process conditions, CoCr tends to operate closer to a conduction-dominated regime, where heat transport is mainly governed by diffusion and assumptions of the simplified thermal model remain closer to reality than for the two other metallic alloys, i.e., 316L and IN625 (W. Wang et al., 2022).

At the same time, the linear regression coefficient (a1) ranged mostly between 1.0 and 1.5 and the $a_2 > 0$, meaning that there was a 30% systematic overestimation for all the materials. These results align with the findings in (Mao et al., 2024), which also revealed a significant overestimation of the simulation data as compared to experiments, especially at higher laser powers, where the model did not consider variations in the laser absorption values.

Regarding the melt pool length, the model showed the highest predictive performance, with an R^2_{adj} of 0.97 for CoCr. The simplified model also properly represented the effects of printing parameters, especially the scanning speed, on the melt pool tail. Between the three dimensions measured (width, length and depth), the length was shown to be the least sensitive to approximations of the simulation model of this study.

In contrast, the melt pool width exhibited a higher sensitivity and greater dispersion, with a1a1 varying from 0.85 to 1.7. This increased variability can be associated with the fact that alloys such as IN625 and 316L are more susceptible to transition toward fluid-driven regimes, where melt pool convection and recoil pressure effects become more relevant, reducing the predictive accuracy of thermal conduction-based models (W. Wang et al., 2022). However, the same

trend as above was also respected, with the width increasing with an increase in the laser energy density, as was also observed by other authors (Liu et al., 2025; Y. Yang et al., 2022).

Furthermore, 316L presents a combination of a relatively high melting temperature, elevated absorptivity, and moderate thermal conductivity that makes its melt pool more sensitive to convective flow and stochastic variations. As a result, localized keyhole formation may occur at higher laser energy densities, producing narrow and deeper melt pools and reducing peak temperatures as compared to model predictions (W. Wang et al., 2022; Zhang et al., 2024).

These observations naturally demonstrate that conduction-only models are more reliable for alloys and conditions in which heat transport remains predominantly in conductive mode and melt pool dynamics are moderate. In alloys like 316L at higher laser energy densities, where convective transport and localized keyhole effects become more significant, deviations from conduction-based predictions are expected (Cox et al., 2022). This notwithstanding, simplified thermal-conduction models remain a valuable tool for rapid first-order simulations and process parameter exploration.

Despite a relatively good correlation between melt pool surface measurements (width, length and area), the predicted melt pool depth presented significant agreement with the metallographic results only within the conduction melting mode. As shown in Figure 15, a linear regression coefficient of ~0.3 confirms that a thermal conduction-based model is clearly unsuitable for melt pool depth prediction in the case of large pores in a solidified substrate and keyhole melting, since the model does not consider the reduced effective conductivity in porous regions. The same was also reported in (Guo et al., 2022; Holla et al., 2024), where a simplified simulation model predicted the width correctly, but underestimated the depth outside the stable conduction melting mode. Regarding the high energy inputs ($LED > 0.3$ J/mm), any simulations that neglect the vapor and recoil pressure phenomena, which are responsible for a higher downward heat transport (Huang et al., 2022; Zhao et al., 2020), underestimate the melt pool depths. Conversely, for irregular tracks with low energy inputs ($LED < 0.2$ J/mm), simulations overestimate the melt pool depth, since the model assumes

continuous melting and does not consider cooling and incomplete powder sintering (Huang et al., 2022).

Despite a relatively good correlation between melt pool surface measurements (width, length and area), the predicted melt pool depth presented significant agreement with the metallographic results while restricted to the conduction melting mode. As shown in Figure 3.15, a linear regression coefficient of ~0.3 confirms that a thermal conduction-based model is clearly unsuitable for melt pool depth prediction in the case of large pores in a solidified substrate and keyhole melting, since the model does not consider the reduced effective conductivity in porous regions. The same was also reported in (Guo et al., 2022; Holla et al., 2024), where a simplified simulation model predicted the width correctly, but underestimated the depth outside the stable conduction melting mode. Regarding the high energy inputs (LED > 0.3 J/mm), any simulations that neglect the vapor and recoil pressure phenomena, which are responsible for a higher downward heat transport (Huang et al., 2022; Zhao et al., 2020), underestimate the melt pool depths. Conversely, for irregular tracks with low energy inputs (LED < 0.2 J/mm), simulations overestimate the melt pool depth, since the model assumes continuous melting and does not consider cooling and incomplete powder sintering (Huang et al., 2022).

Given the strong linearity observed ($R^2_{adj} \geq 0.86$) and the regression slope of approximately 0.3 in the keyhole regime, an empirical correction can be implemented by multiplying the simulated depth slope by a compensation factor of kd ≈ 1/0.3 ≈ 3.3 (based on Table 3.7). This correction would enable the conduction-based model to serve as a rapid predictive tool across the entire process window, including the keyhole regime, albeit with reduced physical fidelity. For physically reliable predictions in the keyhole predictions, the model should be extended to incorporate the previously discussed physical phenomena, including recoil pressure, liquid Marangoni convection, and vapor dynamics. Further validation of this compensation strategy across additional materials and process conditions is recommended for future work.

Table 3.7: Results of linear regression analyses between the experiments and simulations of the melt pool length, width, depth, and the melted area for all three materials

	IN625				316L				CoCr			
	a_1	a_2	R^2_{adj}	RMSE	a_1	a_2	R^2_{adj}	RMSE	a_1	a_2	R^2_{adj}	RMSE
Length	1.1	7.6	0.88	20	1.0	90	0.78	22	1.4	27	0.97	18
Width	0.85	34	0.43	19	1.7	-90	0.76	9.63	1.4	-63	0.80	11
Depth	0.29	42	0.94	4	0.3	47	0.86	3.8	0.3	41	0.86	4
Melted Area	1.2	0.0	0.8	0.01	1.5	0.0	0.93	0.003	1.4	0.0	0.9	0.003

3.7 Conclusion

The present study performed a reliability assessment of the simplified Gaussian heat source thermal conductivity-based melt pool LPBF model for 316L, IN625, and CoCr alloys using a combination of the in-process thermal camera and post-process single-track measurements; the main results demonstrated the following:

- The model accurately predicted the melt pool geometry features (width, length, and melted area) across a wide range of process parameters corresponding to the conduction melting mode. The melt pool length showed the highest agreement with the thermal camera measurements ($R^2_{adj} > 0.78$). The prediction of a melt pool width showed a more moderate agreement due to its inherent sensitivity to the Marangoni effect; however, the overall trends remained compatible with experimental observations and confirmed that thermal conduction-based models are highly effective for predicting the melt pool surface geometry in the conduction melting regime.

- Quantitative prediction of the melt pool depth was found to be limited outside the conduction melting regime, with a regression slope of approximately 0.3 observed. This underestimation in the high-energy regimes and overestimation in the lack-of-fusion zones reflect the main limitations of the model in terms of its capacity to simulate the keyhole dynamics and consider the recoil pressure. Nevertheless, a high degree of linearity was

observed across all the materials, confirming that these discrepancies are systematic rather than random, which supports the model's suitability for preliminary trend analysis.

- Outside the conduction melting mode, the model should primarily be used for trend analysis rather than absolute predictions, since it does not account for the physical mechanisms governing the keyhole and lack-of-fusion regimes.

- Dual-wavelength thermal camera measurements proved to be highly effective for validating the melt pool geometry simulations. Comparisons between the metallography and temperature measurements showed a discrepancy of only 6–9%, thus demonstrating the camera's performance as a process monitoring tool.

In summary, this work establishes a comprehensive methodology for the reliability assessment of LPBF thermal conductivity-based melt pool models. By utilizing simplified melt pool simulations validated in the present work, the computational and experimental costs associated with mapping the process windows for high-performance metallic alloys in LPBF can be significantly reduced.

3.8 Acknowledgments

The authors acknowledge the financial support provided by NSERC (Natural Sciences and Engineering Research Council of Canada) under the Discovery Grant program. The authors also acknowledge the contributions of Emma Bisserié in sample preparation and analysis. During the preparation of this study, the authors used ChatGPT, gpt-4.0, for the purposes of debugging code and translating texts. The authors have reviewed and edited the output and take full responsibility for the content of this publication.

3.9 Funding

This research was funded by the Natural Sciences and Engineering Research Council of Canada (NSERC) under Discovery Grants RGPIN-2020-05800 (V. Brailovski) and RGPIN-2025-04142 (A. Kreitcberg).

3.10 Authors Contribution

M.D.A.S.—performed the experiments, developed the image analysis code, carried out data analysis, prepared figures, and wrote the main manuscript; D.C.—participated in experimental work, con-tributed to code development, and reviewed the manuscript; A.L.—performed numerical simulations and contributed to manuscript writing; A.K.—supervised the work and reviewed the manuscript; V.B.—conceived the study, supervised the project, and reviewed the manuscript. All authors have read and agreed to the published version of the manuscript.

3.11 Competing Interests

The authors declare no competing interests.

3.12 Data Availability

The datasets generated and analyzed during the current study, including experimental measurements and processed data, are available from the corresponding author upon reasonable request. Representative 3D models associated with this study are also available upon request.

The code used for thermal image acquisition is not publicly available due to the inclusion of proprietary components but may be partially shared upon reasonable request, subject to restriction

CHAPTER 4

VALIDATION OF THE IN-PROCESS CALIBRATION METHOD USING Ti-6Al-4V

4.1 Context and Motivation

The calibration method developed in Chapter 2 was built using five materials — 316L, IN625, CoCr, W, and Mo, whose liquidus temperatures served as calibration points spanning a range of approximately 1300 to 3422 °C. Although the method produced physically consistent temperature maps for all five materials, a calibration built exclusively from the data used to construct it cannot, by definition, demonstrate that it can be generalized to other materials. To address this limitation, independent validation was performed using Ti-6Al-4V, a material that was not part of the original calibration experiment. Ti-6Al-4V was selected for this validation because it is a widely used alloy in LPBF, its thermophysical properties are well characterized, and its liquidus temperature (approximately 1650 °C) falls within the calibrated range, allowing a direct comparison with the calibration curve.

4.2 Material Properties and Experimental Setup

The melting point of Ti-6Al-4V is defined as 1660 °C. Single-track experiments were conducted following the same protocol used for the five calibration materials in Chapter 2. A parameter matrix covering conduction, keyhole, and lack-of-fusion melting regimes was selected by varying laser power from 50 to 360 W and scanning speed from 500 to 1200 mm/s, as shown in Figure 4.1A. The top view of the printed tracks (Figure 4.1B) highlights the morphological difference between parameters producing stable, continuous tracks in the conduction regime and those that generated balling in the low-energy-input conditions (parameters P8 and P9).

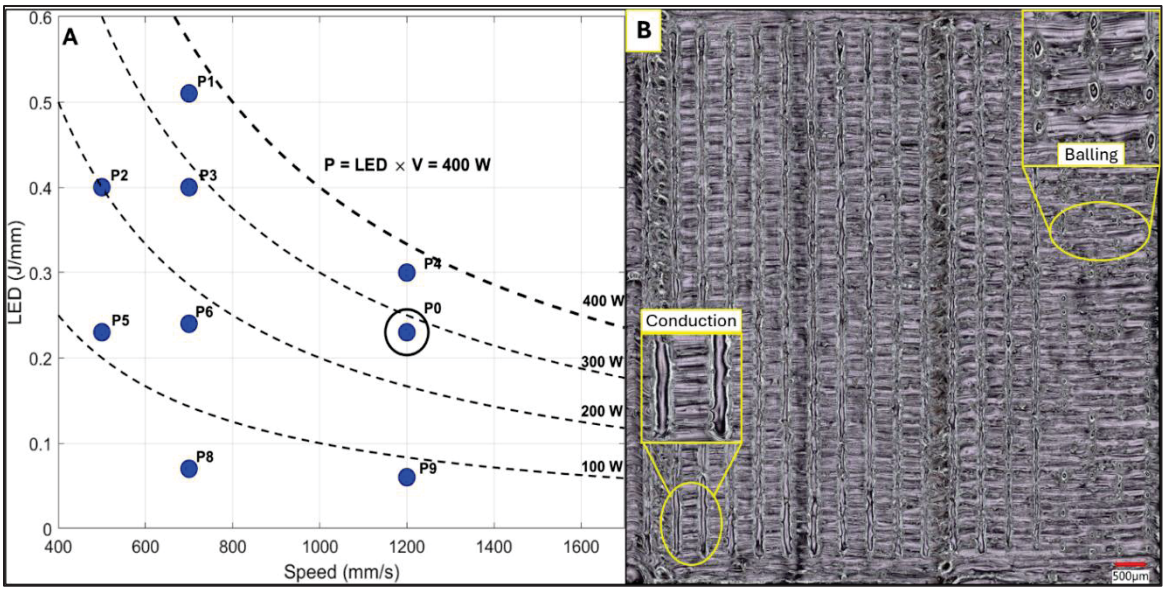

Figure 4.1: Ti-6Al-4V single-track parameter matrix: A) linear energy density vs. scanning speed map with process regime classification; B) top-view images of single tracks showing stable conduction-mode tracks in parameters P0 and P1 and balling in parameters P8 and P9

4.3 Calibration Curve Validation

To validate the calibration independently, the intensity ratio measured by the thermal camera at the melt pool boundary of Ti-6Al-4V single tracks was extracted using the same metallographic width cross-referencing procedure. This procedure consisted in taking the intensity contour at which the thermally measured width matches the metallographically measured width as the liquidus point of the material. The resulting intensity ratio-temperature value was then compared against the calibration curve constructed. The deviation between the Ti-6Al-4V data point and the curve was approximately 87 °C, corresponding to a relative difference of 6% with respect to the liquidus temperature of the alloy. This agreement, obtained from a material that was not used to construct the calibration, confirms that the curve generalizes beyond the original dataset and provides a physically consistent temperature estimate for alloys within the calibrated melting point range.

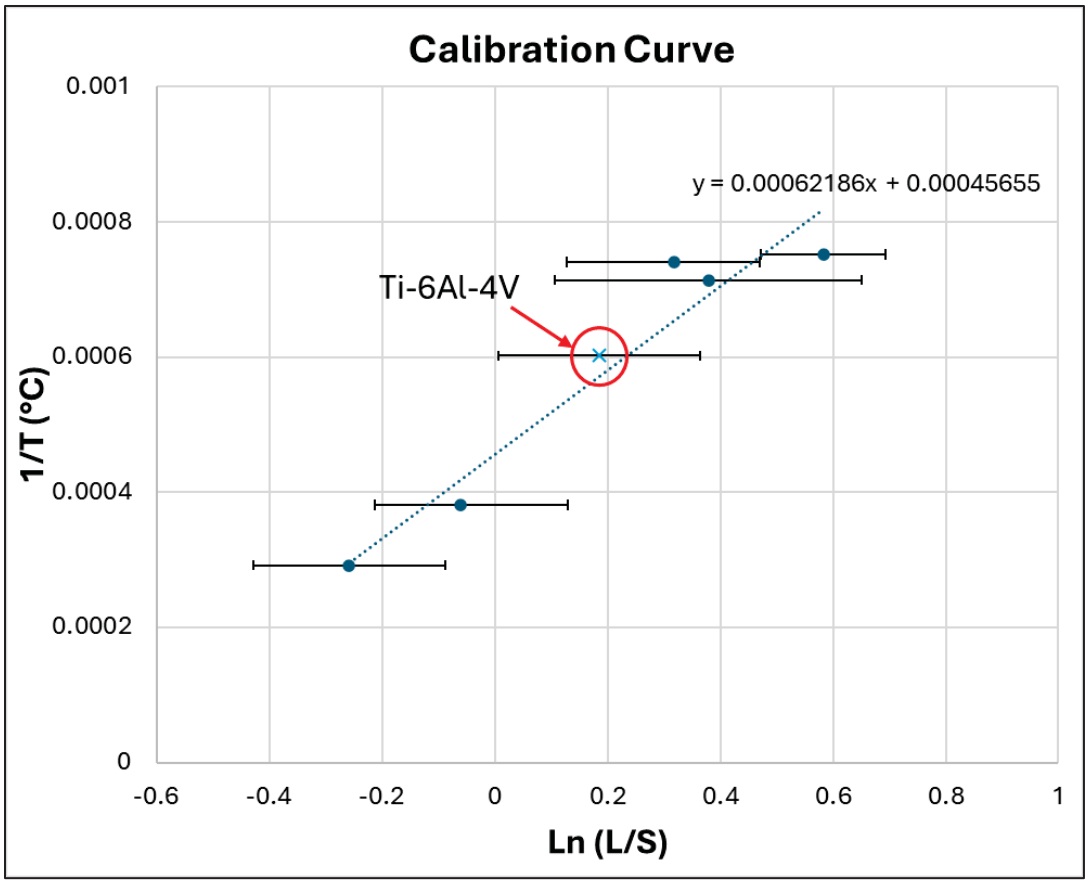

Figure 4.2: Ti-6Al-4V melting point comparison on the calibration curve

4.4 Melt Pool Width Measurement

In addition to the calibration curve comparison, melt pool widths were measured from the Ti-6Al-4V thermal images using the liquidus isotherm as a contour threshold, and compared against the metallographic width measurements obtained from cross-sections of the same tracks. As shown in Figure 4.2, for parameters producing stable, continuous single tracks in the conduction regime, the agreement between the two measurement methods is within 12% (21.5 µm), consistent with the discrepancies observed for the five calibration materials in Chapter 2. This agreement inverts for the balling parameters (P8 and P9), where the track is discontinuous and the metallographic width measurement becomes unreliable or impossible at many cross-sections, generating a difference of up to -21% (22.6 µm). Notably, for these balling conditions, the thermal camera provides a more consistent width estimate than the

metallographic approach, since the camera observes the melt pool surface continuously during printing regardless of track morphology, while the post-process cross-section can only be measured where a coherent track exists. This suggests that in the balling regime, the optical width from the camera may in fact be the more reliable of the two measurements. However, the biggest difference was seen on the P1, the parameter with the highest energy input, with a difference close to 30% (or 60 µm).

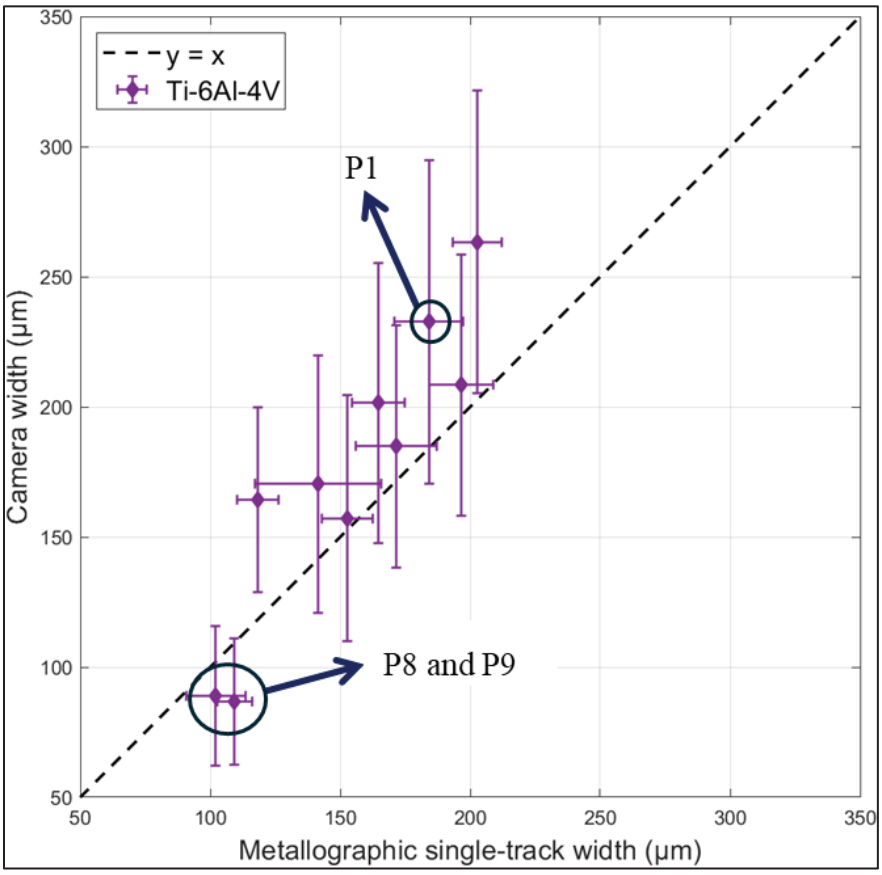

Figure 4.3: Comparison of melt pool width measurements from ex-situ metallography and thermal camera for Ti-6Al-4V single tracks across all parameter sets. Balling parameters (P8, P9) are indicated

4.5 Summary

The Ti-6Al-4V validation confirms that the in-process calibration method developed in Chapter 2 generalizes to materials not used in its construction, with a calibration curve

deviation of approximately 87 °C for a material whose liquidus temperature falls within the calibrated range. Melt pool width measurements from the thermal camera are consistent with metallographic measurements to within 15% for stable conduction-mode tracks, and the camera outperforms metallography as a width measurement tool in the balling regime, where track discontinuity renders top view measurement unreliable. Together, these results support the use of the calibrated dual-wavelength thermal camera as a material independent (material-agnostic) tool for quantitative melt pool characterization in LPBF.

CONCLUSION

This thesis developed and validated an experimental methodology for quantitative in-situ melt pool monitoring in LPBF using a dual-wavelength thermal camera calibrated through ex-situ single-track metallography. A persistent challenge in LPBF process monitoring is the difficulty of obtaining reliable measurements from in-situ thermal cameras: commercial tungsten filament calibrations produce physically inconsistent temperature readings, and no single monitoring technique provides access to all melt pool dimensions simultaneously. In particular, the melt pool length, an important parameter for validating thermal simulations, can only be measured in-situ from the thermal image, since metallographic cross-sections provide only the melt pool width and depth. The methodology proposed in this work addresses these limitations by combining two complementary measurement techniques, in-situ thermal camera (width, length, temperature) and ex-situ metallography (width, depth), that share a common melt pool width measurement enabling cross-validation between the two approaches. The main contributions, limitations, and directions for future research are summarized below.

In-Process Calibration of the Dual-Wavelength Thermal Camera

The commercial tungsten filament calibration of the camera was shown to systematically overestimate melt pool contour temperatures by approximately 450 °C for medium range melting temperature alloys (316L, IN625, CoCr), producing temperature readings that prevent reliable melt pool boundary extraction from the thermal images. A novel in-process calibration method was proposed, in which the liquidus temperature of the material being processed serves as a fixed physical reference point, identified by cross-referencing the thermal image intensity contour with metallographically measured single-track widths. Applied to five materials (316L, IN625, CoCr, W, Mo), the method produced the following key results:

– A single calibration curve covering a melting temperature range of approximately 1300 to 3422 °C was established using the five materials, demonstrating that the method is applicable across the full range of alloys and refractory metals commonly processed by LPBF.

– The new calibration reduced the peak temperature overestimation at the melt pool center from more than 1500 °C to approximately 100 °C for the medium melting temperature range alloys, bringing the camera readings into physical consistency with the known thermophysical properties of the materials.

– The liquidus isotherm could be used directly as a contour threshold for melt pool boundary extraction, enabling quantitative width and length measurements from the thermal images, a capability that was not possible with the commercial calibration.

– Cross-validation between the two experimental techniques, thermal camera (width from liquidus contour) and metallography (width from cross-section), revealed average differences of 6–9% across all three materials, with discrepancies up to 30%. This agreement, obtained from two independent measurement approaches that do not rely on any assumptions, confirms the consistency of the combined methodology and the reliability of the calibrated camera as a quantitative dimensional measurement tool.

– An independent validation using Ti-6Al-4V, a material not included in the calibration dataset, confirmed that the calibration curve generalizes to other alloys within the calibrated temperature range, with a deviation of less than 90 °C, or 6%, from the expected liquidus point.

Reliability of the Analytical Melt Pool Model

The reliability of the simplified Gaussian moving heat source analytical model was assessed by comparing its predictions of melt pool temperature, width, length, depth, and area against simultaneous in-situ thermal observations and ex-situ metallographic measurements for 316L, IN625, and CoCr across ten parameter sets per material spanning the LOF, conduction, and keyhole melting regimes. The following conclusions were observed:

— The model reliably predicts the process trends of melt pool width, length, and area in the conduction melting regime. Melt pool length showed the strongest agreement with camera measurements ($R^2_{adj} > 0.70$), while melt pool width showed moderate but consistent correlation ($R^2_{adj} > 0.52$). CoCr achieved the best overall predictive performance ($R^2_{adj} = 0.97$ for length), operating predominantly in the conduction regime under the investigated conditions.

— For melt pool depth, the model systematically underestimates their values in the keyhole regime due to the non-consideration of recoil pressure and vapor dynamics — the physical mechanisms responsible for the additional penetration of the laser in keyhole mode. However, high linearity of the correlation ($R^2_{adj} \geq 0.86$) confirms that the deviations are systematic rather than random, indicating that a simple empirical scaling factor could partially correct the model in this regime.

— The dual-wavelength camera calibrated via the material's liquidus temperature provides emissivity-independent melt pool temperature, width and length measurements. This enables a complete three-dimensional melt pool dataset (width and length from the camera, width and depth from metallography) with built-in cross-validation on the shared width.

Limitations

The following limitations of the present work should be acknowledged when interpreting the results and planning future studies:

— The calibration method requires ex-situ metallographic measurements as input, which are time-consuming and introduce an uncertainty of approximately ±5–20 µm in the width measurement that propagates into the calibration. The method is therefore not fully in-situ and cannot be applied without a parallel metallographic experiment.

— The gray-body assumption underlying ratio pyrometry, which states that emissivity at the two camera wavelengths (725 and 900 nm) is identical, represents a simplification that may not hold for all materials or all surface states encountered during LPBF. In practice, this

introduces a systematic error in the temperature maps that cannot be separated from the calibration error without independent emissivity measurements.

— The calibration temperature range excludes low melting point alloys such as aluminum or copper and at the upper end temperatures above the tungsten melting point are extrapolated beyond the calibrated range, not capturing all the details close to vaporization temperature for many materials. Similarly, the heat-affected zone surrounding the melt pool, where temperatures fall below the lowest calibration point, cannot be measured with the same level of confidence.

— The analytical model is a conduction-only formulation that neglects Marangoni convection, recoil pressure, and evaporation. Its reliability is therefore limited to the conduction melting regime, and it cannot reproduce the melt pool morphology in the keyhole regime without empirical corrections. The depth prediction, in particular, should not be used for the keyhole-regime parameter selection without such corrections.

— The camera spatial resolution of 13.6 μm/pixel limits the accuracy of width and length measurements for the smallest melt pools in the study (low-power, high-speed conditions), where the melt pool width approaches 50–70 μm and is captured within only 4–5 pixels.

Overall, this work demonstrates that a dual-wavelength thermal camera can be properly calibrated using the physical melting points of the materials being processed, serving as a reliable, quantitative, and material independent tool for in-situ melt pool characterization in LPBF. Combined with ex-situ single-track metallography and the analytical simulation model, it constitutes a comprehensive methodology for process characterization and model validation that is practical to implement on any LPBF system equipped with a thermal imaging capability.

RECOMMENDATIONS

The results of the thesis open several options for further research, both in the refinement of the tools developed and in their application to broader process and material development problems. Possible future use and works are:

— Closed-loop melt pool control. The calibrated camera is capable of extracting quantitative melt pool dimensions in real time using the temperature map. This capability can be used as the feedback signal in a closed-loop control system, where geometrical deviations from the melt pool leads to real-time adjustments of laser power or scanning speed.

— Extension of the calibration to additional materials and camera configuration**.** The current calibration covers six materials. Extending the dataset to other industrially relevant alloys, including copper alloys, aluminum alloys, and additional titanium alloys, would expand the applicability of the calibration curve and test its robustness across materials with very different emissivity characteristics. Also using different neutral density filters could be used to broaden and validate the calibration to different optic setups

— Model improvement for the keyhole regime. The systematic depth underestimation of the analytical model in the keyhole regime could be corrected by incorporating an empirical keyhole depth correction factor calibrated against the metallographic measurements collected in this thesis. Additionally, a correction based on the recoil pressure balance at the keyhole tip could be implemented without the full computational cost of a high-fidelity physics-based simulation.

— Integration with machine learning for defect prediction and microstructure-sensitive process optimization. The thermal camera data collected in this study could serve as training data for machine learning models that predict defect formation, or physical effects like vaporization, from melt pool geometry and temperature distributions. Furthermore, the spatially resolved temperature field enables the calculation of thermal gradients and cooling

rates, which directly influence the microstructure and the level of residual stresses in the printed material. The combination of a physically consistent temperature field with spatial melt pool geometry represents a promising direction for data-driven in-situ LPBF quality assurance.

APPENDIX A
Supplementary data for Chapter 3

Table AA.1: Simulated widths and associated relative errors according to metallographic observations

	IN625			316L			CoCr		
	Exp. (µm)	**Model (µm)**	**Error (%)**	**Exp. (µm)**	**Model (µm)**	**Error (%)**	**Exp. (µm)**	**Model (µm)**	**Error (%)**
P0	139±22	167	-20	134±19	146	-9	155±15	167	-7
P1	176±17	217	-23	154±20	167	-8	170±22	187	-10
P2	166±21	197	-19	140±19	177	-26	166±19	177	-6
P3	167±31	167	0	142±19	157	-11	156±20	136	13
P4	138±14	177	-28	129±18	136	-5	173±20	167	3
P5	141±15	157	-11	136±34	146	-8	170±22	167	2
P6	128±24	167	-30	129±31	146	-13	167±30	157	6
P7	120±33	116	3	118±29	116	2	148±16	136	8
P8	133±28	126	6	124±31	126	-1	150±20	136	9
P9	114±27	126	-11	119±27	106	11	114±28	96	16

Table AA.2: Simulated lengths and associated relative errors according to camera observations

	IN625			316L			CoCr		
	Camera (µm)	**Model (µm)**	**Error (%)**	**Camera (µm)**	**Model (µm)**	**Error (%)**	**Camera (µm)**	**Model (µm)**	**Error (%)**
P0	305±44	309	-1	326±51	333	-2	347±51	364	-5
P1	328±60	333	-2	315±58	291	8	318±49	327	-3
P2	286±43	291	-2	386±56	376	3	346±55	345	0
P3	236±32	230	3	361±54	358	1	179±38	170	5

	IN625			316L			CoCr		
	Camera (µm)	**Model (µm)**	**Error (%)**	**Camera (µm)**	**Model (µm)**	**Error (%)**	**Camera (µm)**	**Model (µm)**	**Error (%)**
P4	343±65	364	-6	252±57	242	4	307±41	297	3
P5	229±31	230	-1	380±43	406	-6	382±52	376	2
P6	329±100	333	-1	388±47	382	2	345±49	358	-4
P7	162±36	158	2	260±55	255	2	270±47	285	-5
P8	205±65	218	-6	323±53	315	3	340±54	370	-8
P9	238±76	236	1	309±63	315	-2	194±33	200	-3

Table AA.3: Simulated depths and associated relative errors according to metallographic observations

	IN625			316L			CoCr		
	Exp. (µm)	**Model (µm)**	**Error (%)**	**Exp. (µm)**	**Model (µm)**	**Error (%)**	**Exp. (µm)**	**Model (µm)**	**Error (%)**
P0	92±6	73	20	55±9	64	-16	114±20	76	33
P1	201±14	103	49	110±6	79	28	146±28	82	44
P2	158±16	91	42	118±7	79	33	147±26	85	42
P3	118±29	73	38	68±7	73	-7	64±14	64	0
P4	142±18	82	42	26±6	61	-134	97±22	76	22
P5	80±14	70	13	52±5	64	-22	131±43	76	42
P6	121±14	70	42	60±4	64	-6	107±36	70	35
P7	11±3	48	-327	21±14	52	-149	57±24	61	-8
P8	33±5	52	-59	22±8	52	-137	70±31	64	9
P9	46±7	52	-14	18±9	45	-145	34±13	42	-24

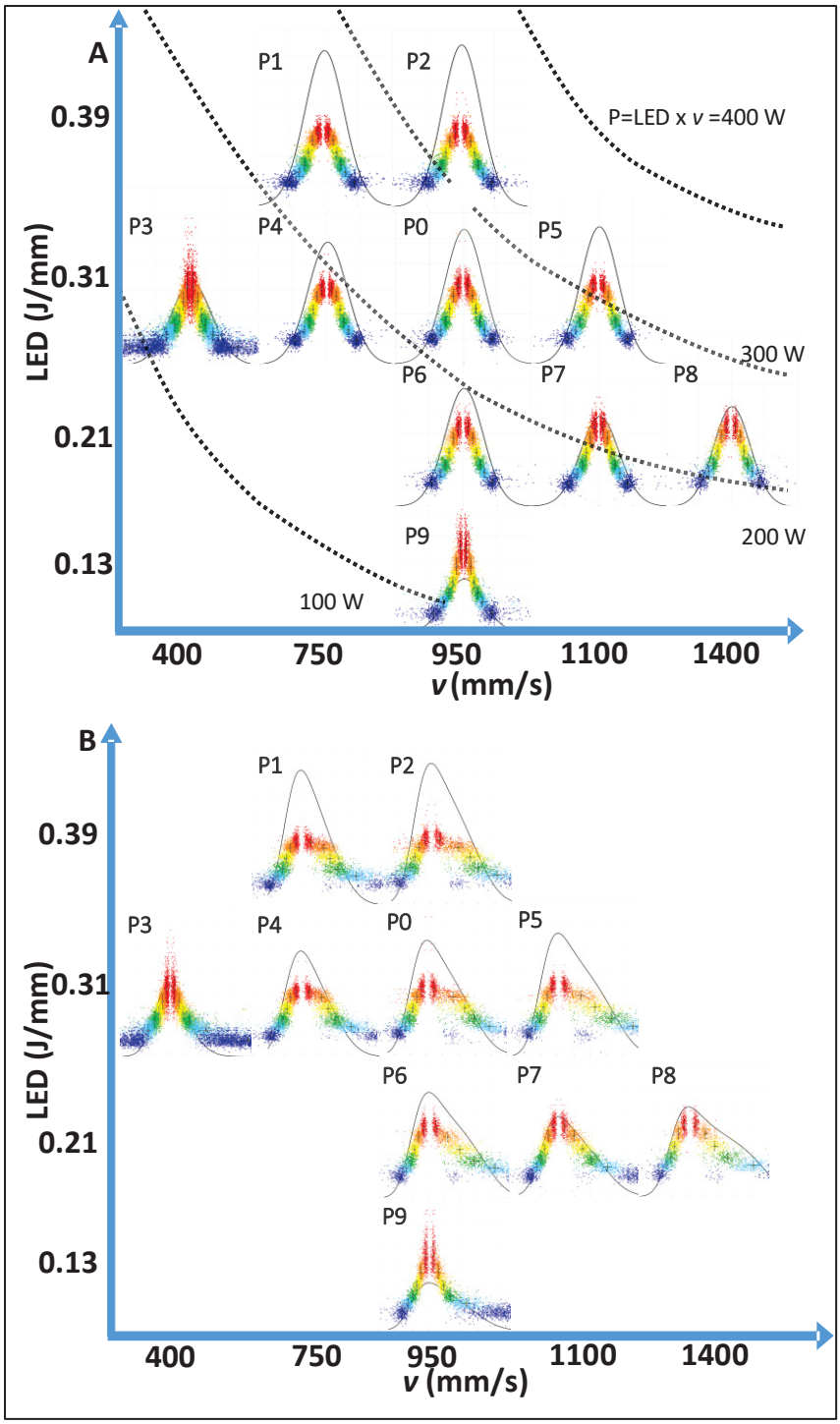

Figure AA.1: CoCr melt pool temperature profiles obtained using simulations (black lines) and camera observations (point clouds): A) width, B) length

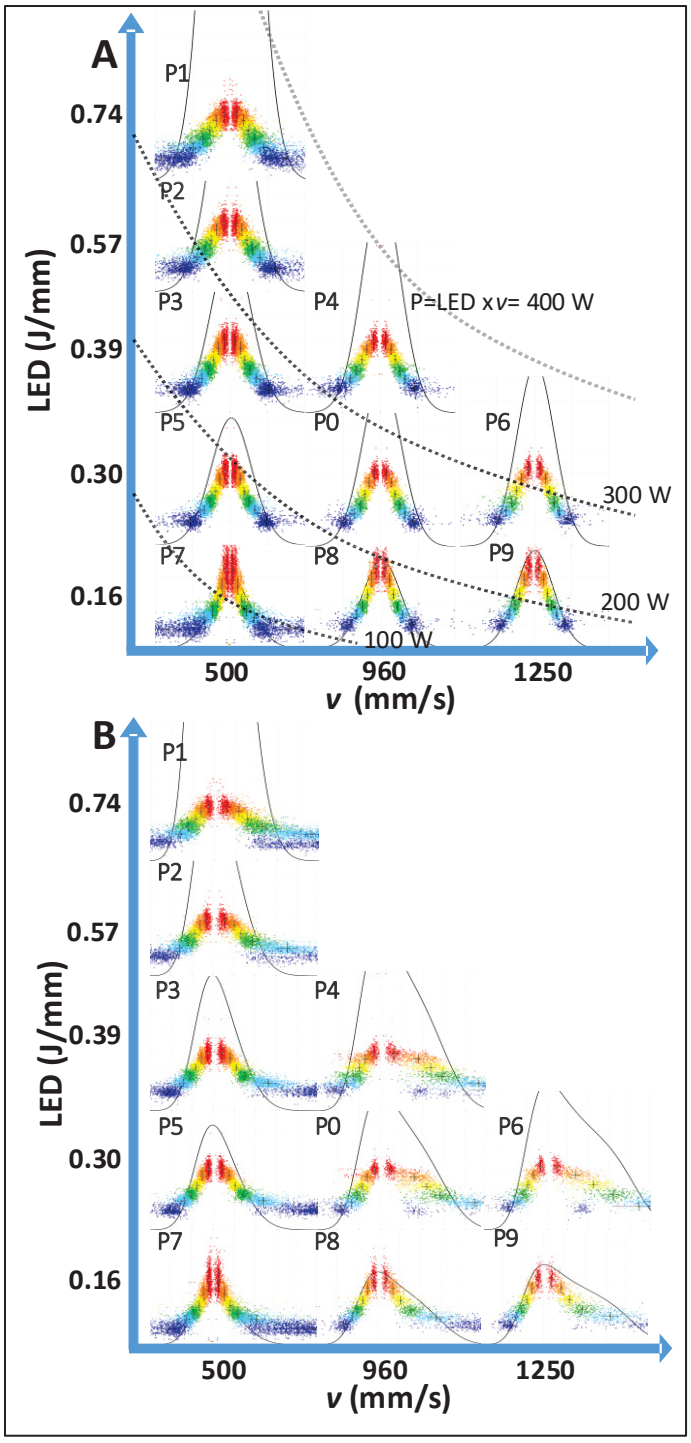

Figure AA.2: IN625 melt pool temperature profiles obtained using simulations (black lines) and camera observations (point clouds): A) width, B) length.

LIST OF BIBLIOGRAPHICAL REFERENCES

Araujo, A. (2017). Multi-spectral pyrometry—a review. Measurement Science and Technology, 28, 082002. https://doi.org/10.1088/1361-6501/aa7b4b

Ashby, A., Guss, G., Ganeriwala, R. K., Martin, A. A., DePond, P. J., Deane, D. J., Matthews, M. J., & Druzgalski, C. L. (2022). Thermal history and high-speed optical imaging of overhang structures during laser powder bed fusion: A computational and experimental analysis. Additive Manufacturing, 53, 102669. https://doi.org/10.1016/j.addma.2022.102669

Aydogan, B., & Chou, K. (2024). Review of In Situ Detection and Ex Situ Characterization of Porosity in Laser Powder Bed Fusion Metal Additive Manufacturing. Metals, 14, 669. https://doi.org/10.3390/met14060669

Bala, K., Pradhan, P. R., Saxena, N. S., & Saksena, M. P. (1989). Effective thermal conductivity of copper powders. Journal of Physics D: Applied Physics, 22(8), 1068–1072. https://doi.org/10.1088/0022-3727/22/8/009

Bidare, P., Bitharas, I., Ward, R. M., Attallah, M. M., & Moore, A. J. (2018). Fluid and particle dynamics in laser powder bed fusion. Acta Materialia, 142, 107–120. https://doi.org/10.1016/j.actamat.2017.09.051

Carter, L. N., Martin, C., Withers, P. J., & Attallah, M. M. (2014). The influence of the laser scan strategy on grain structure and cracking behaviour in SLM powder-bed fabricated nickel superalloy. Journal of Alloys and Compounds, 615, 338–347. https://doi.org/10.1016/j.jallcom.2014.06.172

Chen, S., Yang, Y., Liu, S., & Duan, M. (2023). In-situ additive manufacturing deposition trajectory monitoring and compensation with thermal camera. Additive Manufacturing, 78, 103820. https://doi.org/10.1016/j.addma.2023.103820

Cheng, B., & Chou, K. (2016). Melt pool geometry simulations for powder-based electron beam additive manufacturing. Solid Freeform Fabrication Symposium Proceedings, 644–654.

Cheng, J., Huo, Y., Fernandez-Zelaia, P., Hu, X., Li, M., & Sun, X. (2024). A Gaussian Process-Based Extended Goldak Heat Source Model for Finite Element Simulation of Laser Powder Bed Fusion Additive Manufacturing Process. Computational Materials Science, 244, 113185. https://doi.org/10.1016/j.commatsci.2024.113185

Clijsters, S., Craeghs, T., Buls, S., & Kempen, K. (2014). In situ quality control of the selective laser melting process using a high-speed, real-time melt pool monitoring system. International Journal of Advanced Manufacturing Technology, 75, 1089–1101. https://doi.org/10.1007/s00170-014-6214-8

Coeck, S., Bisht, M., Plas, J., & Verbiest, F. (2019). Prediction of lack of fusion porosity in selective laser melting based on melt pool monitoring data. Additive Manufacturing, 25, 347–356. https://doi.org/10.1016/j.addma.2018.11.015

Cox, B., Ghayoor, M., Doyle, R. P., Pasebani, S., & Gess, J. (2022). Numerical model of heat transfer during laser powder bed fusion of 316L stainless steel. The International Journal of Advanced Manufacturing Technology, 119(9–10), 5715–5725. https://doi.org/10.1007/s00170-021-08352-0

De Izarra, C., & Gitton, J.-M. (2010). Calibration and temperature profile of a tungsten filament lamp. European Journal of Physics, 31, 933–942. https://doi.org/10.1088/0143-0807/31/4/022

De Leon, E., Riensche, A., Bevans, B. D., Billings, C., Siddique, Z., & Liu, Y. (2025). A Review of Modeling, Simulation, and Process Qualification of Additively Manufactured Metal Components via the Laser Powder Bed Fusion Method. Journal of Manufacturing and Materials Processing, 9(1), 22. https://doi.org/10.3390/jmmp9010022

Doubenskaia, M. A., Zhirnov, I. V., Teleshevskiy, V. I., Bertrand, P., & Smurov, I. Y. (2015). Determination of True Temperature in Selective Laser Melting of Metal Powder Using Infrared Camera. Materials Science Forum, 834, 93–102. https://doi.org/10.4028/www.scientific.net/MSF.834.93

Feng, H., Wang, L., Huang, Y., Wang, Y., Zhu, L., & Huang, H. (2026). Learning Physics-Informed Noise Models from Dark Frames for Low-Light Raw Image Denoising. IEEE Transactions on Pattern Analysis and Machine Intelligence, 1–18. https://doi.org/10.1109/TPAMI.2026.3651447

Fu, L., Leutz, R., & Ries, H. (2006). Physical modeling of filament light sources. Journal of Applied Physics, 100(10), 103528. https://doi.org/10.1063/1.2364669

Fuchs, L., & Eischer, C. (2018). In-process monitoring systems for metal additive manufacturing. EOS GmbH White Paper.

Goossens, L. R., & Van Hooreweder, B. (2021). A virtual sensing approach for monitoring melt-pool dimensions using high speed coaxial imaging during laser powder bed fusion

of metals. Additive Manufacturing, 40, 101923. https://doi.org/10.1016/j.addma.2021.101923

Gordon, J. V., Narra, S. P., Cunningham, R. W., Liu, H., Chen, H., Suter, R. M., Beuth, J. L., & Rollett, A. D. (2020). Defect structure process maps for laser powder bed fusion additive manufacturing. Additive Manufacturing, 36, 101552. https://doi.org/10.1016/j.addma.2020.101552

Grasso, M., & Colosimo, B. M. (2017). Process defects and in situ monitoring methods in metal powder bed fusion: a review. Measurement Science and Technology, 28, 044005. https://doi.org/10.1088/1361-6501/aa5c4f

Guo, K., Ji, Y., Li, Y., Kang, X., Bai, H., & Ren, H. (2022). Numerical Simulation of Temperature Field and Melt Pool Characteristics of CP-Ti Manufactured by Laser Powder Bed Fusion. Metals, 13(1), 11. https://doi.org/10.3390/met13010011

Guo, L., Wang, H., Liu, H., Huang, Y., Wei, Q., Leung, C. L. A., Wu, Y., & Wang, H. (2023). Understanding keyhole induced-porosities in laser powder bed fusion of aluminum and elimination strategy. International Journal of Machine Tools and Manufacture, 184, 103977. https://doi.org/10.1016/j.ijmachtools.2022.103977

Gurrala, A. K., Rahul, G., Amalan, S., Preejith, S., & Sivaprakasam, M. (2023). Eliminating Vertical Fixed Pattern Noise in CMOS-Based Endoscopic Images using Modified Dark Frame Subtraction. 2023 IEEE International Symposium on Medical Measurements and Applications (MeMeA), 1–6. https://doi.org/10.1109/MeMeA57477.2023.10171876

Harke, K. J., Calta, N., Tringe, J., & Stobbe, D. (2022). Laser-based ultrasound interrogation of surface and sub-surface features in advanced manufacturing materials. Scientific Reports, 12(1), 3309. https://doi.org/10.1038/s41598-022-07261-w

Holla, V., Grünewald, J., Kopp, P., Praegla, P. M., Meier, C., Wudy, K., & Kollmannsberger, S. (2024). Validity of Thermal Simulation Models for Different Laser Beam Shapes in Bead-on-Plate Melting. Integrating Materials and Manufacturing Innovation, 13(4), 969–985. https://doi.org/10.1007/s40192-024-00382-2

Hooper, P. A. (2018). Melt pool temperature and cooling rates in laser powder bed fusion. Additive Manufacturing, 22, 548–559. https://doi.org/10.1016/j.addma.2018.05.032

Huang, Y., Fleming, T. G., Clark, S. J., Marussi, S., Fezzaa, K., Thiyagalingam, J., Leung, C. L. A., & Lee, P. D. (2022). Keyhole fluctuation and pore formation mechanisms during laser powder bed fusion additive manufacturing. Nature Communications, 13, 1170. https://doi.org/10.1038/s41467-022-28694-x

Hügel, H., & Dausinger, F. (1998). Fundamentals of Laser-Induced Processes. In D. Bäuerle (Ed.), Laser Processing and Chemistry (pp. 3–62). Springer.

Kang, S. H., Jin, H.-H., Jang, J., Choi, Y. S., Oh, K. H., Foley, D. C., & Zhang, X. (2013). A Quantitative Evaluation of Microstructure by Electron Back-Scattered Diffraction Pattern Quality Variations. Microscopy and Microanalysis, 19(S5), 83–88. https://doi.org/10.1017/S1431927613012397

Karayagiz, K., Elwany, A., Tapia, G., Franco, B., Johnson, L., Ma, J., Karaman, I., & Arróyave, R. (2019). Numerical and experimental analysis of heat distribution in the laser powder bed fusion of Ti-6Al-4V. IISE Transactions, 51(2), 136–152. https://doi.org/10.1080/24725854.2018.1461964

Khairallah, S. A., Anderson, A. T., Rubenchik, A., & King, W. E. (2016). Laser powder-bed fusion additive manufacturing: Physics of complex melt flow and formation mechanisms of pores, spatter, and denudation zones. Acta Materialia, 108, 36–45. https://doi.org/10.1016/j.actamat.2016.02.014

Kim, J., Lee, S., Hong, J.-K., Kang, N., & Choi, Y. S. (2020). Calibration of Laser Penetration Depth and Absorptivity in Finite Element Method Based Modeling of Powder Bed Fusion Melt Pools. Metals and Materials International, 26, 891–902. https://doi.org/10.1007/s12540-019-00599-3

Kou, S. (2002). Welding Metallurgy (2nd ed.). Wiley-Interscience. https://doi.org/10.1002/0471434027

Kumar, R., Kumar, M., & Chohan, J. S. (2021). The role of additive manufacturing for biomedical applications: A critical review. Journal of Manufacturing Processes, 64, 828–850. https://doi.org/10.1016/j.jmapro.2021.02.022

Leclercq, A., & Brailovski, V. (2024). Improving laser powder bed fusion printability of tungsten powders using simulation-driven process optimization algorithms. Materials, 17(8), 1865. https://doi.org/10.3390/ma17081865

Leclercq, A., Mouret, T., & Brailovski, V. (2025). Laser powder bed fusion of molybdenum: Density, structure and mechanical properties at room and elevated temperatures. Materials Science and Engineering: A, 929, 148004. https://doi.org/10.1016/j.msea.2025.148004

Letenneur, M., Kreitcberg, A., & Brailovski, V. (2019). Optimization of laser powder bed fusion processing using a combination of melt pool modeling and design of experiment approaches: Density control. Journal of Manufacturing and Materials Processing, 3(1), 21. https://doi.org/10.3390/jmmp3010021

Liu, J., & Wen, P. (2022). Metal vaporization and its influence during laser powder bed fusion process. Materials & Design, 215, 110505. https://doi.org/10.1016/j.matdes.2022.110505

Liu, S., Li, R., Zhou, J., Dai, C., Yu, J., & Zhang, Q. (2025). Physics-Based Data Augmentation Enables Accurate Machine Learning Prediction of Melt Pool Geometry. Applied Sciences, 15(15), 8587. https://doi.org/10.3390/app15158587

Mahmoudi, M., Tapia, G., Karayagiz, K., Franco, B., Ma, J., Arroyave, R., Karaman, I., & Elwany, A. (2018). Multivariate Calibration and Experimental Validation of a 3D Finite Element Thermal Model for Laser Powder Bed Fusion Metal Additive Manufacturing. Integrating Materials and Manufacturing Innovation, 7(3), 116–135. https://doi.org/10.1007/s40192-018-0113-z

Mao, Y., Lin, X., Zhu, H., & Zhu, K. (2024). Physics-guided spatiotemporal approach for melt pool size prediction in laser powder bed fusion. Virtual and Physical Prototyping, 19(1), e2427243. https://doi.org/10.1080/17452759.2024.2427243

McCann, R., Obeidi, M. A., Hughes, C., McCarthy, É., Egan, D. S., Vijayaraghavan, R. K., Joshi, A. M., Gazon, V. A., Dowling, D. P., McNally, P. J., & Brabazon, D. (2021). In-situ sensing, process monitoring and machine control in Laser Powder Bed Fusion: A review. Additive Manufacturing, 45, 102058. https://doi.org/10.1016/j.addma.2021.102058

Mitchell, J. A., Ivanoff, T. A., Dagel, D., Madison, J. D., & Jared, B. (2019). Linking pyrometry to porosity in additively manufactured metals. Additive Manufacturing, 31, 100946. https://doi.org/10.1016/j.addma.2019.100946

Mitrašinović, A., Đurđević, T., Nešković, J., & Radosavljević, M. (2025). Temperature Monitoring in Metal Additive Manufacturing in the Era of Industry 4.0. Technologies, 13, 317. https://doi.org/10.3390/technologies13080317

Myers, A. J., Gobert, C., Beuth, J. L., & Malen, J. A. (2025). High-speed imaging investigation and process mapping of the plume behavior in laser powder bed fusion. Additive Manufacturing, 106, 104797. https://doi.org/10.1016/j.addma.2025.104797

Myers, A. J., Quirarte, G., Ogoke, F., Lane, B. M., Uddin, S. Z., Farimani, A. B., Beuth, J. L., & Malen, J. A. (2023). High-resolution melt pool thermal imaging for metals additive manufacturing using the two-color method with a color camera. Additive Manufacturing, 73, 103663. https://doi.org/10.1016/j.addma.2022.103663

Pandiyan, V., Wróbel, R., Richter, R. A., Leparoux, M., Leinenbach, C., & Shevchik, S. (2024). Monitoring of Laser Powder Bed Fusion process by bridging dissimilar process

maps using deep learning-based domain adaptation on acoustic emissions. Additive Manufacturing, 80, 103974. https://doi.org/10.1016/j.addma.2024.103974

Park, H., Mullin, K. M., Kumar, V., Wander, O., Pollock, T. M., & Zhu, Y. (2025). Resolving thermal gradients and solidification velocities during laser melting of a refractory alloy. Additive Manufacturing, 105, 104750. https://doi.org/10.1016/j.addma.2025.104750

Partouche-Sebban, D., Holtkamp, D. B., Rodriguez, P., Stone, J. B., Borror, S. D., Kruschwitz, C. A., & Young, J. A. (2005). Alternative calibration techniques for high-speed pyrometers in shock experiments. Review of Scientific Instruments, 76, 013106. https://doi.org/10.1063/1.1833331

Patel, S., & Vlasea, M. (2020). Melting modes in laser powder bed fusion. Materialia, 9, 100591. https://doi.org/10.1016/j.mtla.2020.100591

Peng, L., Benavidez, E., Mukherjee, S., Morales, R. E., Tringe, J. W., Stobbe, D., & Deng, Y. (2025). In-situ 3D temperature field modeling and characterization using eddy current for metal additive manufacturing process monitoring. Scientific Reports, 15, 9999. https://doi.org/10.1038/s41598-025-94553-6

Penny, R. W., & John Hart, A. (2025). Radiometric temperature measurement for metal additive manufacturing via temperature emissivity separation. Additive Manufacturing, 110, 104904. https://doi.org/10.1016/j.addma.2025.104904

Pessoa, S., Guimarães, A. S., Lucas, S. S., & Simões, N. (2021). 3D printing in the construction industry — a systematic review of the thermal performance in buildings. Renewable and Sustainable Energy Reviews, 141, 110794. https://doi.org/10.1016/j.rser.2021.110794

Ren, Z., Fu, G., Liu, F., Mao, S., Gao, R., Jiang, J., & Tang, Z. (2024). Elucidation of laser irradiation behaviors associated with the keyhole dynamics during laser powder bed fusion. Journal of Materials Research and Technology, 32, 3555–3567. https://doi.org/10.1016/j.jmrt.2024.08.019

Russell, D. C., Schofield, F. H., & Schofield, F. H. (1960). A theory of the filament temperature distribution of the tungsten vacuum-lamp, with special reference to optical pyrometry. Philosophical Transactions of the Royal Society of London. Series A, Mathematical and Physical Sciences, 252(1016), 463–498. https://doi.org/10.1098/rsta.1960.0012

Scheel, P., Markovic, P., Van Petegem, S., Makowska, M. G., Wrobel, R., Mayer, T., Leinenbach, C., Mazza, E., & Hosseini, E. (2023). A close look at temperature profiles during laser powder bed fusion using operando X-ray diffraction and finite element

simulations. Additive Manufacturing Letters, 6, 100150. https://doi.org/10.1016/j.addlet.2023.100150

Schuöcker, D. (1998). Handbook of the EuroLaser Academy. Vol. 2 (1st ed.). Chapman & Hall.

Sherby, O. D., & Burke, P. M. (1968). Mechanical behavior of crystalline solids at elevated temperature. Progress in Materials Science, 13, 323–390. https://doi.org/10.1016/0079-6425(68)90024-8

Shrestha, S., & Chou, K. (2018). Single track scanning experiment in laser powder bed fusion process. Procedia Manufacturing, 26, 857–864. https://doi.org/10.1016/j.promfg.2018.07.110

Shrestha, S., & Chou, K. (2022). Formation of keyhole and lack of fusion pores during the laser powder bed fusion process. Manufacturing Letters, 32, 19–23. https://doi.org/10.1016/j.mfglet.2022.01.005

Sih, S. S., & Barlow, J. W. (2004). The prediction of the emissivity and thermal conductivity of powder beds. Particulate Science and Technology, 22(3), 291–304. https://doi.org/10.1080/02726350490501682a

Soares, M., Campion, D., Kreitcberg, A., & Brailovski, V. (2026, March 18). In-situ LPBF monitoring using a dual-wavelength thermal camera calibrated via ex-situ single-track measurements. Available at SSRN: https://papers.ssrn.com/sol3/papers.cfm?abstract_id=6437579

Spurek, M. A., Spierings, A. B., Lany, M., Revaz, B., Santi, G., Wicht, J., & Wegener, K. (2022). In-situ monitoring of powder bed fusion of metals using eddy current testing. Additive Manufacturing, 60, 103259. https://doi.org/10.1016/j.addma.2022.103259

Taherkhani, K., Sheydaeian, E., Eischer, C., Otto, M., & Toyserkani, E. (2021). Development of a defect-detection platform using photodiode signals collected from the melt pool of laser powder bed fusion. Journal of Manufacturing Processes, 67, 120–133. https://doi.org/10.1016/j.jmapro.2021.04.040

Tao, Z., Thanki, A., Goossens, L., Witvrouw, A., Vrancken, B., & Dewulf, W. (2024). Photodiode-based porosity prediction in laser powder bed fusion considering inter-hatch and inter-layer effects. Journal of Materials Processing Technology, 332, 118539. https://doi.org/10.1016/j.jmatprotec.2024.118539

Tolias, P. (2017). Analytical expressions for thermophysical properties of solid and liquid tungsten relevant for fusion applications. Nuclear Materials and Energy, 13, 42–57. https://doi.org/10.1016/j.nme.2017.08.002

Vollmer, M., & Möllmann, K.-P. (2017). Infrared Thermal Imaging: Fundamentals, Research and Applications (2nd ed.). Wiley-VCH. ISBN: 978-3-527-40717-0.

Wang, J., Zhu, R., Liu, Y., & Zhang, L. (2023). Understanding melt pool characteristics in laser powder bed fusion: An overview of single- and multi-track melt pools for process optimization. Advanced Powder Materials, 2, 100137. https://doi.org/10.1016/j.apmate.2023.100137

Wang, L., Felicelli, S. D., & Craig, J. E. (2009). Experimental and Numerical Study of the LENS Rapid Fabrication Process. Journal of Manufacturing Science and Engineering, 131(4), 041019. https://doi.org/10.1115/1.3173952

Wang, R., Garcia, D., Kamath, R. R., Dou, C., Ma, X., Shen, B., Choo, H., Fezzaa, K., Yu, H. Z., & Kong, Z. (2022). In situ melt pool measurements for laser powder bed fusion using multi sensing and correlation analysis. Scientific Reports, 12, 13716. https://doi.org/10.1038/s41598-022-18096-w

Wang, W., Ning, J., Garmestani, H., & Liang, S. Y. (2022). Analytical Prediction of Molten Pool Dimensions in Powder Bed Fusion Considering Process Conditions-Dependent Laser Absorptivity. Applied Sciences, 12(23), 11926. https://doi.org/10.3390/app122311926

Williams, R. J., Piglione, A., Ronneberg, T., Jones, C., Pham, M., Davies, C. M., & Hooper, P. A. (2019). In situ thermography for laser powder bed fusion: Effects of layer temperature on porosity, microstructure and mechanical properties. Additive Manufacturing, 30, 100880. https://doi.org/10.1016/j.addma.2019.100880

Xu, Z., Tian, Q., Hu, P., Li, H., & Shen, S. (2024). Laser ultrasonic detection of submillimeter artificial holes in laser powder bed fusion manufactured alloys. Optics and Laser Technology, 169, 110030. https://doi.org/10.1016/j.optlastec.2023.110030

Yan, Z., Liu, W., Tang, Z., Liu, X., Zhang, N., Li, M., & Zhang, H. (2018). Review on thermal analysis in laser-based additive manufacturing. Optics & Laser Technology, 106, 427–441. https://doi.org/10.1016/j.optlastec.2018.04.034

Yang, X., Li, Y., & Li, B. (2023). Formation mechanisms of lack of fusion and keyhole-induced pore defects in laser powder bed fusion process: A numerical study. International Journal of Thermal Sciences, 188, 108221. https://doi.org/10.1016/j.ijthermalsci.2023.108221

Yang, Y., Großmann, A., Kühn, P., Mölleney, J., Kropholler, L., Mittelstedt, C., & Xu, B.-X. (2022). Validated dimensionless scaling law for melt pool width in laser powder bed fusion. Journal of Materials Processing Technology, 299, 117316. https://doi.org/10.1016/j.jmatprotec.2021.117316

Yang, Z., Zhang, S., Ji, X., & Liang, S. Y. (2024). Model-Based Sensitivity Analysis of the Temperature in Laser Powder Bed Fusion. Materials, 17(11), 2565. https://doi.org/10.3390/ma17112565

Zhang, Y., Guo, M., Wang, Z., Xing, J., & Wang, X. (2023). Monitoring of single-track melting states based on photodiode signal during laser powder bed fusion. Sensors, 23(24), 9793. https://doi.org/10.3390/s23249793

Zhang, Z., Zhang, T., Sun, C., Karna, S., & Yuan, L. (2024). Understanding Melt Pool Behavior of 316L Stainless Steel in Laser Powder Bed Fusion Additive Manufacturing. Micromachines, 15(2), 170. https://doi.org/10.3390/mi15020170

Zhao, C., Parab, N., Li, X., Fezzaa, K., Tan, W., Rollett, A., & Sun, T. (2020). Critical instability at moving keyhole tip generates porosity in laser melting. Science, 370, 1080–1086. https://doi.org/10.1126/science.abd1587